Oceanic crust and island arc formation in Central Asia during late Neoproterozoic times - Evidence from petrological and geochemical studies

Jörg A. Pfänder

2001

Oceanic crust and island arc formation in Central Asia during late Neoproterozoic times - Evidence from petrological and geochemical studies

Dissertation zur Erlangung des Grades
„Doktor der Naturwissenschaften“
am Fachbereich Geowissenschaften der Johannes-Gutenberg
Universität Mainz

Jörg A. Pfänder
Mainz, 2001

Jahr der mündlichen Prüfung: 2001

Table of contents

Zusammenfassung für Fachfremde I

Zusammenfassung II

Abstract V

CHAPTER 1 - Introduction

1.1 PURPOSE 1
1.2 OPHIOLITES 2
1.3 EVOLUTION OF CENTRAL ASIA 3
1.4 SUMMARY OF CHAPTERS 2- 4 6
1.5 OUTLOOK AND REMAINING PROBLEMS 7
1.6 METHODS 7
1.7 REFERENCES 9
APPENDIX 11

CHAPTER 2 - Determination of Y, Zr and ultra-low Nb in geological material by multi-ion counting spark-source mass spectrometry 12

ABSTRACT 13
2.1 INTRODUCTION 13
2.2 SAMPLE PREPARATION 14
2.3 MASS SPECTROMETER 14
2.4 MEASURING PROCEDURE 15
2.5 RESULTS 15
2.5.1 Precision and detection limits 15
2.5.2 Interferences and correction method 16
2.5.3 Concentrations 18
2.5.4 Accuracy 18
2.5.5 Comparison of MIC-SSMS and ICP-MS data 19
2.6 REFERENCES 21

CHAPTER 3 - Coupled evolution of back-arc and island arc-like mafic crust in the late Neoproterozoic Agardagh Tes-Chem ophiolite, Central Asia: Evidence from trace element and Sr-Nd-Pb isotope data 22

ABSTRACT 23

3.1 INTRODUCTION 24

3.2 GEOLOGICAL SETTING 26

3.3 RESULTS 27

3.3.1 Major Elements 27

3.3.2 Trace elements 31

3.3.2.1 Compatible trace elements 31

3.3.2.2 Incompatible trace elements 31

3.3.2.3 Rare earth elements 33

3.3.3 Isotopic data 35

3.4 DISCUSSION 38

3.4.1 Parental magma(s) and fractional crystallization 38

3.4.2 Degree of melting 39

3.4.3 Source composition 41

3.4.4 Mixing relationships vs. single parental melt 42

3.4.5 Crustal assimilation vs. source contamination 44

3.5 CONCLUSIONS 46

3.6 REFERENCES 47

APPENDIX: ANALYTICAL METHODS 53

CHAPTER 4 - Ultramafic cumulates and gabbros from boninitic primary melts and lower oceanic crustal evolution in the Agardagh Tes-Chem ophiolite (Tuva, Central Asia) - petrological and geochemical constraints 55

ABSTRACT 56

4.1 INTRODUCTION 57

4.2 GEOLOGICAL SETTING 58

4.3 PETROGRAPHY AND MINERAL COMPOSITIONS 60

4.3.1 Petrographic descriptions 60

4.3.2 Olivine compositions 65

4.3.3 Orthopyroxene compositions 65

4.3.4 Spinel compositions 66

4.3.5 Clinopyroxene compositions 66

4.3.6 Hornblende compositions 68

4.3.7 Plagioclase compositions 68
4.4 GEOCHEMISTRY 69
4.4.1 Major elements 69
4.4.2 Trace elements 69
4.4.3 Rare earth elements 74
4.4.4 Isotopic compositions 74
4.5 DISCUSSION 77
4.5.1 Origin of ultramafic rocks 77
4.5.1.1 Dunites and harzburgites 77
4.5.1.2 Pyroxenites and wehrlites 78
4.5.2 Origin of gabbroic rocks 79
4.5.2.1 Mineral compositions 79
4.5.2.2 Crystallization from a single intrusion 80
4.5.2.3 Order of crystallization 81
4.5.2.4 Depth of gabbro formation 81
4.5.3 Equilibrium melts 82
4.5.3.1 Primary melt composition(s) 82
4.5.3.2 Parental melts of wehrlites and gabbros 83
4.5.4 Evidence for a boninitic source and degree of melting 84
4.5.4.1 Boninitic source characteristics 84
4.5.4.2 Degree of melting from spinel compositions 86
4.5.5 Trace element compositions of gabbroic rocks and trapped-melt 87
4.5.5.1 Complications in the interpretation of trace element patterns . . 87
4.5.5.2 REE composition of gabbros and trapped-melt effects 88
4.5.6 Source composition, mixing relationships and assimilation 89
4.5.6.1 Isotopic constraints 89
4.5.6.2 Trace element constraints 90
4.5.6.3 Assimilation of pre-existing arc crust 92
4.5.7 Evolution of the lower oceanic crust in the ATCO 94
4.5.7.1 Geodynamic setting and crustal structure 94
4.5.7.2 Open system magma chamber evolution 95
4.6 CONCLUSIONS 98
4.7 REFERENCES 100
APPENDIX A: ANALYTICAL METHODS 110
APPENDIX B: EQUATIONS AND MODEL PARAMETERS 112

Zusammenfassung für Fachfremde

Die äusserste Schale der Erde setzt sich aus zwei grundsätzlich verschiedenen Krustentypen, nämlich aus kontinentaler und aus ozeanischer Kruste zusammen. Während das Alter der ältesten Gesteine aus der kontinentalen Kruste nach heutigem Wissen sehr nahe an das Alter der Erde selbst (4.57 Milliarden Jahre) heranreicht, ist die ozeanische Kruste höchstens 200 Millionen Jahre alt. Der Grund hierfür ist, dass ozeanische Kruste stetig an sogenannten mittelozeanischen Rücken neu gebildet wird. Diese mittelozeanischen Rücken sind riesige untermeerische Gebirge, in deren axialen Zentren heiße Magmen aus dem Erdmantel nach oben steigen, abkühlen und kristallisieren. Die auf diese Weise entstandene ozeanische Kruste wandert kontinuierlich zu den Seiten hin weg, um schließlich an sogenannten Subduktionszonen wieder in den Erdmantel hinabzutauchen. Aufgrund der Kontinentaldrift können im Laufe der Erdgeschichte und infolge der Kollision von Krustenplatten ozeanische Krustenfragmente auf die Kontinente überschoben werden. Man spricht von Obduktion, die gestrandeten ozeanischen Krustenfragmente nennt man Ophiolithe. Heute findet man solche Ophiolithe in grossen Gebirgszügen innerhalb der Kontinente.

Die vorliegende Arbeit beschäftigt sich mit der magmatischen Entwicklung eines solchen Restes ehemaliger Ozeankruste, dem Agardagh Tes-Chem Ophiolith in Zentralasien. Dieses Ozeankrustenfragmente wurde erstmalig im Rahmen dieser Arbeit durch radiometrische Altersbestimmung auf 570 Millionen Jahre datiert. Dieser Ophiolith repräsentiert damit die Reste eines Ozeans, der heute nicht mehr existiert. Weiterhin wurde auf der Basis geochemischer Verfahren, d.h. durch die Bestimmung der Konzentrationen und der Isotopenverhältnisse bestimmter chemischer Elemente in Gesteinsproben, erstmalig ein Modell zur Entstehung dieses Ophioliths erstellt. Demnach ist seine Entwicklung nicht unmittelbar an einen typischen mittelozeanischen Rücken, sondern an ein über einer Subduktionszone gebildetes sogenanntes Randbecken gekoppelt. Dabei entstanden im Erdmantel *über* einer abtauchenden Ozeankrustenplatte stark an bestimmten chemischen Elementen verarmte Schmelzen. Von der abtauchenden Platte mitgeführte Sedimente und Fluide führten andererseits zu einer selektiven Anreicherung anderer chemischer Elemente. In einem ersten Entwicklungsstadium verursachten diese Schmelzen vulkanische Eruptionen und es entstanden vulkanische Gesteine. In einem späteren Stadium stiegen weitere, aber chemisch unterschiedliche Schmelzen auf. Diese gelangten jedoch nicht bis an die Erdoberfläche, sondern blieben in der Kruste stecken, wo sie eine sogenannte Magmenkammer bildeten. Dort kristallisierten bestimmte Minerale infolge langsamer Abkühlung und lagerten sich am Grund der Magmenkammer ab, wo sie einen Teil der in dieser Arbeit untersuchten Gesteine bildeten.

Zusammenfassung

Die vorliegende Arbeit behandelt die Entwicklung des 570 Ma alten, neoproterozoischen Agardagh - Tes-Chem Ophioliths (ATCO) in Zentralasien. Dieser Ophiolith liegt südwestlich des Baikalsees (50.5° N, 95° E) und wurde im frühen Stadium der Akkretion des Zentralasiatischen Mobilgürtels auf den nordwestlichen Rand des Tuvinisch-Mongolischen Mikrokontinentes aufgeschoben. Bei dem Zentralasiatische Mobilgürtel handelt es sich um einen riesigen Akkretions- Subduktionskomplex, der heute das größte zusammenhängende Orogen der Erde darstellt. Im Rahmen dieser Arbeit wurden eine Reihe plutonischer und vulkanischer Gesteine, sowie verschiedene Mantelgesteine des ATCO mittels mikroanalytischer und geochemischer Verfahren untersucht (Elektronenstrahlmikrosonde, Ionenstrahlmikrosonde, Spurenelement- und Isotopengeochemie). Die Auswertung dieser Daten ermöglichte die Entwicklung eines geodynamisch-petrologischen Modells zur Entstehung des ATCO.

Die vulkanischen Gesteine lassen sich aufgrund ihrer Spurenelement- und Isotopenzusammensetzung in inselbogenbezogene und „back-arc Becken“ bezogene Gesteine (IA-Gesteine und BAB-Gesteine) unterscheiden. Darüber hinaus gibt es eine weitere, nicht eindeutig zuzuordnende Gruppe, die hauptsächlich mafische Gänge umfasst. Der grösste Teil der untersuchen Vulkanite gehört zur Gruppe der IA-Gesteine. Es handelt sich um Al-reiche Basalte und basaltische Andesite, welche aus einem evolvierten Stammmagma mit Mg# $\geq$0.60, Cr ~ 180 µg/g und Ni ~ 95 µg/g hauptsächlich durch Klinopyroxenfraktionierung entstanden sind. Das Stammmagma selbst entstand durch Fraktionierung von ca. 12 % Olivin und geringen Anteilen von Cr-Spinell aus einer primären, aus dem Mantel abgeleiteten Schmelze. Die IA-Gesteine haben hohe Konzentrationen an inkompatiblen Spurenelementen (leichte-(L)- Seltenerdelement-(SEE)-Konzentrationen etwa 100-fach chondritisch, chondritnormierte $(La/Yb)_c$ von 14.6 - 5.1), negative Nb-Anomalien (Nb/La = 0.37 - 0.62) und niedrige Zr/Nb Verhältnisse (7 - 14) relativ zu den BAB-Gesteinen. Initiale ϵ_{Nd} Werte liegen bei etwas +5.5, initiale Bleiisotopenverhältnisse sind: $^{206}Pb/^{204}Pb$ = 17.39 - 18.45, $^{207}Pb/^{204}Pb$ = 15.49 - 15.61, $^{208}Pb/^{204}Pb$ = 37.06 - 38.05. Die Anreicherung lithophiler inkompatibler Spurenelemente (LILE) in dieser Gruppe ist signifikant (Ba/La = 11 - 130) und zeigt den Einfluss subduzierter Komponenten an. Die BAB-Gesteine repräsentieren Schmelzen, die sehr wahrscheinlich aus der gleichen Mantelquelle wie die IA-Gesteine stammen, aber durch höhere Aufschmelzgrade (8 - 15 %) und ohne den Einfluss subduzierter Komponenten entstanden sind. Sie haben niedrigere Konzentrationen an inkompatiblen Spurenelementen, flache SEE-Muster ($(La/Yb)_c$ = 0.6 - 2.4) und höhere initiale ϵ_{Nd} Werte zwischen +7.8 und +8.5. Nb Anomalien existieren nicht und Zr/Nb Verhältnisse sind hoch (21 - 48).

Um die geochemische Entwicklung der vulkanischen Gesteine des ATCO zu erklären, sind mindestens drei Komponenten erforderlich: (1) eine angereicherte, ozeaninselbasalt-ähnliche

Komponente mit hoher Nb Konzentration über ~ 30 µg/g, einem niedrigen Zr/Nb Verhältnis (ca. 6.5), einem niedrigen initialen ϵ_{Nd} Wert (um 0), aber mit radiogenen $^{206}Pb/^{204}Pb$-, $^{207}Pb/^{204}Pb$- und $^{208}Pb/^{204}Pb$-Verhältnissen; (2) eine N-MORB ähnliche „back-arc Becken" Komponente mit flachem SEE-Muster und einem hohen initialen ϵ_{Nd} Wert von mindestens +8.5, und (3) eine Inselbogen-Komponente aus einer verarmten Mantelquelle, welche durch die abtauchende Platte geochemisch modifiziert wurde. Die geochemische Entstehung der ATCO Vulkanite lässt sich dann am besten durch eine Kombination aus Quellenkontamination, fraktionierte Kristallisation und Magmenmischung erklären. Geodynamisch gesehen entstand der ATCO sehr wahrscheinlich in einem intraozeanischen Inselbogen - back-arc System.

Bei den untersuchten Plutoniten handelt es sich um ultramafische Kumulate (Wehrlite und Pyroxenite) sowie um gabbroische Plutonite (Olivin-Gabbros bis Diorite). Die geochemischen Charakteristika der mafischen Plutonite sind deutlich unterschiedlich zu denen der vulkanischen Gesteine, weshalb sie sehr wahrscheinlich ein späteres Entwicklungsstadium des ATCO repräsentieren.

Die Spurenelement-Konzentrationen in den Klinopyroxenen der ultramafischen Kumulate sind extrem niedrig, mit etwa 0.1- bis 1-fach chondritischen SEE-Konzentrationen und mit deutlich LSEE-verarmten Mustern ($(La/Yb)_c$ = 0.27 - 0.52). Berechnete Gleichgewichtsschmelzen der ultramafischen Kumulate zeigen grosse Ähnlichkeit zu primären boninitischen Schmelzen. Die primären Magmen waren daher boninitischer Zusammensetzung und entstanden in dem durch vorausgegangene Schmelzprozesse stark verarmten Mantelkeil über einer Subduktionszone. Niedrige Spurenelement-Konzentrationen zeigen einen geringen Einfluss der abtauchenden Platte an.

Die Spurenelement-Konzentrationen der Gabbros sind ebenfalls niedrig, mit etwa 0.5 - 10-fach chondritischen SEE-Konzentrationen und mit variablen SEE-Mustern ($(La/Yb)_c$ = 0.25 - 2.6). Analog zu den Vulkaniten der IA-Gruppe haben alle Gabbros eine negative Nb-Anomalie mit Nb/La = 0.01 - 0.31. Die initialen ϵ_{Nd} Werte der Gabbros variieren zwischen +4.8 und +7.1, mit einem Mittelwert von +5.9, und sind damit identisch mit denen der IA-Vulkanite.

Bei den untersuchten Mantelgesteinen handelt es sich um teilweise serpentinisierte Dunite und Harzburgite, die alle durch hohe Mg/Si- und niedrige Al/Si-Verhältnisse gekennzeichnet sind. Dies zeigt einen refraktären Charakter an und steht in guter Übereinstimmung mit den hohen Cr-Zahlen (Cr#) der Spinelle (bis zu Cr# = 0.83), auf deren Basis der Aufschmelzgrad der residuellen Mantelgesteine berechnet wurde. Dieser beträgt etwa 25 %.

Die geochemische Zusammensetzung und die petrologischen Daten der Ultramafite und Gabbros lassen sich am besten erklären, wenn man für die Entstehung dieser Gesteine einen zweistufigen Prozess annimmt. In einer ersten Stufe entstanden die ultramafischen Kumulate unter hohem Druck in einer Magmenkammer an der Krustenbasis, hauptsächlich durch Klinopyroxen-Fraktionierung. Bei dieser Magmenkammer handelte es sich um ein offenes System, dem von unten laufend neue Schmelze zugeführt wurde, und aus dem im oberen Bereich evolviertere Schmelzen geringerer Dichte entwichen. Diese evolvierten Schmelzen stiegen in flachere krustale Bereiche auf und bildeten dort meist isolierte Intrusionskörper. Diese Intrusionskörper erstarrten ohne Magmen-Nachschub, weshalb petrographisch sehr unterschiedliche Gesteine entstehen konnten. Eine geochemische Modifikation der abkühlenden Schmelzen erfolgte allerdings durch die Assimilation von Nebengestein. Da innerhalb der Gabbros keine signifikante Variation der initalen ϵ_{Nd} Werte existiert, handelte es sich bei dem assimilierten Material hauptsächlich um vulkanische Gesteine des ATCO und nicht um ältere, möglicherweise kontinentale Kruste.

Abstract

The late Neoproterozoic (570 Ma) Agardagh Tes-Chem ophiolite (ATCO) in Tuva, Central Asia, southwest of Lake Baikal (50.5° N, 95° E), marks the northwestern border of the Tuva-Mongolian microcontinent. The ophiolite was obducted during the accretion of the Central Asian Mobile Belt, which represents one of the largest accretionary complex on Earth. We report electron and ion microprobe, major element, trace element and isotopic data for a variety of volcanic, plutonic and mantle rocks from the ATCO and outline a model suitable to explain the geochemical and petrological data in a comprehensive way.

The volcanic rocks of the ATCO are subdivided by means of their trace element and isotopic compositions into island arc related rocks (IA-rocks), back-arc basin related basalts (BAB-rocks) and exotic rocks, which are mainly late-stage dykes. The majority of the volcanic rocks analyzed belong to the island arc related group and are high-alumina basalts and basaltic andesites. They were derived from an evolved parental magma (Mg# $\geq$0.60, Cr~180 µg/g, Ni~95 µg/g), predominantly by clinopyroxene fractionation. The parental magma developed from a primary mantle melt by fractionation of about 12 % of an olivine + spinel assemblage. The IA-rocks have high abundances of incompatible trace elements (light-(L)-rare-earth element (REE) abundances up to 100 times chondritic, chondrite-normalized $(La/Yb)_c$ = 14.6 - 5.1) and negative Nb-anomalies (Nb/La = 0.37 - 0.62), but low Zr/Nb ratios (7 - 14). Initial ϵ_{Nd} values are around +5.5, initial Pb isotopic compositions are $^{206}Pb/^{204}Pb$ = 17.39 - 18.45, $^{207}Pb/^{204}Pb$ = 15.49 - 15.61, $^{208}Pb/^{204}Pb$ = 37.06 - 38.05. Enrichment of large-ion lithophile elements within this group is significant with Ba/La = 11 - 130. The BAB-rocks are most likely derived from the same depleted mantle source as the IA-rocks but underwent higher degrees of melting (8-15 %) and are not influenced by slab-derived components. They have lower abundances of incompatible trace elements, flat REE patterns ($(La/Yb)_c$ = 0.6 - 2.4) and higher initial ϵ_{Nd} values (+7.8 to +8.5). Negative Nb anomalies are absent (Nb/La = 0.81 - 1.30), but Zr/Nb is high (21 - 48).

At least three components are necessary to explain the geochemical evolution of the volcanic rocks of the ATCO: (1) an enriched, ocean-island like component characterized by high Nb concentration (up to 30 µg/g), an absent negative Nb anomaly, a low Zr/Nb ratio (~6.5), a low ϵ_{Nd} value (around 0), and radiogenic $^{206}Pb/^{204}Pb$, $^{207}Pb/^{204}Pb$ and $^{208}Pb/^{204}Pb$; (2) a back-arc basin component similar to N-MORB with a flat REE pattern and a high ϵ_{Nd} value around +8.5, and (3) an island arc component derived from a depleted mantle source which was modified by the downgoing slab. Crystal fractionation superimposed on mixing and source contamination by subducted sediments is suitable to explain the observed geochemical data. The most likely geodynamic environment to produce these characteristics is a young, intra-oceanic island arc system and an associated back-arc basin.

Plutonic rocks investigated during this study comprise ultramafic cumulates (wehrlites and pyroxenites) as well as a variety of gabbroic rocks ranging from olivine-gabbros to diorites. The geochemical characteristics of the mafic plutonic rocks are different compared to the volcanic rocks and are therefore suggestive of representing a later stage during the evolution of the ATCO.

Trace element abundances in clinopyroxene from ultramafic cumulates are extremely low between 0.1 and 1 times chondritic for REE, with strongly LREE depleted patterns ($(La/Yb)_c$ = 0.27 - 0.52). Calculated equilibrium melts of ultramafic cumulates suggest a boninitic primary magma which was generated in the previously depleted mantle wedge above the subduction zone, but overall low trace element abundances indicate a negligible slab influence.

Trace element abundances in gabbroic rocks are also low and REE concentrations are between about 0.5 and 10 times chondritic with both LREE-depleted and LREE-enriched patterns ($(La/Yb)_c$ = 0.25 - 2.6). Comparable to the volcanic rocks with island arc affinity, all gabbros have negative Nb anomalies with Nb/La = 0.01 - 0.31. Initial ϵ_{Nd} values vary between +4.8 and +7.1 with an average value (+5.9) identical to the average ϵ_{Nd} value of the IA-rocks (+ 5.5).

Mantle rocks analyzed are serpentinized dunites and harzburgites. They are characterized by high ratios of whole-rock Mg/Si, but low Al/Si, indicating a highly refractory character. This is consistent with high Cr# in dunite and harzburgite spinel (up to 0.83). The total degree of melt extraction from residual mantle rocks was estimated to have been about 25 %, based on spinel compositions.

The occurrence of highly residual mantle rocks, associated with ultramafic cumulates and both depleted and evolved gabbroic rocks is explained by assuming a two-stage magmatic process. First, ultramafic cumulates were formed at the crust-mantle boundary within a deep-level, open-system magma chamber, where melts from the mantle wedge passed on their way to the crust. Subsequently, more evolved magmas with lower densities were periodically expelled from this deep-level magma chamber to form mostly isolated (”trapped”), smaller intrusions at shallower crustal levels. These intrusions crystallized without remarkable replenishment, thus forming a wide variety of gabbroic rocks within a small region. However, trace element and isotopic modifications of crystallizing melts occured during assimilation of pre-existing island arc crust, which is represented by the volcanic rocks of the ATCO.

Chapter 1: Introduction

1.1 Purpose

Asia accomodates the largest coherent accretionary belt on Earth, the so called Central Asian Mobile Belt (CAMB). This orogen extends from the northern Ural mountains southeastwards to central Mongolia and China and from there farther to the east, terminating close to the Pacific ocean (Fig. 1). Sengör et al. (1993) estimated that Asia‘s crust grew by about 5.3 million square kilometre during Palaeozoic times, which is about 12 % of the present day‘s surface of Asia, or ~ 3.5 % of the present day‘s solid surface of the Earth. They further suggested that roughly half of this crust was newly extracted from the Earth‘s mantle, predominantly by supra-subduction zone melting and island arc formation. Such enormous amounts of melt extraction from the mantle are expected to have left incisive marks on its thermal and chemical structure, which should be preserved in ophiolites accreted to the CAMB during crustal evolution.

The aim of the present thesis was the investigation of an ophiolite zone located in the central part of the CAMB (Fig. 1). This so called Agardagh Tes-Chem ophiolite (ATCO) was accreted to the northwestern edge of the Tuva-Mongolian Microcontinent (TMM) during early Palaeozoic times, and thus during the early evolution of the CAMB. It therefore provides a unique opportunity to study crust-formation processes operating on a large scale and to evaluate their consequences on the chemical structure of the Earth‘s mantle. The study focuses on the petrological and geochemical investigation of a variety of ultramafic to intermediate plutonic and volcanic rocks, with the objective to outline a geodynamic and petrogenetic model suitable to explain the observed data in a coherent sense. Special attention is drawn on supra-subduction zone melting and subsequent magma evolution that occurred by crystal fractionation, magma mixing and crustal assimilation.

The individual chapters of the thesis are manuscripts either published (Chapter 2) or submitted to international earth science journals (Chapters 3 and 4).

Fig. 1 Location and dimension of the late Neoproterozoic to Palaeozoic Central Asian Mobile Belt (CAMB). The position of the Agardagh Tes-Chem ophiolite (ATCO) is shown as a small black box (arrow)

1.2 Ophiolites

Since the Penrose conference held by the Geological Society of America in 1972, an ophiolite is defined as an assemblage of plutonic and volcanic ultramafic and mafic rocks, associated with deep sea sediments (cherts). A simplified and schematic ophiolite succession is shown in Fig. 2 and comprises residual mantle rocks, ultramafic cumulates, mafic plutonic rocks (mainly gabbros), a sheeted dyke complex, pillow lavas and overlying pelagic and sometimes shallow marine sediments. Defined in 1813 by Brongniart as serpentinite matrix, it was late in the nineteenfifties, after the breakthrough of plate tectonic theory (Wegener, 1929), that ophiolite genesis was directly linked to sea floor spreading (e.g. DeRoever, 1957; Brunn, 1959; Hess, 1965). This analogy is now widely accepted, although the ophiolite concept was meanwhile extended to subduction zone environments (for review see Moores, 1982 and Shervais, 2001).

Due to their origin in oceanic basins, ophiolites play a crucial role in deciphering the geochemical signature and evolution of the Earth‘s mantle through time, as they are the only existing remnants of magmatic activity in ocean basins in the past. A principle question, therefore, arises whether ophiolite occurrences are related to a „real“ mid-ocean ridge spreading environment, or to supra-subduction zone environments, in which several configurations lead to the formation of mafic crust, and therefore to ophiolite generation (e.g. fore-arc spreading, initial arc magmatism, intra-arc rifting, back-arc spreading).

Besides their relevance in elucidating ancient mantle signatures, ophiolite occurrences are also important for plate tectonic reconstructions. In this context, ophiolite belts that occur in orogenic belts are usually regarded as remnants of former ocean basins, and thus are lithological markers of plate boundaries (suture zones).

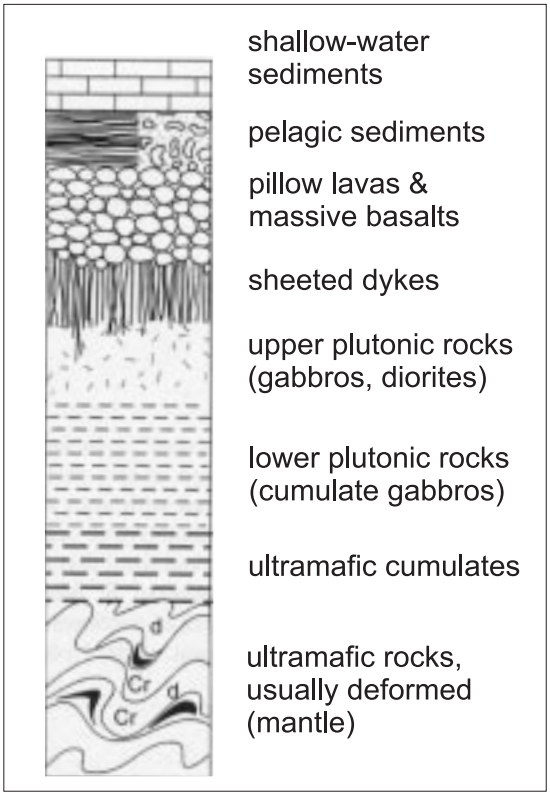

Fig. 2 Schematic diagram showing a complete ophiolite section (from Moores, 1982)

1.3 Evolution of Central Asia

The origin and evolution of the huge Central Asian accretonary orogen is subject to controversial discussions and was the objective of many regional studies carried out in recent years.

It has been proposed that the CAMB represents an association of microcontinents, assumed to be mainly Precambrian in age (Berzin et al., 1994; Mitrofanov & Kozakov 1993; Coleman, 1989). The origin of these microcontinents is unclear in most cases, and some controversy exists whether they are fragments derived from Gondwana (Mossakovsky et al., 1993; Didenko et al., 1994) or from the Siberian craton (Berzin et al., 1994), or both. Based on palaeomagnetic data and stratigraphic correlations it was shown that some microcontinents (e.g. the Tarim- and Mongolia blocks) were most likely separated from Gondwana during late Riphean and Vendian times (Berzin et al., 1994). The ages of the microcontinents are not well constrained, and radiometric age data range from 1.1 Ga to 2.2 Ga (Berzin et al., 1994). However, recent studies by Salnikova et al. (2001) have shown that the high-grade metamorphic rocks of the Tuva-Mongolian

microcontinent adjacent to the ATCO (Fig. 4) are significantly younger than previously proposed (1.1 - 2.0 Ga; Berzin et al., 1994), with the oldest zircon age being 536 ± 6 Ma. It is therefore likely that several other microcontinents are also younger than commonly suggested. This is because age relationships in Central Asia have often been derived from metamorphic grades in the regional literature, such that high grade metamorphic rocks were typically assumed to be either Proterozoic or Archaean in age. This may be a grave misinterpretation. The collision of microcontinents and their accretion to the Siberian craton began during Neoproterozoic times, due to the closure of the Palaeoasian Ocean (Belichenko et al., 1994; Melnikov et al., 1994). Subduction zone processes led to the accretion of volcano-sedimentary successions which now interconnect the older crustal blocks. According to Zorin et al. (1994), the collision of the active margin of the Tuva-Mongolian Microcontinent with the passive margin of the Siberian craton occurred during the Caledonian orogeny. This event may have been responsible for the obduction of the ATCO.

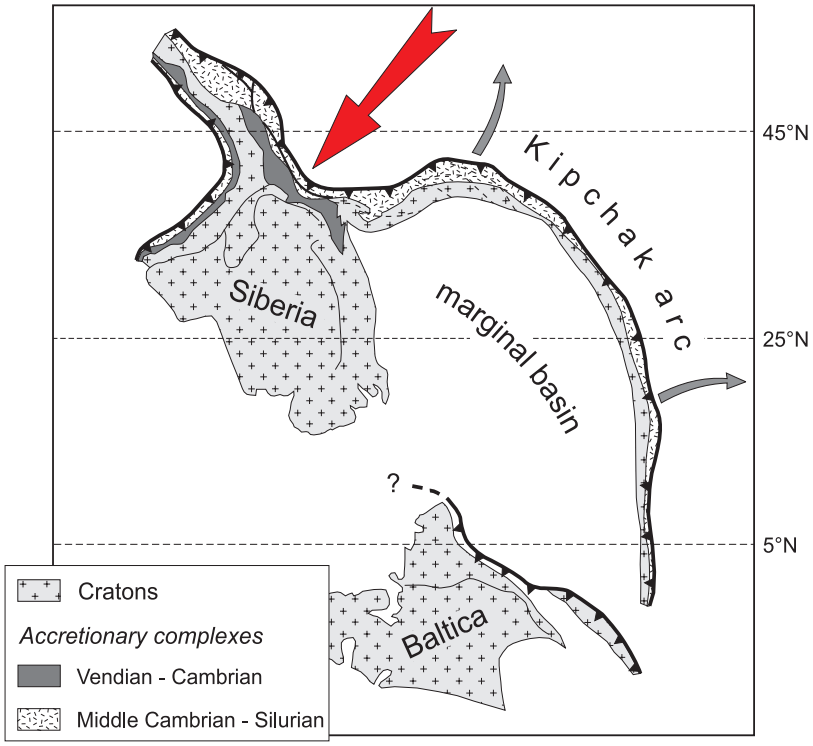

Fig. 3 Geodynamic situation in „Central Asia“ during middle Silurian times (~ 430 Ma) according to the model of Sengör et al. (1993). Arrow: estimated position of the ATCO

Another model explains the evolution of the CAMB in terms of a single, large subduction-accretion system operating for a long time from Neoproterozoic to late Palaeozoic times (Sengör et al., 1993). Comparable to the present-day circumpacific subduction system, it was proposed that continuous accretion of sediments, extended island arc magmatism and collisional processes led to the present-day rock associations and structures of the CAMB. In Fig. 3, the possible geodynamic situation in Central Asia is shown for middle Silurian times (~ 430 Ma), according to the model of Sengör et al. (1993). At this time, the ATCO was already accreted because of its significantly older age of 569.6 ± 1.7 Ma (Pfänder et al., 1998). Although this model is suitable to explain the widespread occurrence of metamorphic, volcano-sedimentary and magmatic rocks in Central Asia, the existence and involvement of distinct microcontinents is not constrained.

Large ophiolite zones are known in Central Asia where they occur primarily as E-W trending belts (Fig. 4; Avdeyev 1984; Kovalenko et al. 1996a, b; Zonenshain and Kuzmin, 1978; Kepezhinskas 1986; Kepezhinskas et al. 1991; Buchan et al., 2001). However, a consistent interpretation of these ophiolites and their significance for the accretionary history of Central Asia is an outstanding problem, simply due to the lack of a comprehensive data base. Basically these ophiolites are interpreted as remnants of the Palaeoasian Ocean (Khain et al. 1997), but their detailed geodynamic origin, i.e. mid-ocean ridge-like oceanic crust or island arc related crust, is largely unknown. This is especially problematic, since the ophiolites are important in deciphering the evolution of the CAMB because they mark suture zones tracing former plate boundaries. A few older papers and several recent publications (Kephezinskas et al., 1991; Kovalenko et al, 1996a; Buchan et al., 2001; Pfänder et al., 1998; Salnikova, pers. comm.) have suggested that most of the ophiolites are very similar in age (Fig. 4). This observation makes the existence of a large, coherent ocean basin more probable than the existence of several small basins developing during different times and therefore support the model proposed by Sengör et al. (1993). Nevertheless, the processes which led to the formation of these ophiolites and the nature of their corresponding mantle sources are still obscure.

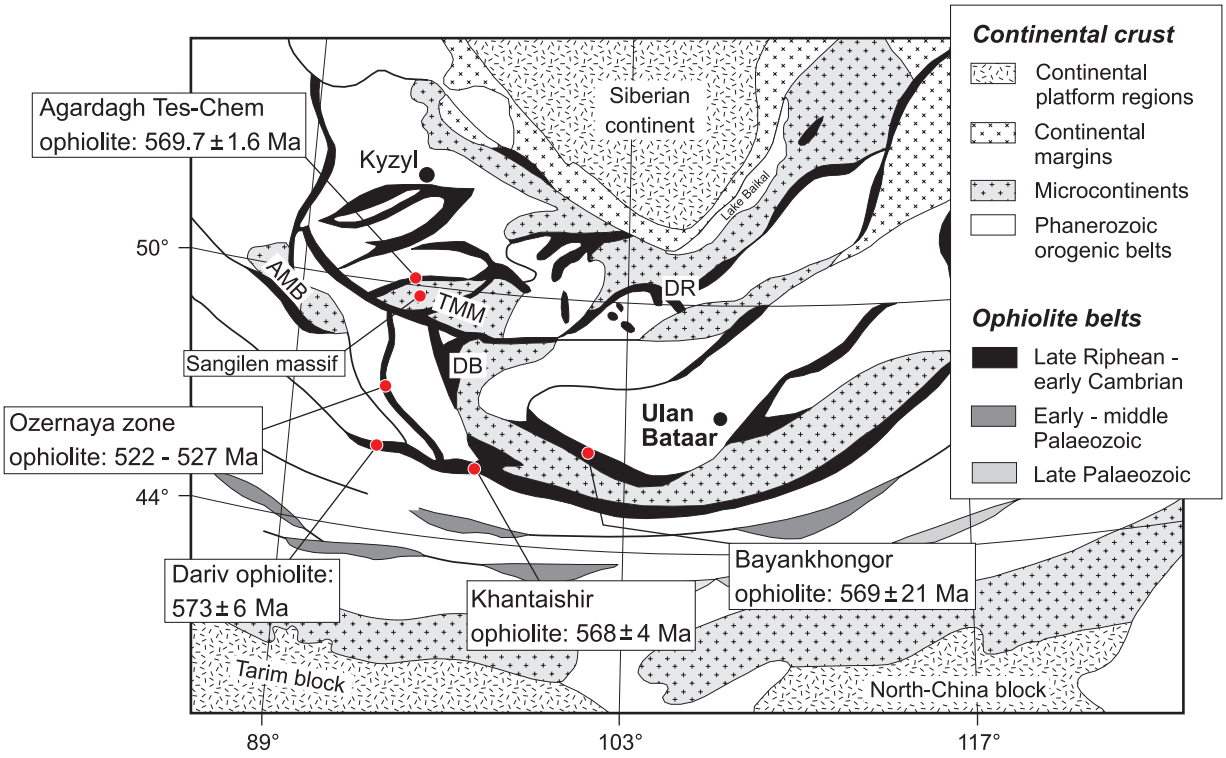

Fig. 4 Ophiolite belts in Central Asia. Ages are: Agardagh Tes-Chem: Pb-Pb zircon (Pfänder et al., 1998), Ozernaya: Sm-Nd (Kovalenko et al., 1996a), Dariv and Khantaishir: U-Pb zircon (Salnikova, pers. comm.), Bayankhongor: Sm-Nd (Kepezhinskas et al., 1991). Microcontinents: AMB: Altai-Mongolia block, DB: Dzabhanian block, DR: Dzhida region, TMM: Tuva-Mongolia Microcontinent

1.4 Summary of chapters 2 - 4

Chapter 2 of the present thesis describes the analytical procedures applied to the measurement of most trace elements used for this study (except a few elements measured either by XRF or ICP-MS, see below). Although this chapter gives a basic methodological overview of multi ion-counting spark source mass spectrometry (MIC-SSMS), special emphasis is on the detailed analytical procedure of low-concentration Y, Zr and Nb measurements. This is because the matrix of the most depleted gabbros investigated caused significant spectral interferences on the signals of ^{91}Zr and ^{93}Nb. It was therefore necessary to improve the existing MIC-SSMS method and to develop a technique which permits the highly precise determination of low Nb and Zr concentrations in the ng/g range. By applying a very small slit, long measuring times and a mathematical correction for isobaric interferences, a detection limit of 0.005 µg/g was finally achieved for Zr and Nb, and an accuracy better than 10 % for low-concentration samples compared to international reference materials. These improvements are described in chapter two and were published in *Fresenius Journal of Analytical Chemistry, 364, 376-380, 1999*.

In Chapter 3, the magmatic evolution of the volcanic rocks of the ATCO is discussed on the basis of geochemical and isotopic investigations. It is shown that the ATCO developed as part of an intra-oceanic island arc back-arc system. The island arc volcanic rocks are characterized by negative Nb anomalies associated with an enrichment in large-ion lithophile elements (LILE) and positive initial $\epsilon_{Nd(570)}$ values of around +5.5. Back-arc basin basalts have flat or slightly depleted rare-earth element (REE) patterns, highly positive initial $\epsilon_{Nd(570)}$ values up to +8.5, whereas negative Nb anomalies are absent. The observed isotopic and trace element characteristics of the ATCO volcanic rocks can be explained by mantle source contamination caused by subducted, partly continental sediments. Magma ascent, mixing and crystal fractionation modified the primary melt signatures before the upper volcanic - volcanoclastic part of the ATCO crust developed. Chapter 3 was submitted for publication to *Contributions to Mineralogy and Petrology*.

Chapter 4 outlines the evolution of the mantle and lower, plutonic part of the mafic arc crust in the ATCO. Electron and ion microprobe mineral investigations, combined with whole-rock trace element and isotopic data, demonstrate that the source of the primary magmas in the ATCO was highly refractory in a petrological sense, and strongly depleted in a geochemical sense. Residual mantle rocks are therefore characterized by high whole-rock Mg/Si ratios and low Al/Si ratios, and by high Cr# in residual spinel (up to 0.83). Melting of this source led to the formation of boninitic primary melts with highly depleted REE patterns. These melts were pooled in a deep-level, open system magma chamber at the base of the crust, and close to the back-arc region of the arc system. Fractionation led to the formation of ultramafic cumulates and more evolved magmas were expelled to shallower crustal levels to build up gabbroic intrusions. It is shown that the gabbroic rocks of the ATCO represent such an intrusion which crystallized in a nearly closed

system and where trace element and isotopic modifications occurred by wall-rock assimilation of pre-existing island arc crust. Chapter 4 is the most extensive part of the thesis and will be submitted to *Journal of Petrology* in a slightly condensed form.

1.5 Outlook and remaining problems

Geoscientists are far away from understanding the geodynamic evolution of Central Asia in a comprehensive way. Nevertheless, the present data shed some light on the processes which led to the formation of a small fragment of mafic crust in the CAMB and thus may be at least partly representative for the formation of adjacent mafic crustal fragments. A remaining problem concerning the studied region is a more detailed investigation of the slightly younger (512 - 447 Ma; Pfänder et al., 1998) Tannuola island arc complex to the north of the ophiolite. This well exposed complex seems to be more evolved compared to the ATCO, as inferred from the dominant occurrence of felsic island arc rocks (gabbrodiorites, diorites, tonalites, andesites and rhyolites). A major question therefore is, whether the ATCO and the Tannuola island arc are genetically related and whether the Tannuola arc represents a later, more mature, stage of evolution of the same island arc system.

Another major objective for future research should be on the principal differences between oceanic and ophiolite gabbros, since recent trace element investigations suggest different mechanisms for the evolution of oceanic and ophiolite gabbros (Chapter 4). If it emerges that these different trace element characteristics are inherited from the mantle sources, the now widely accepted analogue between ophiolite complexes and oceanic crust may appear in a new light.

1.6 Methods

The petrological and geochemical investigation of mafic volcanic and plutonic rocks of the ATCO is based on a number of well established analytical methods, which will be described very briefly in the following.

Major and trace element concentrations for volcanic and plutonic rocks were determined using a Philips PW 1404 X-ray fluorescence spectrometer at Universität Mainz. Fused pellets for major element determination were produced by melting 0.8 g sample powder with 4.8 g flux (Li-tetraborate). Trace element concentrations were determined on pressed powder pellets consisting of 6 g sample powder and 25 drops of resin. For major elements, the reproducibility of the method is better than 1 % (see appendix). For trace elements, the reproducibility and detection limits are listed in the appendix of this chapter.

Low-abundant trace elements, such as Th, U, REE and high-field strength elements (HFSE; e.g. Zr, Hf, Nb) were remeasured using multi ion-counting spark-source mass spectrometry as mentioned above and as described in Chapter 2. A selection of more enriched, volcanic rocks was sent to Memorial University, St. Johns, Newfoundland, Canada, where trace element compositions were determined by ICP-MS according to the technique described in Jenner et al. (1990).

Sr, Nd and Pb isotopic compositions and Rb, Sr, Nd and Sm concentrations of whole-rock powders and mineral separates were measured on Finnigan MAT 261 thermal-ion mass-spectrometers at Max-Planck-Institut für Chemie in Mainz. Concentrations were determined by applying the isotope-dilution method and by using mixed ^{150}Nd-^{149}Sm and ^{84}Sr-^{85}Rb tracers. Rhenium double filament arrangements were used for Nd, Sm and Rb measurements, and tungsten single filament arrangements with TaF_5 were used for Sr measurements. Pb was loaded and measured with silica-gel on rhenium single filaments. Pb isotopic compositions were partly determined using the highly precise triple-spike technique developed by Galer (1999). To correct for instrumental mass fractionation, this technique requires the run of a spiked sample aliquot prior to Pb isotopic measurement, but improves the precision of the Pb isotopic ratios to about 100 ppm ($2\sigma_m$). This is about a factor of 10 better than for conventional procedures. Where the triple spike technique was not applied, correction for mass fractionation was performed conventionally by external calibration.

The age of the ophiolite was established by the dating of single zircons from a plagiogranite sample, using the single zircon evaporation technique described by Kober (1986). Lead was masured using a Finnigan MAT 261 thermal-ion mass spectrometer at Max-Planck-Institut in Mainz. The resulting ^{207}Pb/^{206}Pb evaporation age is 569.6 ± 1.7 Ma (Pfänder et al, 1998) and within error close to a gabbro whole-rock Sm-Nd isochron age of 546 ± 18 Ma (Chapter 4).

Microanalytical techniques used during this study were electron microprobe and ion microprobe. Electron microprobe analyses of major elements and some trace elements (Ni, Cr, Na) were carried out on a Jeol JXA-8900 RL microprobe at Universität Mainz using 15kV acceleration voltage, 12 nA probe current and a beam size of 2 µm. Several samples were measured for clinopyroxene trace element compositions using a modified Cameca IMS-3f secondary ion mass spectrometer (SIMS) at the Max-Planck-Institut in Mainz. Ionization was performed using negative oxygen ions, an acceleration voltage of 12.5 kV and a probe current of 10 nA. The spot size for these conditions was 15-20 µm. An energy offset of - 80 eV was used to suppress multiply charged interfering ions and molecules.

1.7 References

Avdeyev, A.V. (1984). Ophiolite zones and the geologic history of Kazakhstan from the mobilist standpoint. *Intern. Geol. Rev.*, **26**, 995-1004.

Belichenko, V.G.; Sklyarov, E.V.; Dobretsov, N.L. & Tomurtogoo, O. (1994). Geodynamic map of Paleoasian ocean: Eastern segment. *Russian Geol. Geophys.*, **35**, 23-32.

Berzin, N.A.; Coleman, R.G.; Dobretsov, N.L.; Zonenshain, L.P.; Xuchang, X. & Chang, E.Z. (1994). Geodynamic map of the western part of the paleoasian ocean. *Russian Geol. Geophys.*, **35**, 44682.

Brongniart, A. (1813). Essai de classification minéralogique des roches mélanges. *J. Mines*, **XXXIV**, 199.

Brunn, I.H. (1959). La dorsale médio-atlantique et les épanchements ophiolitiques. *C.R. Soc. géol. France*, **8**, 234-236.

Buchan, C.; Cunningham, D.; Windley, B.F. & Tomurhuu, D. (2001). Structural and lithological characteristics of the Bayankhongor Ophiolite Zone, Central Mongolia. *J. Geol. Soc. Lond.*, **158**, 445-460.

Coleman, R.G. (1989). Continental growth of northwest China. *Tectonics*, **8**, 621-635.

DeRoever, W.P. (1957). Sind die alpinotypen Peridotitmassen vielleicht tektonisch verfrachtete Bruchstücke der Peridotitschale? *Geol. Rundschau*, **46**, 137-146.

Didenko, A.N.; Mossakovskii, A.A.; Pecherskii, D.M.; Ruzhentsev, S.V.; Samygin, S.G. & Kheraskova, T.N. (1994). Geodynamics of the Central-Asian Paleozoic Oceans. *Russian Geol. Geophys.*, **35**, 48-61.

Galer, S.J.G. (1999). Optimal double and triple spiking for high precision lead isotopic measurement. *Chem. Geol.*, **157**, 255-274.

Hess, H.H. (1965). Mid-ocean ridges and tectonics of the sea floor. *In: Proc. of the 17th Symp. of the Colston Research Society. Butterworths, London*, 317-334.

Jenner, G.A.; Longerich, H.P.; Jackson, S.E. & Fryer, B.J. (1990). ICP-MS - A powerful tool for high-precision trace-element analysis in earth sciences - evidence from analysis of selected USGS reference samples. *Chem. Geol.,* **83**, 133-148.

Kepezhinskas, K.B. (1986). Structural-metamorphic Evolution of late Proterozoic Ophiolites and Precambrian basement in the central Asian foldbelt of Mongolia. *Precambr. Res.*, **33**, 209-223.

Kepezhinskas, P.K.; Kepezhinskas, K.B. & Puchtel, I.S. (1991). Lower Paleozoic Oceanic Crust in Mongolian Caledonides: Sm-Nd Isotope and Trace Element Data. *Geophys. Res. Lett.*, **18**, 1301-1304.

Khain, V.E.; Gusev, G.S.; Khain, E.V.; Vernikovskym, V.A. & Volobuyev, M.I. (1997). Circum-Siberian Neoproterozoic ophiolite belt. *Ofioliti*, **22**, 195-200.

Kober, B. (1986). Whole-grain evaporation for $^{207}Pb/^{206}Pb$-age-investigations on single zircons using a double-filament thermal ion source. *Contrib. Mineral. Petrol.*, **93**, 482-490.

Kovalenko, V.I.; Puchtel, I.S.; Yarmolyuk, V.V.; Zhuravlev, D.Z.; Stosch, H. & Jagoutz, E. (1996a). The Sm-Nd isotopic systematics of ophiolites in the Ozernaya Zone (Mongolia). *Stratigraphy and Geological Correlation*, **4**, 107-113.

Kovalenko, V.I.; Yarmolyuk, V.V.; Kovach, V.P.; Kotov, A.B.; Kozakov, I.K. & Salnikova, E.B. (1996b). Sources of Phanerozoic granitoids in central Asia: Sm-Nd isotope data. *Geochem. Int.*, **34**, 628-640.

Melnikov, A.I.; Mazukabzov, A.M.; Sklyarov, E.V. & Vasiliev, E.P. (1994). Baikal rift basement: structure and tectonic evolution. *Bull. Centr. Rech. Explor. Prod. Elf Aquitaine*, **18**, 99-122.

Mitrofanov, F.P. & Kozakov, I.K. (1993). Precambrian in younger fold belts. *In: Precambrian geology of the USSR. Rundqvist, D.V. & Mitrofanov (eds.)*, 443-498.

Moores, E.M. (1982). Origin and Emplacement of Ophiolites. *Rev. Geophys. Space Phys.*, **20**, 735-760.

Mossakovsky, A.A.; Ruzhentsev, S.V.; Samygin, S.G. & Kheraskova, T.N. (1993). The Central Asian fold belt: geodynamic evolution and formation history. *Geotectonics*, **6**, 3-32.

Pfänder, J.A.; Jochum, K.P.; Kröner, A.; Kozakov, I.; Oidup, C. & Todt, W. (1998). Age and geochemical evolution of an early Cambrian ophiolite-island arc system in Tuva, South Central Asia. *In: Generation and Emplacement of Ophiolites Through Time. Geol. Surv. Finland, Spec. Paper,* **26***, 42*.

Salnikova, E.B.; Kozakov, I.K.; Kotov, A.B.; Kröner, A.; Todt, W.; Nutman, A.; Yakovleva, S.Z. & Kovach, V.P. (2001). Age of Palaeozoic granites and metamorphism in the Tuvino-Mongolian massif of the Central Asian Mobile Belt: loss of a Precambrian microcontinent. *Precambr. Res.,* **110**, 143-164.

Sengör, A.M.C; Natal'in, B.A. & Burtman, V.S. (1993). Evolution of the Altaid tectonic collage and Palaeozoic crustal growth in Eurasia. *Nature*, **364**, 299-307.

Shervais, J.W. (2001). Birth, death, and resurrection: The life cycle of suprasubduction zone ophiolites. *G^3*, **2**.

Wegener, A. (1929). Die Entstehung der Kontinente und Ozeane. *4. Aufl., Friedr. Vieweg & Sohn, Braunschweig*.

Zonenshain, L.P. & Kuzmin, M.I. (1978). The Khan-Taishir ophiolitic complex of western Mongolia, its petrology, origin and comparison with other ophiolitic complexes. *Contrib. Mineral. Petrol.*, **67**, 95-109.

Zorin, Y.A.; Belichenko, V.G.; Turutanov, E.Kh.; Mordvinova, V.V.; Kozhevnikov, V.M.; Khozbayar, P.; Tomurtogoo, O.; Arvisbaatar, N.; Gao, S. & Davis, P. (1994). Baikal-Mongol transect. *Russian Geol. Geophys.*, **35**, 78-92.

APPENDIX

Reproducibility and detection limits for major and trace elements determined by XRF on fused (major elements) and powder pellets (trace elements)[1)]

Trace elements

Element	C [µg/g]	R [µg/g]	R [%]	DL [µg/g]
V	220	1.8	0.8	1.1
Cr	435	5.1	1.2	2.1
Co	57	2.3	3.9	1.9
Ni	345	2.9	0.8	1.1
Cu	60	2.2	3.7	0.4
Zn	105	1.5	1.3	1.8
Ga	18	0.7	3.9	1.4
Rb	44	1.0	2.4	1.3
Sr	755	2.5	0.3	1.4
Y	26	0.6	2.4	1.6
Zr	223	1.5	0.7	1.1
Nb	77	0.3	0.4	1.0
Cd	29	0.8	2.8	3.8
Sn	57	0.4	0.8	6.9
Sb	17	0.4	2.4	9.3
Ba	585	3.6	0.6	6.6
La	278	1.9	0.7	3.6
Ce	406	3.7	0.9	9.1
Pr	39	1.9	4.9	2.5
Nd	109	2.1	2.0	5.1
Sm	8	1.8	22.0	6.9
Hf	24	1.2	5.0	2.5
Ta	23	1.0	4.3	3.2
Pb	30	0.6	2.0	2.0
Th	13	0.4	3.1	1.0
U	5	0.3	6.0	1.6

Major elements

Element	C [wt%]	R [wt%]	R [%]
SiO_2	44.2	0.060	0.13
TiO_2	2.17	0.003	0.16
Al_2O_3	12.3	0.031	0.25
Fe_2O_3	12.3	0.014	0.11
MnO	0.19	0.002	0.88
MgO	12.2	0.029	0.23
CaO	10.1	0.016	0.16
Na_2O	2.70	0.016	0.61
K_2O	1.08	0.005	0.45
P_2O_5	0.62	0.003	0.48
Cr_2O_3	0.063	0.000	0.54
NiO	0.043	0.000	0.56

[1)] Data source: home page XRF laboratory, Institut für Geowissenschaften, Universität Mainz: http://www.uni-mainz.de/FB/Geo/Geologie/EMSRFA/RFA.html

C = Concentration, R = Reproducibility, DL = Detection limit

Chapter 2

Determination of Y, Zr and ultra-low Nb in geological material by multi-ion counting spark-source mass spectrometry

Jörg A. Pfänder, Klaus Peter Jochum, Andreas Sassen, Brigitte Stoll,
Petra Maissenbacher, Melanie Murmann

published in Fresenius J. Anal. Chem., 364, 376-380, 1999

Abstract

Precise concentrations of Zr, Y and Nb in the µg/g to ng/g range have been determined in rock samples using multi-ion counting spark-source mass spectrometry (MIC-SSMS). A high resolution method, combined with interference correction on ^{91}Zr and ^{93}Nb for low concentration samples, was applied. An analytical precision of 2-5% for concentrations down to 0.020 µg/g and 10% for lower concentrations was attained. The detection limit is below 0.005 µg/g. By measuring international reference materials, the accuracy of the method was determined to be within about 10% of the recommended values. However, the accuracy of the final concentration is influenced by interference corrections, but the additional error is below 20%. The interference problem is most difficult for Al-rich samples (>15% Al_2O_3), as the interfering molecules are $^{40}Ca^{27}Al^{12}C_2^+$ and $^{27}Al_3{}^{12}C^+$. The accordance between ICP-MS and MIC-SSMS results is worse for low Nb concentrations in the ng/g range. Here, ICP-MS gives systematically lower values than MIC-SSMS. The reason for this discrepancy is not yet clear, but may be caused by Nb loss during chemical treatment of the samples prior to ICP-MS measurements.

2.1 Introduction

Trace elements, such as Zr, Y or Nb, are helpful tools for deciphering the chemical evolution of the Earth through time. These elements have different geochemical affinities during magmatic processes, leading to the enrichment or depletion of various geochemical reservoirs in the Earth [1]. The precise determination of the concentrations of these elements in rocks thus allows conclusions on the processes which lead to their formation. However, the geochemically interesting elements Zr, Y and especially Nb have very low abundances in some rock types, making it difficult or impossible to get precise analyses without time consuming enrichment or cleanup processes. Therefore, the most common method for the determination of these elements is mass spectrometry [2], especially inductively coupled plasma mass spectrometry (ICP-MS) [3-7] and spark-source mass spectrometry (SSMS) [8-10]. As the conventional ICP-MS technique requires the dissolution and chemical treatment of the samples, SSMS allows to bring the sample to the ion source in a solid state. This impedes the problems of insufficient sample decomposition [11] and loss of material during dissolution and chemical separation, which is especially a problem for refractory elements (e.g. Nb, Zr). Otherwise, the SSMS technique requires the mixture of the sample powder with graphite, thus limiting the detection limit as no preconcentration is possible.

In this paper we describe the application of the Multi-Ion Counting Spark-Source Mass Spectrometry (MIC-SSMS) [10] to determine low concentrations of Y, Zr and Nb in depleted rock samples (gabbros and pyroxenites from Central Asia and New Foundland). Special measuring problems arising from interferences on ^{91}Zr and ^{93}Nb are emphasized and a simple correction

method is presented. The reliability of the method is investigated by measuring several geological standard materials. Furthermore, we compare the analytical results to ICP-MS measurements made on some of the same rock samples.

2.2 Sample preparation

Sample preparation is done by mixing 60 mg of powdered rock sample with 30 mg ultrapure graphite powder containing ^{91}Zr as spike isotope for the determination of Zr by isotope dilution [12]. The sample/graphite mixture was homogenized using a ball mill. Then, two rod-shaped electrodes were pressed, each about 6 mm long and 2 mm wide. These electrodes were placed within the ion-source of the mass spectrometer.

2.3 Mass spectrometer

For mass separation, an AEI-MS 702R double-focussing mass spectrometer with Mattauch-Herzog geometry was used (Fig. 1). Ionisation was reached by a pulsed high-voltage AC discharge (spark) between the two sample electrodes. The detection system consists of an array of 20 channeltrons that are connected to a multichannel pulse counter [10]. Signal integration ("counting") on each measuring position was done until a user defined total ion charge (TIC), measured by the monitor system, was reached. This yields more reproducible values than time-related integration. The regulation of the whole system, including magnetic field control for dynamic measurements and data acquisition, is maintained by a personal computer. A slit plate is positioned in front of the channeltron array. For this study the smallest slit size (0.02 mm) was used, reaching a high mass resolution of ~3000 which allows to resolve interfering molecule peaks.

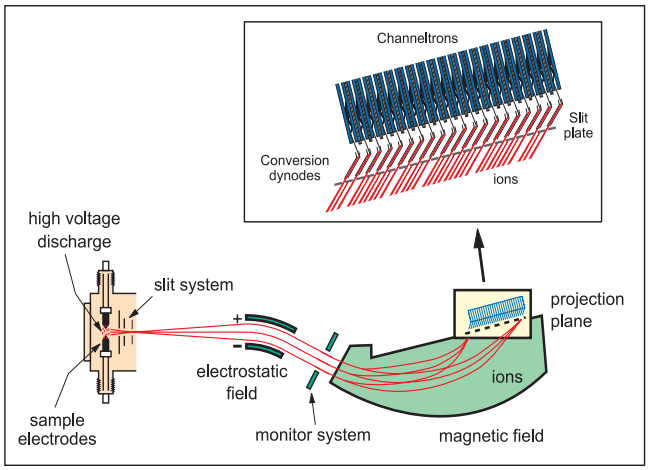

Fig. 1 Scheme of the double-focussing AEI-MS 702R mass spectrometer. Ionisation is reached by a high-voltage AC discharge between the two sample electrodes (25kV, 300Hz pulse repetition rate, 100µs pulse length). The multi-channel ion detection system (channeltron array, above) is positioned within the projection plane of the ion-optic system (Mattauch-Herzog geometry). Note the monitor system between the electrostatic and magnetic field which registers the total ion charge used to normalise the measured counts

2.4 Measuring procedure

From each sample, three blocks of 25 scans were measured. During one scan the following mass positions were measured sequentially: baseline, ^{89}Y, ^{90}Zr, ^{91}Zr, ^{93}Nb, ^{94}Zr, and ^{95}Mo. The TIC for each measuring position was set to 1, 3, 10 or 20 nC, depending on the concentration of the measured element. Corresponding integration times are between 1 and 4 minutes per scan, depending on the intensity and stability of the total ion current. ^{95}Mo was measured to correct the ^{94}Zr-counts for isobaric ^{94}Mo-counts. Typical corrections are below 15%, with higher values up to 40% for samples with Zr concentrations < 1 µg/g (Tab. 1).

2.5 Results

2.5.1 Precision and detection limits

From 25 scans measured per block, we calculated isotope ratio averages for each individual block. Due to the short measuring times during one scan, the standard deviation of these averages is up to 100% for samples with very low concentrations (<0.020 µg/g). However, the reproducibility of the block averages is much better (Fig. 2), giving a typical analytical precision (σ_m of three block averages) of 5% for Y, 2% for Zr, and 5% for Nb concentrations >0.020 µg/g and 10% for Nb concentrations <0.020 µg/g. If significant corrections have to be made due to interfering signals, the uncertainty will be enlarged as is shown below. Detection limits also depend on the intensity of interfering molecule ions, but are below 0.005 µg/g for samples with low interfering signals.

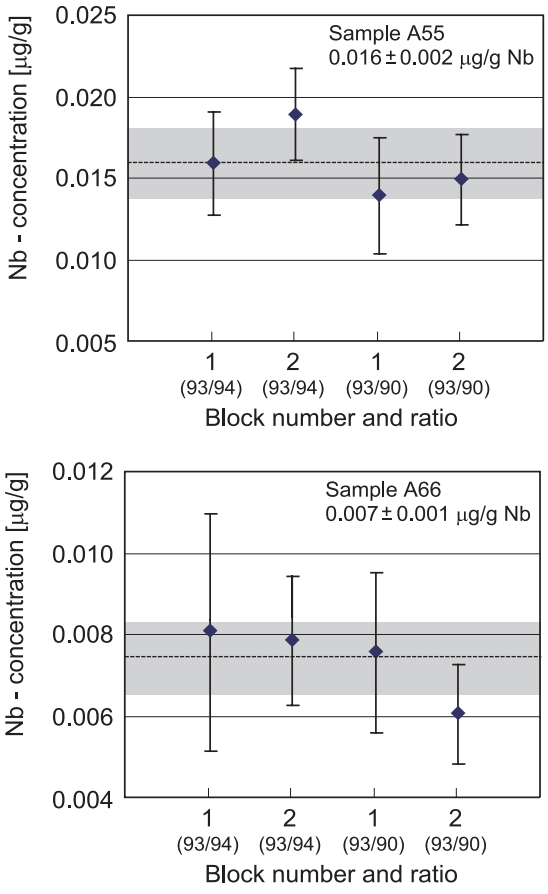

Fig. 2 Variation of block averages shown for Nb concentrations calculated from ^{93}Nb/^{94}Zr and ^{93}Nb/^{90}Zr ratios. The two samples shown are those with the lowest measured Nb concentrations (A55 and A66). Although the errors of the block averages (error bars representing $2\sigma_m$ of 25 scans) are relatively large, the reproducibility of the block averages is much better giving a typical analytical precision (σ_m of block averages) better than 10% for Nb concentrations < 0.020 µg/g. Dotted line: mean of block averages, grey bar: error given as $2\sigma_m$

Table 1 Zirconium concentrations in µg/g as determined by isotope dilution from measured $^{90}Zr/^{91}Zr$ and $^{94}Zr/^{91}Zr$ ratios. Samples are gabbros from Central Asia.

Sample	Zr from $^{90}Zr/^{91}Zr$	Zr from $^{94}Zr/^{91}Zr$	Deviation (%)[a]	^{94}Zr correction from ^{94}Mo (%)	Measured $^{90}Zr/^{94}Zr$[b]
T42	143.7	143.3	-0.3	2.4	2.95 (0)
T16	142.9	146.6	2.6	0.5	3.02 (2)
A57	36.1	33.5	-7.2	0.6	3.13 (6)
A62	18.9	17.3	-8.5	1.3	3.18 (7)
T27b	3.05	3.04	-0.3	4.6	2.97 (0)
T27a	1.72	1.75	1.7	11	3.00 (1)
A35	1.29	1.65[c]	28	14	2.32 (22)[c]
T7	1.13	1.20	6.2	8.4	2.90 (2)
A55	0.890	0.587[c]	-34	42	4.59 (55)[c]
T28	0.538	0.534	-0.7	23	3.00 (1)
A66	0.362	0.374	3.3	20	2.80 (6)

[a] Positive values: concentration from $^{94}Zr/^{91}Zr$ higher than from $^{90}Zr/^{91}Zr$, negative values: vice versa
[b] Natural ratio = 2.96. In brackets: deviation from natural ratio in %
[c] Incorrect value due to incorrect ^{94}Zr measurement (see text)

2.5.2 Interferences and correction method

The measured samples mainly consist of Ca-, Mg-, Fe-, and Al-silicates. The major elements, as well as carbon from the graphite, are responsible for the molecule interferences that occur on ^{91}Zr and ^{93}Nb. In Fig. 3 a magnetic scan spectra of a sample, containing 0.021 µg/g Nb, is shown. Interfering masses are calculated from measured field-differences and are 92.945 amu and 92.952 amu. These masses are best fit by assuming $^{27}Al_3{}^{12}C^+$ (92.9446 amu) and $^{29}Si^{16}O_4{}^+$ (92.9561 amu) as interfering molecules. To test this hypothesis, we measured two samples with similar SiO_2 and Nb concentrations, but strongly different Al_2O_3 contents. Fig. 4a shows the spectrum for sample T27a, which contains 0.051 µg/g Nb and 25% Al_2O_3. The intensity of the interfering signal is sufficiently high to disturb the measurement of ^{93}Nb. By contrast, in sample T27b, which has a similar Nb concentration of 0.045 µg/g but only 5.5% Al_2O_3, the interfering signal is lower than the ^{93}Nb signal (Fig. 4b).

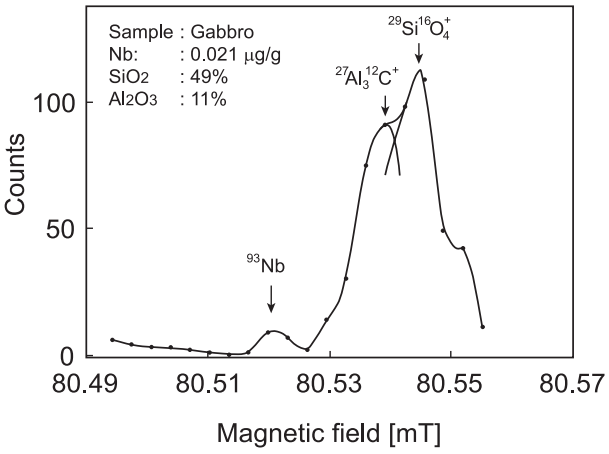

Fig. 3 Magnetic scan spectra of a gabbro sample containing 0.021 µg/g Nb, 49% SiO_2 and 11% Al_2O_3. The interfering double-peak is resolved from the ^{93}Nb-peak and consists most likely of $^{27}Al_3{}^{12}C^+$ and $^{29}Si^{16}O_4{}^+$

A similar problem occurs for the measurement of ^{91}Zr. In this case, the mass difference to the interfering signal is about 0.0384 amu, and the interfering molecule is assumed to be $^{40}Ca^{27}Al^{12}C_2^+$ (90.9441 amu). Thus, the intensity of the interfering signal strongly depends on the Al_2O_3 and CaO content in the sample. A high Al_2O_3 content in sample T27a produces a high interfering signal (Fig. 5a), whereas a low Al_2O_3 content in sample T27b gives a nearly undisturbed ^{91}Zr signal (Fig. 5b).

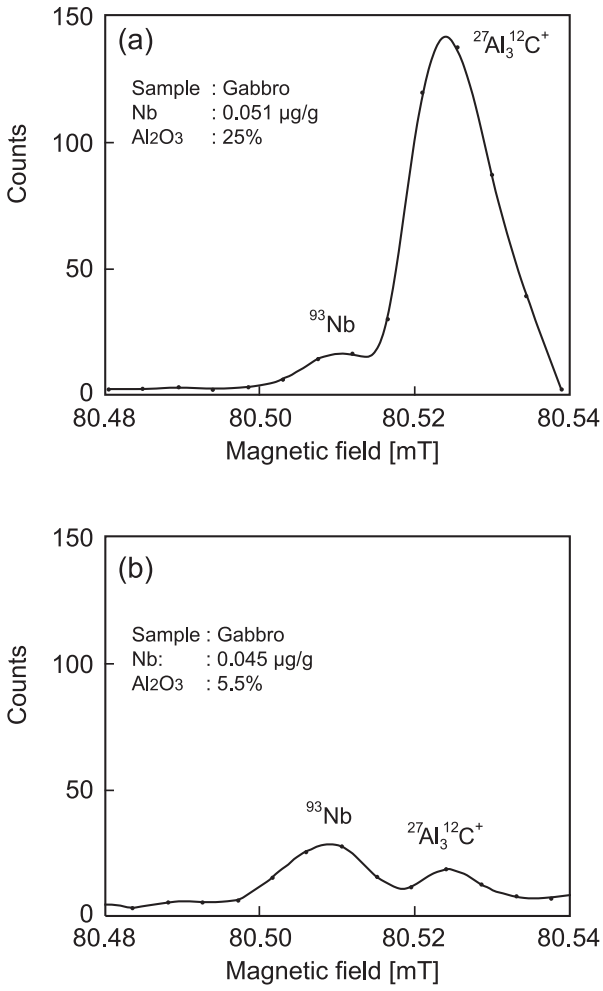

Fig. 4 Magnetic scan spectra of two samples containing nearly the same amount of Nb and SiO_2 but different Al_2O_3 contents of 25% (a) and 5.5% (b). As the intensity of the interfering peak varies strongly with the Al_2O_3 content of the sample, the interfering molecule is rather $^{27}Al_3^{12}C^+$ than $^{29}Si^{16}O_4^+$

To correct for interfering counts on ^{91}Zr and ^{93}Nb, the intensity of the interfering signals was measured during each scan in addition to the masses listed above. The magnetic field differences between ^{91}Zr and $^{40}Ca^{27}Al^{12}C_2^+$ and ^{93}Nb and $^{27}Al_3^{12}C^+$ are -0.0171 mT and -0.0217 mT, respectively. From this, assuming that the shape of molecule and element peaks is identical and mass and intensity independent, we determined the intensity ratios between the peak maximum I_{max} and the peak flank I_s 0.0171 mT and 0.0217 mT next to the peak maximum of an undisturbed peak (Fig. 6). These intensity ratios I_s/I_{max} are 0.069 ± 0.004 and 0.023 ± 0.006 (precision given as σ_m of 50 scans), respectively. Thus, subtracting 6.9% of the counts of the $^{40}Ca^{27}Al^{12}C_2^+$ peak from the ^{91}Zr counts gives the corrected ^{91}Zr value. Subtracting 2.3% of the counts of the $^{27}Al_3^{12}C^+$ peak from the ^{93}Nb counts gives the corrected ^{93}Nb value. Due to variable major element compositions, corrections up to 40% on ^{93}Nb occur for samples with very low Nb concentrations (<0.010 µg/g). The additional error included in the final Nb concentration was calculated from the precision of the correction factor and depends on the required correction as is shown in Fig. 7. It is obvious that for corrections up to 40%, the additional error is below 20% of the final concentration.

2.5.3 Concentrations

From the measured $^{90}Zr/^{91}Zr$ and $^{94}Zr/^{91}Zr$ ratios, two independent Zr concentrations are calculated (Tab. 1) by isotope dilution [12]. In most cases, both values agree within 10%. Exceptions are two samples where the concentrations differ by about 30%. We assume that these deviations are caused by unresolved molecule peaks interfering with ^{95}Mo, therefore overestimating the ^{94}Zr correction, resulting in lower Zr concentrations. Conversely, molecule peaks interfering with ^{94}Zr could yield higher Zr concentrations. For example, the first case is assumed for sample A55 (42% correction on ^{94}Zr), where the measured $^{90}Zr/^{94}Zr = 4.49$ and thus significantly higher than the natural ratio of 2.96. The latter is assumed for sample A35, where the measured $^{90}Zr/^{94}Zr = 2.35$ and thus lower than the natural ratio. Due to this uncertainties, we only used the $^{90}Zr/^{91}Zr$ ratio to calculate Zr concentrations in this study as ^{90}Zr is not disturbed by interfering signals.

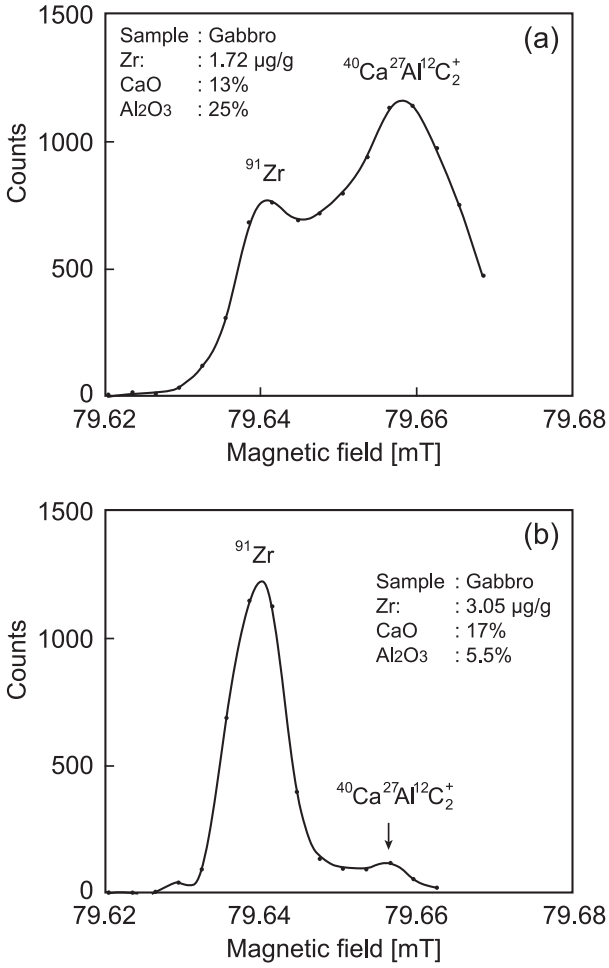

Fig. 5 Magnetic scan spectra of the same samples as in Fig. 4. Both samples have similar Zr and CaO contents but different Al_2O_3 concentrations of 25% (a) and 5.5% (b). The intensity of the interfering peak varies strongly with the Al_2O_3 content which confirms the assumption that the interfering signal is $^{40}Ca^{27}Al^{12}C_2^+$

From the Zr concentration, the concentrations of Y and Nb are calculated from the measured $^{89}Y/^{90}Zr$ and $^{93}Nb/^{90}Zr$ ratios (Tab. 2) using relative sensitivity factors (RSF, see [12]). The RSF resulting from different ion yields for Nb and Y relative to Zr were determined using international standard materials.

2.5.4 Accuracy

Accuracy is defined here as the mean deviation of the measured concentration from the literature value given for international geological reference materials. During this study, the accuracy was monitored by measuring the geological standard materials BHVO-1, BIR-1, JP-1 and DTS-1. The concentrations of Zr, Y and Nb in the first two standards are well known. However, for the last two reference materials only proposed values exist in literature [7, 13, 14, 15]. In Tab. 3, the measured concentrations are compared to literature values. The accordances are generally within 10%, except for the Zr concentration of DTS-1 and the Nb concentration of JP-1.

Table 2 Zr, Y and Nb concentrations in µg/g of gabbros from Central Asia

Sample	Zr (^{90}Zr/^{91}Zr)	Y (^{89}Y/^{90}Zr)	Nb (^{93}Nb/^{90}Zr)
T42	143.7	34.8	13.3
T16	142.9	24.2	11.4
A57	36.1	15.6	0.789
A62	18.9	23.0	0.408
T27b	3.05	7.27	0.045
T27a	1.72	0.852	0.051
A35	1.29	4.41	0.021
T7	1.13	1.88	0.034
A55	0.890	1.46	0.014
T28	0.538	0.979	0.008
A66	0.362	0.662	0.007

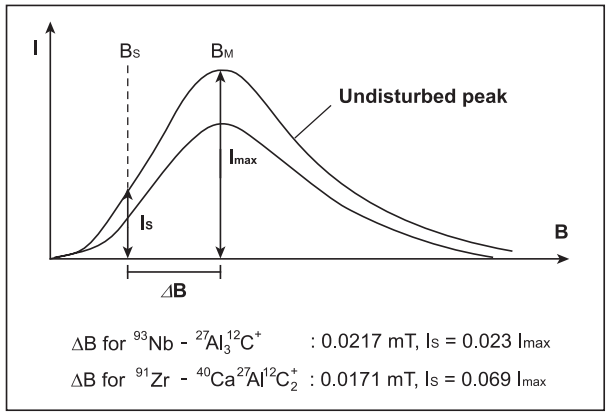

Fig. 6 Determination of the amount of interfering counts on the measuring positions of ^{91}Zr and ^{93}Nb. These measuring positions (B_s) are 0.0171 mT and 0.0217 mT next to the peak maximum of the corresponding molecule peak (B_M). Assuming an intensity independent peak shape, the intensity ratio I_S/I_{max} remains constant and allows to correct the measured ^{91}Zr and ^{93}Nb counts from the measured intensity I_{max} of the molecule peak. The I_s values have been determined using an undisturbed peak and are 0.023 I_{max} for ^{93}Nb and 0.069 I_{max} for ^{91}Zr

2.5.5 Comparison of MIC-SSMS and ICP-MS data

In order to compare MIC-SSMS and ICP-MS results, four samples previously investigated by ICP-MS [16] were measured in this study by MIC-SSMS. The results are shown in Tab. 4. For Zr concentrations > 4 µg/g and for Y concentrations > 2 µg/g, the agreement is within 10% of the MIC-SSMS value. For lower concentrations, the agreement is poor (16 - 34%) and for Nb the agreement is fairly bad. The ICP-MS values for Nb are systematically lower than the MIC-SSMS values by about 20 - 80%, with the largest deviation at the lowest concentration. Y concentrations measured by ICP-MS are also systematically lower than the MIC-SSMS data, whereas for Zr concentrations no systematic trend is recognizable. The reason for the significant deviations, especially for Nb, is not yet clear, but may be caused either by insufficient sample decomposition or Nb loss prior to ICP-MS analysis or by insufficient interference correction during MIC-SSMS

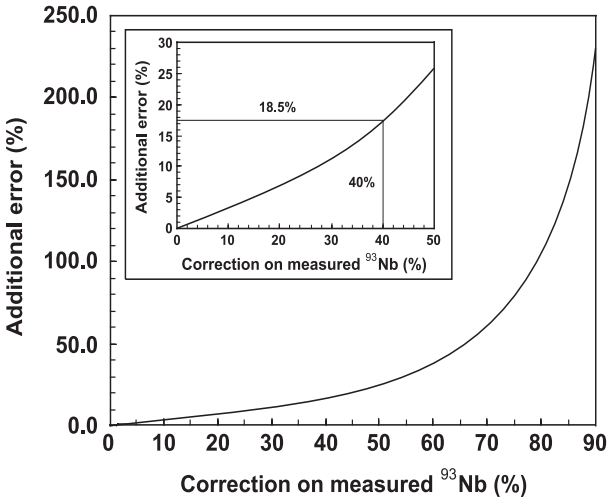

Fig. 7 Additional error contributed to the Nb concentration due to interference correction. This error results from the uncertainty of the correction factor and depends on the extend of correction. For signal corrections up to 40% the additional error is below 20%. Inset: Enlarged part of the same diagram

analysis. However, the counts involved in the Nb peak due to the interfering signal, which was not corrected during the run of these samples, is estimated from magnetic field scans to be maximal 10-15%. This would shift the Nb concentrations to only slightly lower values, but would definitely not explain the large discrepancy between the MIC-SSMS and ICP-MS results. Therefore, we conclude that a significant Nb loss occurred during sample decomposition or chemical treatment of the samples prior to ICP-MS measurement.

Table 3 Comparison of measured Zr, Y and Nb concentrations with literature values for several geological reference materials. From standard BHVO-1 two independent measurements are made (including separate electrode preparation)

Standard	**Zr (µg/g)**		**Y (µg/g)**		**Nb (µg/g)**	
	MIC-SSMS	Lit.	MIC-SSMS	Lit.	MIC-SSMS	Lit.
BHVO-1	178.0	179.0[13]	--	27.6[13]	17.6	19.0[13]
BHVO-1	179.0	179.0[13]	30.2	27.6[13]	18.4	19.0[13]
BIR-1	14.4	14.5[10]-15.5[13]	16.4	16.0[13]-16.8[14]	0.53	0.51[10]-0.60[13]
JP-1	5.51	5.25[15]	0.069	0.065[15]	0.045	0.058[15]
DTS-1	0.36	0.23[14]-0.25[7]	0.041	0.038[7,14]	0.018	0.012[7]-0.032[14]

Table 4 Comparison of Zr, Y and Nb concentrations in gabbros and pyroxenites measured by MIC-SSMS and ICP-MS. Deviation is given in percent deviation from the MIC-SSMS value, positive values indicating higher ICP-MS concentration, negative values indicating lower ICP-MS concentration

Sample	**Zr (µg/g)**			**Y (µg/g)**			**Nb (µg/g)**		
	MIC-SSMS	ICP-MS[16]	Dev. in %	MIC-SSMS	ICP-MS[16]	Dev. in %	MIC-SSMS	ICP-MS[16]	Dev. in %
95-73	0.55	0.64	16	1.80	1.19	-34	0.024	0.004	-83
95-93	0.59	0.40	-32	1.46	1.20	-18	0.023	0.008	-65
U34	4.52	4.86	7.5	2.76	2.70	-2.2	0.062	0.046	-26
95-103	5.90	5.88	-0.4	2.61	2.59	-0.8	0.142	0.110	-23

2.6 References

1. Hofmann AW (1997) Nature 385 : 219-229
2. Becker JS, Dietze HJ (1998) Spectroscopy Europe 10 : 14-20
3. Jenner GA, Longerich HP, Fryer BJ, Jackson SE (1990) Chem Geol 83 : 105-118
4. Poitrasson F, Pin C, Telouk P, Imbert JL (1993) Geostand Newslett 17 : 209-215
5. Garbe-Schönberg CD (1993) Geostand Newslett 17 : 81-93
6. Xie Q, Jain J, Sun M, Kerrich R, Fan J (1994) Geostand Newslett 18 : 53-63
7. Eggins SM, Woodhead JD, Kinsley LPJ, Mortimer GE, Sylvester P, McCulloch MT, Hergt JM, Handler MR (1997) Chem Geol 134 : 311-326
8. Taylor SR, Gorton MP (1977) Geochim Cosmochim Acta 41 : 1375-1380
9. Jochum KP (1997) Spectroscopy Europe 9 : 22-27
10. Jochum KP, Laue HJ, Seufert HM, Dienemann C, Stoll B, Pfänder JA, Flanz M, Achtermann H, Hofmann AW (1997) Fresenius J Anal Chem 359 : 385-389
11. Totland M, Jarvis I, Jarvis KE (1992) Chem Geol 95 : 35-62.
12. Jochum KP, Seufert HM, Midinet-Best S, Rettmann E, Schönberger K, Zimmer M (1988) Fresenius J Anal Chem 331 : 104-110
13. Govindaraju K (1994) Geostandards Newsletter 18 : 1-158
14. Jochum KP, Seufert HM, Thirlwall MF (1990) Chem Geol 81 : 1-16
15. Jochum KP, Jenner G (1994) Fresenius J Anal Chem 350 : 310-318
16. Sassen A (1999) Ph.D. thesis, University Cologne, p 297

Chapter 3

Coupled evolution of back-arc and island arc-like mafic crust in the late Neoproterozoic Agardagh Tes-Chem ophiolite, Central Asia: Evidence from trace element and Sr-Nd-Pb isotope data

Jörg A. Pfänder, Klaus Peter Jochum, Ivan Kozakov, Alfred Kröner, Wolfgang Todt

submitted to Contrib. Mineral. Petrol.

Abstract

The late Neoproterozoic (570 Ma) Agardagh Tes-Chem ophiolite (ATCO) in Central Asia, southwest of Lake Baikal (50.5° N, 95° E), marks the northwestern border of the Tuva-Mongolian microcontinent and was obducted during the accretion of the Central Asian Mobile Belt. We report major element, trace element and isotopic data of volcanic rocks from the ATCO, which are subdivided into island arc rocks (IA-rocks), back-arc basin rocks (BAB-rocks) and late-stage dykes.

The majority of samples analyzed are island arc related high-alumina basalts and basaltic andesites. They were derived from an evolved parental magma (Mg# $\geq$ 0.60, Cr~180 µg/g, Ni~95 µg/g) by predominantly clinopyroxene fractionation. The parental magma developed from a primary mantle melt by fractionation of about 12 % of an olivine + spinel assemblage. The IA-rocks have high abundances of incompatible trace elements (light rare-earth element abundances up to 100 times chondritic, chondrite-normalized $(La/Yb)_n$ = 14.6 - 5.1) and negative Nb-anomalies (Nb/La = 0.37 - 0.62), but low Zr/Nb ratios (7 - 14). Initial ϵ_{Nd} values are around +5.5, initial Pb isotopic compositions are $^{206}Pb/^{204}Pb$ = 17.39 - 18.45, $^{207}Pb/^{204}Pb$ = 15.49 - 15.61, $^{208}Pb/^{204}Pb$ = 37.06 - 38.05. Enrichment of large-ion lithophile elements within this group is significant (Ba/La = 11 - 130). The BAB-rocks are most likely derived from the same depleted mantle source as the IA-rocks, but underwent higher degrees of melting (8-15 %) and are not influenced by slab components. They have lower abundances of incompatible trace elements, flat REE patterns ($(La/Yb)_n$ = 0.6 - 2.4) and higher initial ϵ_{Nd} values (+7.8 to +8.5). Negative Nb anomalies are absent (Nb/La = 0.81 - 1.30), but Zr/Nb is high (21 - 48).

At least three components are necessary to explain the geochemical evolution of the volcanic rocks: (1) an enriched (ocean-island like) component characterized by a high Nb concentration (up to 30 µg/g), an absent negative Nb anomaly, a low Zr/Nb ratio (~6.5), a low ϵ_{Nd} value (around 0), and radiogenic $^{206}Pb/^{204}Pb$, $^{207}Pb/^{204}Pb$ and $^{208}Pb/^{204}Pb$; (2) a back-arc basin component similar to N-MORB with a flat rare-earth element pattern and a high ϵ_{Nd} value (around +8.5), and (3) an island arc component from a mantle source which was modified by the downgoing slab. Crystal fractionation superimposed on mixing and source contamination by subducted sediments is suitable to explain the observed geochemical data. The most likely geodynamic environment to produce these characteristics is a young, intra-oceanic island arc system and an associated back-arc basin.

3.1 Introduction

Geochemical, petrological and isotopic characteristics of volcanic rocks related to ophiolites are frequently used to reconstruct the geodynamic situation which led to the formation of a specific ophiolite, and to place constraints on the composition of the Earth‘s mantle for a distinct region and time interval (e.g. Zimmer et al. 1995; Swinden et al. 1990; Pedersen and Dunning 1997). Regional mantle sources, source contamination, melting processes, melt migration, and fractionation prior to ophiolite formation are a matter of intensive debate, and some of these processes obscure the primary signature of melts originally formed within the Earth‘s mantle. This is especially the case for island arc related ophiolites, as isotopic and trace element modifications of arc magmas occur within several stages during magma genesis and ascent. Mantle wedge heterogeneities may be an intrinsic feature or can be produced by element transfer from the downgoing slab to the mantle wedge (1) via fluids (Tatsumi 1989; Hawkesworth et al. 1997), (2) via partial melts produced by melting of the downgoing slab (Rapp et al. 1999), (3) via the accretion of unmolten or partially molten subducted sediments to the mantle wedge (Johnson and Plank 1999), or by a combination of these processes. As a consequence of fluid transfer from the slab to the mantle wedge, its solidus will be lowered leading to the formation of primary melts (Tatsumi 1989). Further modifications of these melts will occur on their way to the surface by the reaction with overlying mantle peridotite (Kelemen 1990; Navon and Stolper 1987), and by combined fractional crystallization and assimilation of continental- or pre-existing arc crust (e.g. DePaolo 1981). A detailed knowledge of these processes is thus essential for an understanding of regional mafic and continental crust formation.

Large volumes of continental and oceanic crust were accreted to the Siberian Craton during Neoproterozoic and Palaeozoic times, now represented by the Central Asian Mobile Belt (CAMB or Altaids; Sengör et al. 1993) that extends from the Pacific Ocean to the Ural Mts. (Fig. 1 inset). The origin and evolution of the CAMB is poorly understood and controversially discussed (e.g. Sengör et al. 1993; Sengör and Okurogullari 1991). Basically, the CAMB represents an association of microcontinents, which are interconnected by deformed Neoproterozoic to late Palaeozoic subduction-accretion complexes (Sengör et al. 1993; Kuzmichev et al. 2001). These subduction-accretion complexes developed during the closure of the Palaeoasian Ocean (Belichenko et al. 1994; Melnikov et al. 1994; Khain et al. 1999). The microcontinents are assumed to be Precambrian in age (Berzin et al. 1994; Mitrofanov and Kozakov 1993; Coleman 1989) but their origin is contentious, either they are fragments from Gondwana (Mossakovsky et al. 1993; Didenko et al. 1994), from the Siberian craton (Berzin et al. 1994) or both.

Mafic crustal fragments are widespread within the CAMB where they roughly form E-W trending narrow belts (Avdeyev 1984; Kovalenko et al. 1996a, b; Zonenshain and Kuzmin 1978; Kepezhinskas 1986; Kepezhinskas et al. 1991; Buchan et al. 2001). These belts are usually

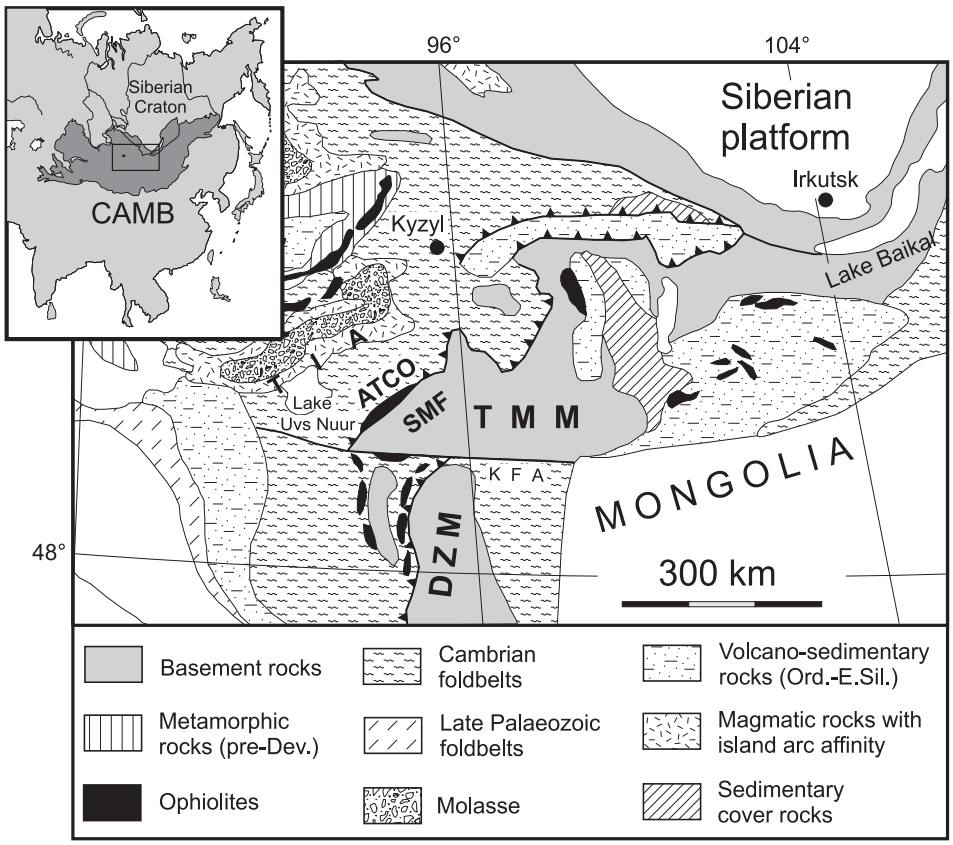

Fig. 1 Central part of the Central Asian Mobile Belt (CAMB), showing main lithotectonic units. ATCO: Agardagh Tes-Chem ophiolite; TMM: Tuva-Mongolian Microcontinent including the Sangilen massif (SMF) adjacent to the ophiolite; TIA: Tannuola island arc; DZM: Dzabkhanian Microcontinent; KFA: Khangay fault. Inset: Geographical overview of Asia with exaggerated area framed (modified from Zonenshain et al. 1990)

regarded as ophiolite zones and thus are interpreted as remnants of the Palaeoasian Ocean (Khain et al. 1997), although their geodynamic origin, i.e. mid-ocean ridge like oceanic crust or island arc related crust, is fairly unknown. However, the ophiolites play an outstanding role in deciphering the evolution of the CAMB because they are lithological markers of former plate boundaries (suture zones).

In this paper we describe the geochemical evolution of the late Neoproterozoic (570 ± 2 Ma; Pfänder et al. 1998) Agardagh Tes-Chem ophiolite (ATCO), situated within the northern part of the CAMB (Fig. 1). This ophiolite is a well-preserved fragment of ultramafic to mafic crust and provides a unique opportunity to study crust-formation processes operating on a large scale. In this context, the ATCO is particularly suitable to reveal the processes which initiated the evolution of the CAMB. We focus on volcanic rocks in which primary geochemical signatures were governed by partial melting, but were modified by crystal fractionation, mixing and contamination processes. We further constrain the geochemical and isotopic composition of the source of these rocks and outline a geodynamic framework suitable to explain the observed geochemical and isotopic data.

3.2 Geological setting

The ATCO marks the northwestern border of the Tuva-Mongolian Microcontinent (TMM) which consists of several intrusive and metamorphic complexes (Kuzmichev et al. 2001; Salnikova et al. 2001; Fig. 1). Adjacent to the SE and S of the ophiolite are the Moren, Erzin and Naryn complexes (Kozakov 1986; Salnikova et al. 2001). The Moren complex consists of metatonalites, gneises, migmatites, amphibolites, marbles, quartzites and minor ultramafic lenses. Kyanite-bearing gneisses indicate HP-metamorphic conditions (Kozakov 1986). The western part of the complex is intruded by early Ordovician diorites and quartz-diorites (Salnikova et al. 2001). The Erzin complex consists of garnet-bearing gneisses, migmatites, granulites and metavolcanic rocks (tholeiites, andesites, dacites). The Naryn complex consists of low-grade metapelites, and of calcareous quartzites. Carbonates are abundant and contain Middle Riphean (~1000 Ma) fossils (Mitrofanov and Kozakov 1993). All complexes belong to the Sangilen massif (Fig. 1), which has traditionally been regarded as Precambrian basement of the TMM, comprising Palaeoproterozoic and Archaean rocks (Ez 1983; Ilyin 1990; Zonenshain et al. 1990). However, recent geochronological studies yielded predominantly early Palaeozoic ages for the metamorphic and intrusive rocks of the Moren, Naryn and Erzin complexes, making the existence of a Precambrian microcontinent questionable (Salnikova et al. 2001). To the north of the ophiolite succession lies the E-W striking Tannuola ridge (Fig. 1), which represents a middle to late Ordovician island arc assemblage (Fedorovskii et al. 1995; Zonenshain et al. 1990; Pfänder et al. 1998).

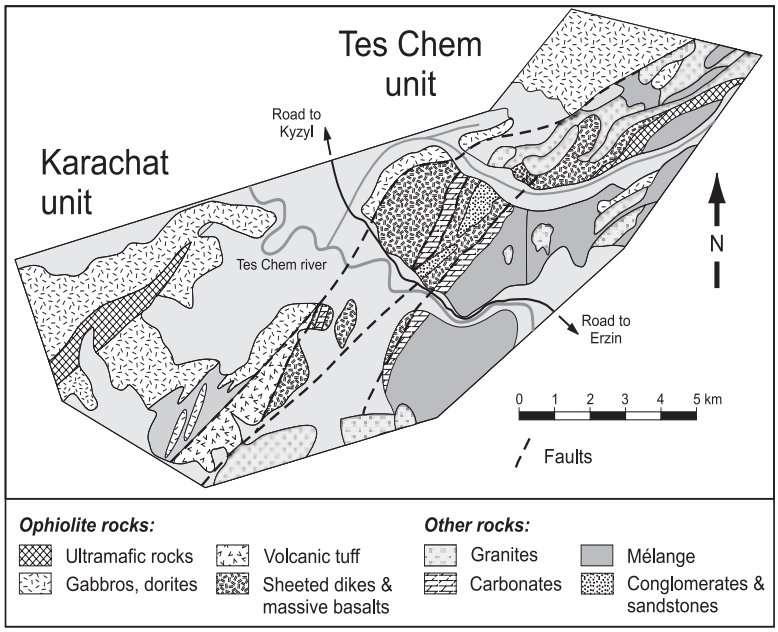

Fig. 2 Geological map of the northeastern part of the Agardagh Tes-Chem ophiolite (ATCO), comprising the Karachat- and Tes-Chem units. The Agardagh unit lies further to the southwest and is not shown

The ATCO can be subdivided into three main units. The southwestern part (Agardagh unit, abbreviated as AD) consists mainly of variably serpentinized ultramafic rocks comprising dunite, harzburgite, wehrlite and pyroxenite. Small lenses of gabbro, gabbronorite and plagiogranite are also present. The AD unit is embedded within a tectonic mélange, consisting of metasedimentary

rocks, carbonates, cherts, sheared pillow lavas and basaltic rocks. The central part of the ATCO (Karachat unit, abbreviated as KA; Fig. 2) represents an intrusive body dominated by gabbros, hornblende-gabbros, gabbronorites and minor diorites. The northeastern part of the ATCO (Tes-Chem unit, abbreviated as TC; Fig. 2) consists of the lower to intermediate part of a sheeted dyke complex, comprising microgabbros, massive basalts and basaltic andesites. Low grade metamorphic pillow lavas occur as sheared bodies within the mélange associated to the TC unit. The samples analyzed in this study are low-grade pillows and massive basalts from the AD unit (samples A22 - A49; Table 1), massive basalts and basaltic dykes/sills from the KA unit (samples A39 - A59; Table 1), and low-grade pillows, massive volcanics and microgabbros from the TC unit (samples T2 - T44; Table 1).

3.3 Results

3.3.1 Major elements

Based on their SiO_2 concentration (Table 1) the volcanic rocks are subdivided into predominantly basalts and basaltic andesites with minor andesites, dacites and picrites. Na_2O and K_2O concentrations (Table 1) are not considered for classification, because alteration probably played a significant role in controlling the budget of alkaline elements within nearly all rocks. All samples except two (A7 & A59) are characterized by calc-alkaline affinity. Mg-numbers (Mg# = molar $Mg/[Mg+Fe^{II}]$) of volcanic rocks range from 0.48 to 0.67 for the TC group rocks, from 0.54 to 0.69 for the KA group rocks and from 0.49 to 0.73 for the AD group rocks (Table 1). Major element correlations for all volcanic rocks are poor or absent (Fig. 3). For the TC and KA group rocks, CaO decreases significantly with decreasing MgO (Fig. 3a), whereas Al_2O_3 slightly increases (Fig. 3b). This indicates that clinopyroxene (cpx) was a dominant phase

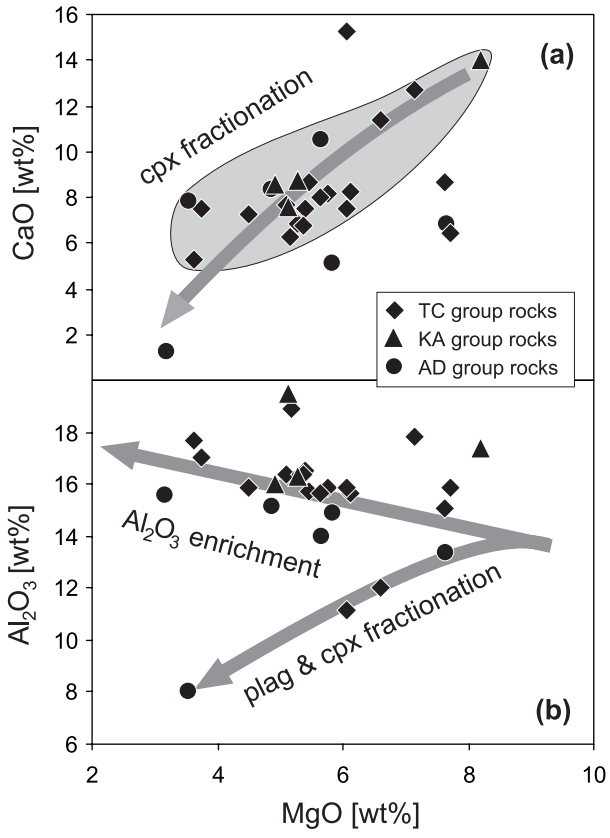

Fig. 3 CaO and Al_2O_3 vs. MgO for all volcanic rocks. (a) Decreasing CaO with decreasing MgO indicates clinopyroxene (cpx) fractionation. (b) Predominantly increasing Al_2O_3 concentrations suggest minor or absent plagioclase (plag) fractionation, except for some low-Al samples

Table 1 Major element (wt%, LOI corrected) and trace element (ppm) composition of volcanic rocks from the Agardagh Tes-Chem ophiolite. FeO* was calculated treating all iron as FeO and assuming that $FeO/(FeO+Fe_2O_3) = 0.85$

	Agardagh unit (AD)							Karachat unit (KA)				
Sample	T97A22	T97A23	T97A24	T97A41	T97A43	T97A47	T97A49	T97A39	T97A40	T97A57	T97A58	T97A59
Rock type	*ba*	*ba*	*da*	*ba (p)*	*ba (p)*	*da*	*an*	*ba*	*ba*	*bs (d)*	*ba (d)*	*pi (d)*
SiO_2	52.59	52.08	69.53	53.47	53.39	64.18	55.08	52.22	52.74	48.73	52.10	42.48
Al_2O_3	14.98	8.65	8.13	15.19	13.42	15.65	14.08	16.02	19.47	16.09	16.31	17.42
Fe_2O_3	14.06	10.11	5.84	9.21	11.84	7.65	9.93	10.47	8.33	10.78	10.80	16.18
MnO	0.18	0.26	0.58	0.13	0.22	0.22	0.14	0.15	0.19	0.18	0.16	0.22
MgO	5.81	11.67	3.53	4.87	7.61	3.18	5.63	4.93	5.12	10.15	5.27	8.18
CaO	5.24	10.94	7.89	8.42	6.92	1.33	10.61	8.60	7.63	10.01	8.75	13.99
Na_2O	4.94	2.42	4.15	4.80	4.62	6.21	2.61	4.28	5.28	2.16	3.31	0.31
K_2O	0.62	0.87	0.32	0.30	0.29	0.97	0.65	1.11	0.22	0.07	0.93	0.05
TiO_2	1.72	2.90	0.35	1.45	1.69	0.78	1.20	1.48	0.90	0.76	1.51	0.60
P_2O_5	0.13	0.37	0.13	0.11	0.13	0.11	0.12	0.54	0.13	0.07	0.50	0.00
Cr_2O_3	0.01	0.02	0.01	0.05	0.00	0.01	0.04	0.01	0.00	0.08	0.01	0.00
NiO	0.00	0.02	0.01	0.01	0.00	0.00	0.02	0.00	0.00	0.02	0.01	0.01
LOI	3.57	3.60	4.09	2.40	2.13	2.36	1.93	1.33	2.71	1.68	2.44	2.58
Total	100.28	100.31	100.48	98.00	100.13	100.29	100.13	99.82	100.01	99.11	99.67	99.44
FeO*	10.75	7.73	4.46	7.04	9.06	5.85	7.60	8.01	6.37	8.25	8.26	12.37
Mg#	0.49	0.73	0.59	0.55	0.60	0.49	0.57	0.52	0.59	0.69	0.53	0.54
Rb	*9*	*9*	*4*	*3*	5.77	*17*	7.68	16.5	*6*	0.389	13.1	0.292
Sr	*129*	*110*	*106*	*82*	223	*139*	261	613	*368*	177	508	114
Ba	*73*	*336*	*103*	*55*	*54*	*185*	*151*	*327*	*81*	*28*	259	*11*
Y	*39*	*23*	*21*	*32*	*43*	*34*	*17*	23.3	*8*	15.6	20.7	2.03
Zr	*95*	*199*	*62*	*90*	*96*	*112*	*58*	128	*23*	36.1	113	0.53
Hf	2.98	5.76	1.88	2.99	2.60		1.79			1.29		
Nb	*3*	*29*	*3*	*4*	*2*	*4*	*5*	9.59	*2*	0.820	11.5	0.039
U	0.137	0.816	0.792	0.090	0.095		0.134	0.470		0.088	0.490	0.004
Th	0.170	2.46	1.45	0.186	0.141		0.395	2.17		0.155	1.41	0.046
Pb	0.880	2.92	4.11	1.43	1.72	*4*	3.31	1.94	*3*	3.22	3.15	0.858
Sc	40	23	17	41	34	22	21	34	18	38	28	61
V	458	238	86	308	405	115	155	246	200	247	241	713
Cr	20	122	111	404	7	51	302	76	25	604	84	9
Co	41	41	28	41	30	15	40	19	30	43	29	61
Ni	26	104	79	89	18	24	187	33	24	179	42	43
Cu	9	1	20	56	25	32	58	25	32	51	81	220
Zn	53	71	56	78	68	91	90	70	77	88	109	76
Ga	20	11	10	14	15	17	18	19	19	15	19	14
La	3.70	26.5	8.54	3.08	3.49		4.79	21.0		2.46	21.2	0.19
Ce	12.2	61.0	30.5	9.06	11.9		11.4	48.6		6.93	46.2	0.29
Pr	1.96	8.13	2.48	1.49	1.98		1.53	6.25		1.04	5.51	0.04
Nd	9.87	29.9	9.26	9.06	12.1		8.09	29.9		5.01	27.4	0.19
Sm	3.62	6.56	2.56	3.26	4.51		3.03	6.63		1.64	6.07	0.11
Eu	1.52	3.46	1.17	0.98	1.31		1.50	2.00		0.63	1.77	0.15
Gd	4.04	8.21	4.30	3.28	4.50		3.01	6.35		2.47	5.51	0.26
Tb								0.91		0.39	0.81	0.06
Dy	4.90	5.31		4.39	6.21		2.65	5.46		2.69	4.71	
Ho	1.13	1.07	0.75	0.96	1.43		0.53	1.07		0.52	0.92	0.09
Er	3.71	2.81	2.35	2.69	3.85		1.44	3.00		1.74	2.52	0.28
Tm								0.37			0.32	
Yb	4.72	2.42	2.95	2.48	3.84		1.41	2.37		1.41	2.05	0.32
Lu								0.34		0.19	0.29	0.03

bs = basalt, ba = basaltic andesite, an = andesite, da = dacite, pi = picrite, mg = microgabbro, p = pillow, d = dike

Rb, Sr, Sm and Nd by TIMS, all other trace elements by MIC-SSMS or ICP-MS (samples A39, A58, T02, T14, T20, T39) except Sc, V, Cr, Co, Ni, Cu, Zn, Ga and italic by XRF

Table 1 (continued)

	Tes-Chem unit (TC)											
Sample	T97T02	T97T03	T97T04	T97T05	T97T06	T97T07	T97T14	T97T15	T97T16	T97T17	T97T18	T97T20
Rock type	*mg*	*ba*	*bs*	*bs*	*ba*	*mg*	*ba*	*an*	*bs*	*ba*	*mg*	*ba*
SiO_2	52.55	53.16	51.21	50.43	52.51	42.59	52.21	56.07	49.12	53.12	55.34	52.15
Al_2O_3	16.34	16.34	12.04	11.13	15.07	17.84	16.49	17.68	19.13	15.88	17.00	15.73
Fe_2O_3	10.01	10.05	11.11	10.08	8.75	18.17	11.15	8.65	11.00	11.24	8.40	10.47
MnO	0.15	0.16	0.16	0.16	0.17	0.23	0.16	0.14	0.18	0.17	0.12	0.18
MgO	5.11	5.27	6.59	6.06	7.63	7.16	5.41	3.63	5.17	4.50	3.74	5.46
CaO	7.70	6.85	11.42	15.22	8.70	12.73	7.49	5.31	6.28	7.27	7.52	8.66
Na_2O	4.06	3.51	4.34	4.42	3.08	0.11	4.38	6.00	5.70	3.64	3.57	3.44
K_2O	1.74	2.44	0.29	0.24	2.82	0.25	1.34	0.88	0.80	1.63	1.57	0.85
TiO_2	1.31	1.31	2.84	2.50	0.76	0.56	0.97	0.80	1.88	1.63	1.16	1.57
P_2O_5	0.64	0.65	0.32	0.29	0.27	0.00	0.36	0.34	0.52	0.77	0.51	0.64
Cr_2O_3	0.02	0.02	0.02	0.02	0.05	0.01	0.01	0.01	0.01	0.01	0.01	0.02
NiO	0.01	0.01	0.01	0.01	0.01	0.00	0.00	0.00	0.00	0.00	0.00	0.01
LOI	1.79	2.95	4.10	6.59	3.51	3.15	7.32	3.93	5.52	1.43	1.73	1.31
Total	99.65	99.78	100.35	100.55	99.80	99.65	99.96	99.52	99.78	99.88	98.93	99.18
FeO*	7.66	7.68	8.50	7.71	6.69	13.90	8.52	6.62	8.41	8.60	6.42	8.01
Mg#	0.54	0.55	0.58	0.58	0.67	0.48	0.53	0.49	0.52	0.48	0.51	0.55
Rb	16.9	*38*	*4*	*3*	*37*	8.29	23.0	11.6	15.7	*22*	27.4	11.4
Sr	604	*547*	*380*	*365*	*648*	117	766	749	1024	*565*	558	744
Ba	450	*634*	*96*	*75*	*364*	*36*	1266	*860*	*345*	*575*	*574*	399
Y	33.5	*30*	*23*	*21*	*17*	1.88	17.4	15.9	24.2	*34*	22.4	25.3
Zr	143	*175*	*168*	*147*	*76*	1.13	76.6	99.0	143	*187*	152	121
Hf								3.81	3.47		4.14	
Nb	12.6	*13*	*26*	*23*	*3*	0.034	11.3	11.3	11.4	*14*	10.9	11.1
U	0.539					0.030	1.53	1.78	1.03		0.735	0.463
Th	2.04					0.011	5.35	5.03	2.71		2.55	1.79
Pb	6.00	*9*	*5*	*3*	*10*	2.71	10.5	27.7	6.31	*9*	6.60	3.44
Sc	26	25	33	30	29	70	29	19	18	28	27	25
V	202	206	301	271	223	782	263	160	199	270	199	221
Cr	116	115	170	136	368	9	79	47	58	33	42	155
Co	32	30	39	36	32	57	30	21	33	29	14	24
Ni	56	63	89	71	80	15	26	17	32	22	21	67
Cu	50	58	112	83	75	195	30	28	49	57	112	28
Zn	101	99	87	74	72	103	92	75	74	104	80	107
Ga	20	19	17	15	16	18	20	19	18	21	19	19
La	31.0			17.5		0.28	30.4	25.1	23.0		23.3	22.9
Ce	59.9			41.1		0.43	56.2	52.5	50.3		48.8	46.2
Pr	9.54					0.06	7.18	7.29	7.26		7.10	7.57
Nd	36.1			23.5		0.25	29.1	31.0	32.7		30.4	35.8
Sm	7.37			6.79		0.13	5.96	6.30	6.74		6.27	7.13
Eu	2.26			1.56		0.17	2.15	1.86	1.94		2.07	2.11
Gd	7.08			5.75		0.25	5.68					6.50
Tb	0.99						0.69	0.74	0.85		1.02	0.88
Dy	6.13			4.97			3.98					5.34
Ho	1.23					0.08	0.71	0.64	0.90		0.95	1.03
Er	2.95			2.55		0.28	1.79	1.53	2.53		2.58	2.56
Tm	0.45						0.24					0.36
Yb	3.16			1.64		0.33	1.49	1.74	2.57		3.08	2.53
Lu	0.37			0.17		0.03	0.18	0.25	0.36		0.38	0.30

Table 1 (continued)

	Tes-Chem unit (TC)						
Sample	T97T31	T97T39	T97T40	T97T41	T97T42	T97T43	T97T44
Rock type	*ba*	*bs*	*bs*	*bs*	*bs*	*bs*	*bs*
SiO_2	53.09	51.19	49.97	50.32	50.27	50.98	48.78
Al_2O_3	16.39	15.84	15.62	15.65	15.66	15.83	15.87
Fe_2O_3	11.23	11.90	12.50	12.00	12.04	12.01	12.44
MnO	0.17	0.17	0.19	0.18	0.19	0.19	0.22
MgO	5.37	5.75	5.64	5.63	6.11	6.05	7.71
CaO	6.80	8.13	7.98	8.03	8.24	7.53	6.43
Na_2O	3.68	3.28	3.30	3.35	3.06	3.26	3.78
K_2O	1.65	1.03	1.00	1.16	1.30	1.17	1.22
TiO_2	1.24	1.76	1.92	1.83	1.76	1.74	1.96
P_2O_5	0.45	0.75	0.78	0.77	0.73	0.75	0.77
Cr_2O_3	0.02	0.02	0.02	0.02	0.02	0.02	0.02
NiO	0.00	0.01	0.01	0.01	0.01	0.01	0.01
LOI	4.84	1.93	3.08	2.31	2.99	2.21	2.77
Total	100.09	99.84	98.91	98.94	99.40	99.54	99.20
FeO*	8.59	9.10	9.56	9.18	9.21	9.18	9.51
Mg#	0.53	0.53	0.51	0.52	0.54	0.54	0.59
Rb	*23*	17.7	*18*	*21*	21.9	*21*	14.4
Sr	*1413*	704	*721*	*724*	652	*668*	635
Ba	*1036*	356	*357*	*477*	*379*	*355*	*611*
Y	*20*	31.9	*34*	*34*	34.8	*34*	36.5
Zr	*147*	146	*174*	*176*	144	*172*	151
Hf					3.57		3.83
Nb	*14*	13.5	*13*	*13*	13.3	*13*	12.9
U		0.434			0.377		0.449
Th		1.45			1.27		1.13
Pb	*19*	3.24	*6*	*5*	5.64	*5*	6.32
Sc	33	28	28	29	30	26	29
V	272	249	270	255	256	251	278
Cr	140	140	138	131	165	159	130
Co	32	33	36	33	35	36	38
Ni	38	57	52	49	79	62	52
Cu	58	62	51	33	38	48	48
Zn	103	103	115	123	128	125	113
Ga	22	21	21	19	19	19	19
La		27.8			21.1		23.3
Ce		68.7			44.9		55.1
Pr		9.12			7.44		8.41
Nd		36.4			35.2		37.9
Sm		7.82			7.62		8.28
Eu		2.72			1.88		2.22
Gd							
Tb		1.04			0.87		1.06
Dy		5.88			6.95		6.92
Ho		1.17			0.98		1.07
Er		3.20			2.68		2.96
Tm		0.48					
Yb		3.00			2.80		3.31
Lu		0.46			0.37		0.42

during fractionation of KA and TC group parental melts. A large scatter in terms of major element compositions for the AD group volcanic rocks suggests a non-uniform origin of these samples. TiO_2 decreases with decreasing MgO for all samples (Fig. 4), but TiO_2 concentrations are generally high (0.5 - 2.9 %, Table 1) and higher than in primitive ocean floor basalts (~ 0.6 - 1 %; Presnall and Hoover 1987) or in many island arc basalts. The latter usually have TiO_2 < 1 % (e.g. Woodhead et al. 1998) due to Ti retention in residual slab minerals (rutile, titanite; Brenan et al. 1994). In contrast, oceanic-island basalts (OIB) tend to have higher TiO_2 (> 2 % TiO_2; e.g. Garcia et al. 1998). In terms of TiO_2 concentration most of the volcanic rocks are very similar to back-arc basin basalts (TiO_2 ~0.7 - 2 %; Eissen et al. 1991; Hawkins 1976; Hawkins et al. 1985; Pearce et al. 1995) and mid-ocean ridge basalts (MORB average TiO_2 = 1.6 %; Hofmann 1988).

3.3.2 Trace elements

3.3.2.1 Compatible trace elements

Cr and Ni concentrations (Table 1, Fig. 5a) in most of the volcanic rocks are low compared to primary basalts (Ni = 300 - 400 µg/g, Cr = 300 - 500 µg/g; Hess 1992; Frey et al. 1978). The concentrations of both elements are well correlated for most of the TC and KA group rocks (except A57, T6 & T7; Fig. 5a), suggesting a common parental magma and substantial cpx and/or combined olivine and spinel fractionation. A few samples are characterized by relatively high Mg# (0.67-0.73; MgO up to 11.7 wt%) and high Ni and Cr concentrations (up to 187 and 604 µg/g, respectively, Fig. 5b). These samples may represent less fractionated primary melts. On the other hand, due to the generally large scatter, it is unlikely that all volcanic rocks were derived from one single parental melt by simple fractionation processes.

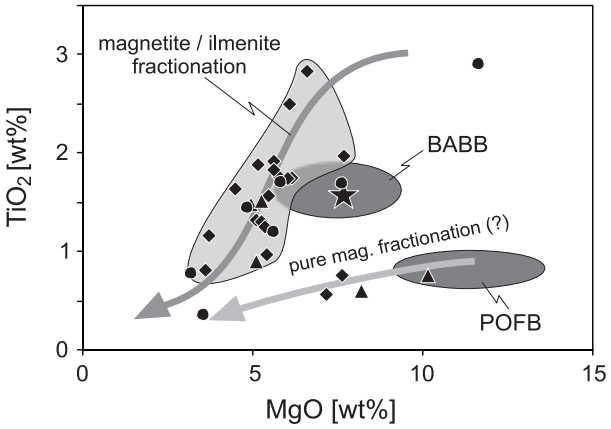

Fig. 4 TiO_2 vs. MgO. Decreasing TiO_2 with decreasing MgO indicates magnetite and/or ilmenite fractionation.TiO_2 concentrations for most of the samples are higher than in primitive ocean floor basalts (POFB; Presnall & Hoover 1987) but resemble back-arc basin basalts (BABB; Eissen et al. 1995), although the variation is significantly larger (symbols as in Fig. 3). Star: average MORB (Hofmann 1988)

3.3.2.2 Incompatible trace elements

Primitive mantle (PRIMA; Hofmann 1988) normalized trace element concentrations of selected samples from all three units are shown in Fig. 6. All TC group samples (Fig. 6a) are characterized by negative Nb anomalies with relatively uniform Nb/La ratios (Nb/La = 0.37 - 0.62, except T7:

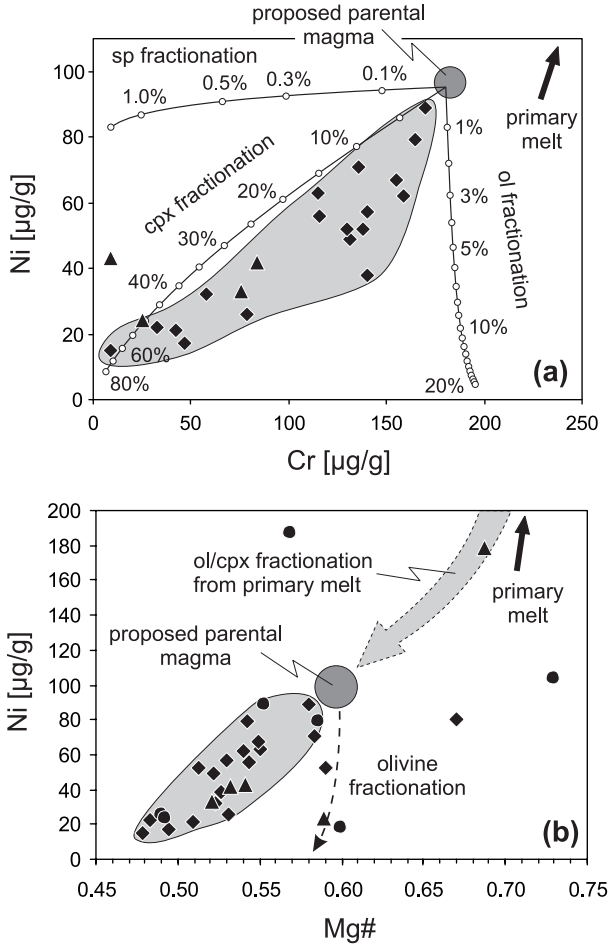

Fig. 5 (a) Ni vs. Cr in TC and KA group volcanic rocks (rhombs: TC group, triangles: KA group). Ni and Cr are well correlated indicating either substantial clinopyroxene fractionation or combined olivine and spinel fractionation (Rayleigh fractionation, partition coefficients from Bédard 1994; numbers give amount of phase fractionated). (b) Ni vs. Mg# of all volcanic rocks, including AD group rocks (circles). The proposed composition of the parental magma is: Mg# ~ 0.60, Ni ~ 95 µg/g, Cr ~ 180 µg/g

0.12). Nb/U ratios are more variable (6.4 - 35), indicating variable enrichment of U relative to N-MORB (Nb/U = 49; data for N-MORB from Hofmann 1988). Pb anomalies are also variable (Ce/Pb = 1.9 - 21, except T7: 0.2), but are overall positive compared to N-MORB (Ce/Pb = 25). Th/U ratios within this group vary between 2.5 and 3.9 with an average of 3.3 ± 0.5 (1σ). Sample T7 is also characterized by a negative Nb and a positive Pb anomaly, but displays a significant depletion in incompatible trace elements relative to primitive mantle and N-MORB. All TC samples are characterized by slightly positive Sr and negative Ti anomalies. KA group samples (Fig. 6b) have also negative Nb anomalies (Nb/La = 0.20 - 0.54; Nb/U = 9.1 - 23), but span a wider range in trace element concentrations than TC group rocks. However, the most enriched KA samples resemble the TC group rocks and thus most likely represent the same source and underwent more or less the same post-melting evolution. Lead anomalies are similar to the TC suite rocks (Ce/Pb = 2.2 - 25, except A59: 0.4). However, Th/U ratios are more variable than in TC group samples (Th/U = 1.8 - 10.5). AD group rocks (Fig. 6c) are heterogeneous compared to KA and TC group rocks, with one sample (A23) having an oceanic island-like („OIB-like“) trace element pattern (Fig. 6c). This sample is characterized by enrichment of Nb (Nb/La = 1.1; Nb/U = 37) and depletion of Pb (Ce/Pb = 21). Two AD group rocks are metapillows which are very similar in trace element composition to N-MORB (Fig. 6d). Th/U ratios within all AD group rocks vary between 1.2 and 3.0 with an average of 2.1 ± 0.7 (1σ) and thus are significantly lower than in TC group rocks.

Zr/Nb ratios of volcanic rocks from all three units vary between 6.4 and 48 and correlate with Nb concentrations (Fig. 11). Ba/La ratios differ not significantly between different units (average value for TC ~23, for KA ~25, for AD ~19), but are higher than in primitive mantle (Ba/La = 10) and

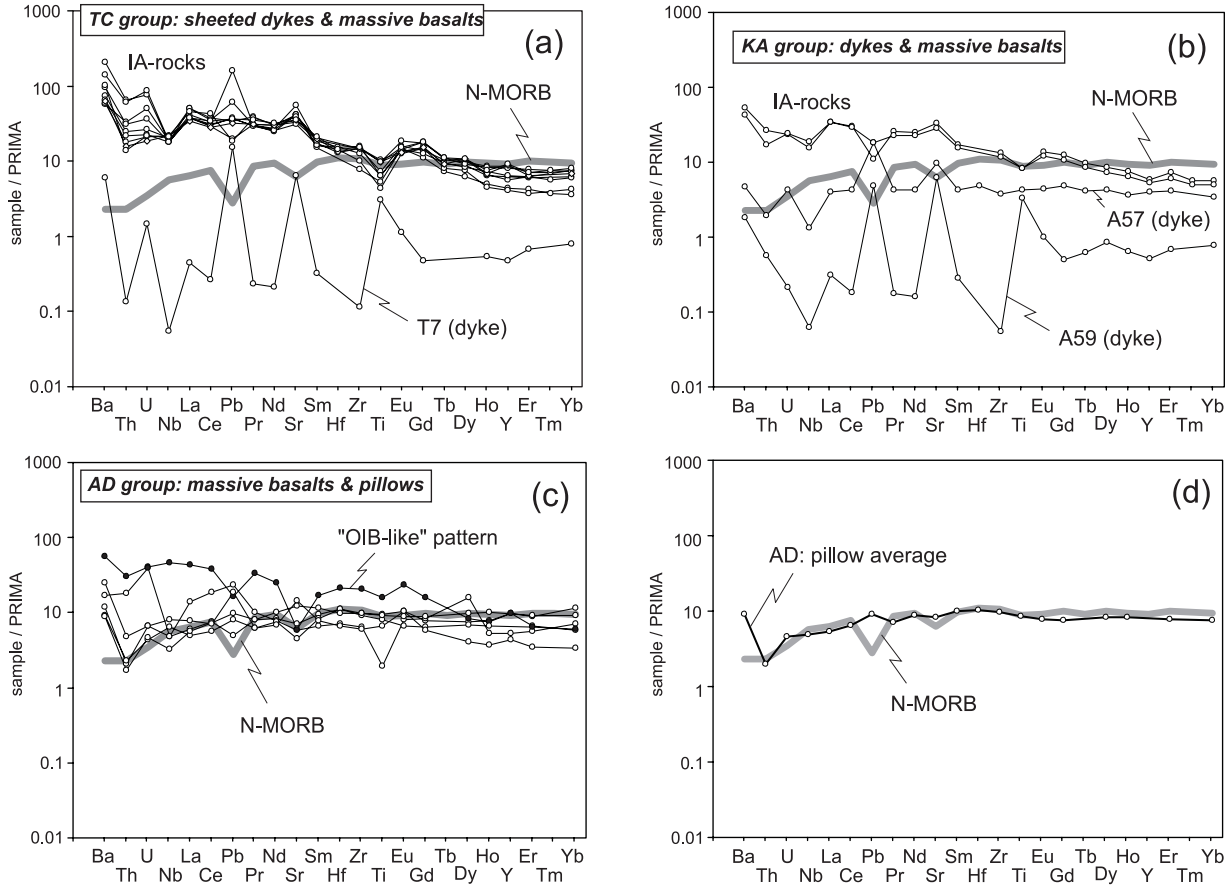

Fig. 6 Concentrations of incompatible trace elements for selected samples, normalized to primitive mantle values (Hofmann 1988). (a) TC group rocks have negative Nb anomalies and are strongly enriched in highly incompatible trace elements relative to N-MORB (except T7). Pb anomalies are variable. (b) KA group rocks have negative Nb and Pb anomalies. One sample is more depleted with a positive Pb anomaly. Sample A59 represents a dyke and strongly resembles sample T7 of the TC group. (c) AD group rocks are heterogeneous with one sample having an „OIB-like“ pattern (absent negative Nb anomaly, negative Pb anomaly). (d) Average of two AD group metapillows (note the similarity to N-MORB). Generally, TC and KA group volcanic rocks are very similar, but different to AD group volcanic rocks. Samples T7 and A59, and probably A57, are dykes and are characterized by completely different trace element characteristics. Grey curves: N-MORB for comparison, data from Hofmann (1988)

N-MORB (Ba/La = 3.6). This indicates an enrichment of large-ion lithophile elements (LILE) within all rocks. Zr/Hf ratios vary between 26 and 41 with an average of 34 ± 5 (N-MORB = 35; PRIMA = 36). Ti/V ratios for all rocks are between 19 and 57 (except A23, A59 and T7) and thus are rather in the range of back-arc basin (BAB) basalts or MORB (typically between 20 and 50) than within the range of many island arc basalts (typically <20; Shervais 1982).

3.3.2.3 Rare earth elements

Based on their chondrite-normalized rare-earth element (REE) abundances (Fig. 7), the volcanic rocks are subdivided into three groups. All TC group samples (except T7; Fig. 7a) and two KA volcanic rocks (Fig. 7b) show a significant enrichment in light-(L)REE relative to chondrite

and heavy-(H)REE. Chondrite-normalized $(La/Yb)_n$ ratios for this group are between 14.6 and 5.1, whereas $(Sm/Nd)_n$ is nearly constant (0.61 - 0.67). Eu-anomalies are negligible or absent. Based on the REE budget, this group of rocks is very similar to unusually enriched island arc basaltic rocks from the Lesser Antilles Islands (Fig. 7a, b). These rocks are low-Mg calcic basalts generated from picritic parental melts by high-level fractionation of plagioclase, augite, olivine, and titano-magnetite (Thirlwall and Graham 1984). In the following we refer to the LREE enriched group as island arc related rocks (IA-rocks).

The second group comprising all AD volcanic rocks is characterized by flat REE patterns (Fig. 7c; except the „OIB-like“ sample A23) with $(La/Yb)_n$ = 0.6 - 2.4, $(La/Sm)_n$ = 0.5 - 1.0 and $(Sm/Nd)_n$ = 0.8 and 1.1. Eu-anomalies are absent or slightly positive. Although the general pattern within this group is the same, absolute abundances vary significantly by a factor of about 2 for the LREE and of about 4 for the HREE. Despite the variability in absolute REE abundances and non-parallel REE patterns, we refer to this group as back-arc basin related samples in the following (BAB-rocks). The assumption of a back-arc or even open-basin origin of at least some of these samples is justified by trace element data (Fig. 6d, 7c) but also by field relationships and isotopic results discussed below. Nevertheless, we emphasize that the BAB-rocks may even represent fragments of „true“ mid-ocean ridge (MOR) related mafic rocks as the transition from back-arc to open-marine is difficult to constrain geochemically.

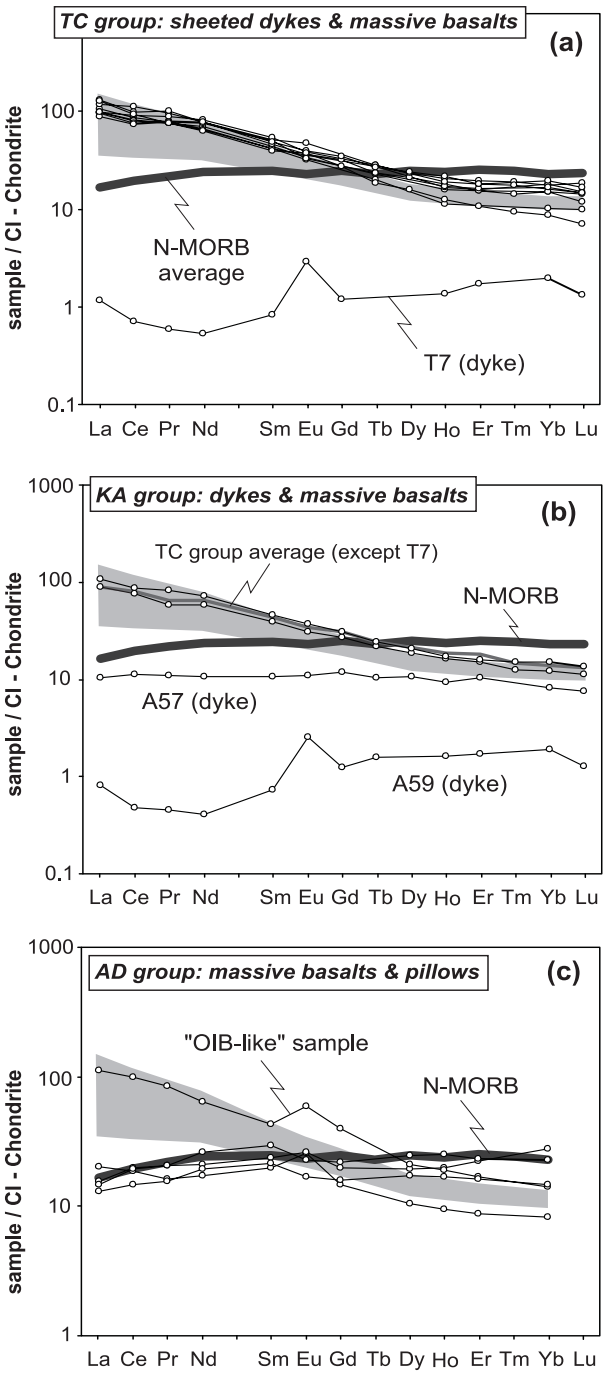

Fig. 7 Chondrite-normalized REE composition of volcanic rocks. (a) TC group rocks are strongly enriched in LREE compared to N-MORB, but depleted in HREE (except strongly depleted dyke sample T7). (b) KA group rocks split into enriched massive basalts, identical to TC group rocks, and one flat and one LREE depleted dyke sample. (c) AD group rocks are more heterogeneous but tend to have flat REE patterns similar to MORB, except one sample termed "OIB - like". Shaded field: enriched basaltic rocks from the Lesser Antilles island arc (data from Thirlwall & Graham 1984; normalizing values from Sun & McDonough 1989)

The third group is represented by only two samples (dykes T7 and A59; Fig. 7a, b) and is characterized by a depleted but U-shaped LREE pattern with $(La/Yb)_n$ = 0.4 and 0.6, $(La/Sm)_n$ = 1.1 and 1.4, and $(Sm/Nd)_n$ = 1.5 and 1.8. Positive Eu-anomalies as well as La and Ce enrichments are due to the presence of feldspar phenocrysts.

3.3.3 Isotopic data

Sr and Nd whole rock isotopic compositions and Sr, Rb, Nd and Sm concentrations of selected samples are listed in Table 2. Initial $^{87}Sr/^{86}Sr$ ratios (calculated for an age of 570 Ma) vary between 0.70294 and 0.70590. In terms of their initial $^{87}Sr/^{86}Sr$ ratios vs. ϵ_{Nd} (570 Ma) (not shown) the volcanic rocks and dykes plot right to the recent mantle array and slightly below the MORB field for 570 Ma. Some initial $^{87}Sr/^{86}Sr$ ratios are shifted to higher values for a given ϵ_{Nd} (570) due to seawater alteration ($^{87}Sr/^{86}Sr$ in seawater ~570 Ma ago was between about 0.7065 and 0.7075; Jacobsen and Kaufman 1999). Therefore, Sr isotopic ratios are not further considered since they probably indicate more or less intensive sea floor alteration and rock-water exchange.

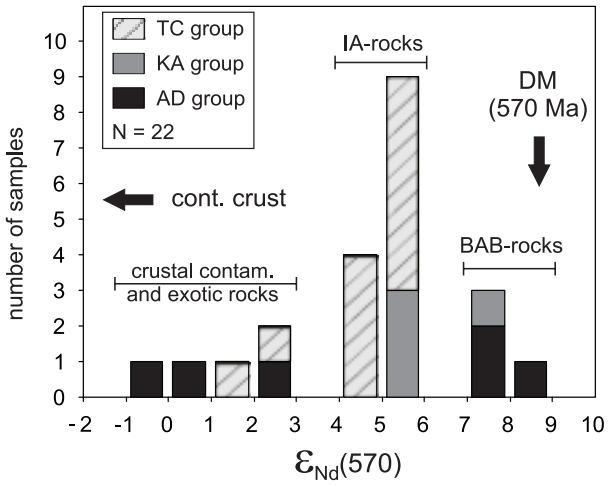

Fig. 8 Distribution of initial ϵ_{Nd} values for samples from all three units. AD group rocks have the largest range from -1 up to +9 and include highly depleted BAB-rocks (metapillows) and enriched fragments associated with the mélange. TC and KA group rocks are more uniform with a maximum of around +5.5. Although KA volcanic rocks tend to be more radiogenic than TC group rocks, both groups mainly represent IA-rocks. DM gives the depleted mantle value 570 Ma ago, old continental crust plots outside the given range

Initial ϵ_{Nd} values (570 Ma) of samples from all three units are given in Table 2 and shown in Fig. 8. The values span a large range from -0.6 for the least radiogenic sample (A24) to +8.5 for the most radiogenic sample (A22), with the latter value being close to the 570 Ma depleted mantle value of +8.75 (linear evolution model after Goldstein et al. 1984). Both samples belong to the AD section, whereas the KA and TC group rocks are more uniform in their Nd isotopic composition ($\epsilon_{Nd}(570)$ = +5.5 to +7.7 and +1.9 to +5.9, respectively), in which the majority of samples have initial ϵ_{Nd} values around +5.5.

Based on the classification in IA- and BAB-rocks, the IA-rocks have intermediate, but variable initial ϵ_{Nd} values between +1.9 and +6.0 (average = +4.6), whereas the BAB-rocks have higher initial ϵ_{Nd} values between +7.7 and +8.5 (average = +8.0). The U-shaped, REE depleted samples (dykes T7 & A59) have intermediate initial ϵ_{Nd} values of +5.1 and +5.5 suggesting that these two samples were derived from the same source as the IA-rocks. However, the most unradiogenic

Table 2 Rb-Sr and Sm-Nd data of volcanic rocks from the Agardagh Tes-Chem ophiolite

	Rb (ppm)	Sr (ppm)	$^{87}Rb/^{86}Sr$	$(^{87}Sr/^{86}Sr)_m$ [1)]	$(^{87}Sr/^{86}Sr)_i$ [2)]	Sm (ppm)	Nd (ppm)	$^{147}Sm/^{144}Nd$	$(^{143}Nd/^{144}Nd)_m$ [1)]	$(^{143}Nd/^{144}Nd)_i$ [2)]	$(\varepsilon_{Nd})_{570}$
Agardagh unit (AD)											
T97A22						3.62	9.87	0.2219	0.513168 ± 8	0.512340	8.5
T97A23						6.56	29.9	0.1328	0.512522 ± 10	0.512027	2.4
T97A24						2.56	9.26	0.1668	0.512498 ± 7	0.511876	-0.6
T97A41						3.26	9.06	0.2173	0.513114 ± 8	0.512303	7.8
T97A43	5.77	222.9	0.0749	0.705898 ± 12	0.705290	4.51	12.1	0.2245	0.513147 ± 11	0.512309	7.9
T97A49	7.68	260.5	0.0853	0.705791 ± 13	0.705098	3.03	8.09	0.2263	0.512753 ± 8	0.511909	0.1
Karachat unit (KA)											
T97A39	16.5	612.9	0.0778	0.704487 ± 11	0.703855	6.63	29.9	0.1339	0.512710 ± 13	0.512211	6.0
T97A57	0.389	177.5	0.0063	0.703311 ± 11	0.703260	1.64	5.01	0.1975	0.513035 ± 12	0.512298	7.7
T97A58	13.1	507.8	0.0745	0.704409 ± 8	0.703804	6.07	27.4	0.1340	0.512661 ± 12	0.512161	5.0
T97A59	0.292	114.1	0.0074	0.703460 ± 10	0.703400	0.11	0.19	0.3561	0.513517 ± 13	0.512187	5.5
Tes-Chem unit (TC)											
T97T02	16.9	603.6	0.0810	0.704620 ± 14	0.703963	7.37	36.1	0.1232	0.512657 ± 5	0.512198	5.7
T97T04						5.99	26.2	0.1381	0.512651 ± 5	0.512136	4.5
T97T05						5.21	23.1	0.1365	0.512652 ± 5	0.512143	4.7
T97T07	8.29	117.3	0.2045	0.704600 ± 12	0.702938	0.126	0.250	0.3038	0.513298 ± 12	0.512163	5.1
T97T14	23.0	766.0	0.0867	0.705774 ± 18	0.705070	5.96	29.1	0.1238	0.512482 ± 6	0.512020	2.3
T97T15	11.6	748.9	0.0446	0.705485 ± 10	0.705123	6.30	31.0	0.1231	0.512461 ± 5	0.512001	1.9
T97T16	15.7	1024	0.0442	0.704831 ± 12	0.704472	6.74	32.7	0.1245	0.512626 ± 13	0.512162	5.0
T97T18	27.4	558.2	0.1422	0.704732 ± 7	0.703577	6.27	30.4	0.1248	0.512651 ± 15	0.512185	5.5
T97T20	11.4	744.0	0.0442	0.704503 ± 13	0.704144	7.13	35.8	0.1205	0.512656 ± 3	0.512207	5.9
T97T39	17.7	703.9	0.0729	0.704489 ± 15	0.703897	7.82	36.4	0.1301	0.512607 ± 5	0.512122	4.3
T97T42	21.9	652.5	0.0971	0.704603 ± 8	0.703815	7.62	35.2	0.1309	0.512655 ± 9	0.512166	5.1
T97T44	14.4	635.2	0.0653	0.704534 ± 14	0.704003	8.28	37.9	0.1321	0.512645 ± 16	0.512153	4.9

[1)] measured values, error: in run precision from individual ratios ($2\sigma_m$), given are the last digits of the reported value. [2)] initial values calculated for an age of 570 Ma

Table 3 Pb isotopic data of volcanic rocks from the Agardagh Tes-Chem ophiolite

	Measured values				Corrected to 570 Ma[1)]		
	$^{208}Pb/^{204}Pb$	$^{207}Pb/^{204}Pb$	$^{206}Pb/^{204}Pb$	$^{207}Pb/^{206}Pb$	$^{208}Pb/^{204}Pb$	$^{207}Pb/^{204}Pb$	$^{206}Pb/^{204}Pb$
Agardagh unit (AD)							
T97A22	38.28	15.60	19.11	0.8162	37.91	15.54	18.19
T97A23	40.37	15.80	20.83	0.7586	38.69	15.70	19.09
T97A24	39.61	15.85	21.53	0.7365	38.91	15.78	20.33
T97A41	38.34	15.55	19.41	0.8010	38.09	15.53	19.04
T97A43	38.33	15.66	19.00	0.8242	38.18	15.64	18.68
T97A49	37.57	15.56	17.42	0.8932	37.35	15.55	17.19
Karachat unit (KA)							
T97A39	38.34	15.57	18.82	0.8276	36.24	15.49	17.39
T97A57	37.67	15.51	18.06	0.8588	37.59	15.50	17.90
T97A58	38.24	15.59	18.43	0.8462	37.40	15.54	17.52
T97A59	37.62	15.54	17.83	0.8717	37.52	15.54	17.80
Tes-Chem unit (TC)							
T97T02	37.97	15.53	18.21	0.8529	37.34	15.50	17.69
T97T05	40.35	15.70	20.68	0.7589			
T97T07	37.55	15.52	17.77	0.8735	37.54	15.52	17.70
T97T14	38.13	15.61	18.31	0.8524	37.18	15.56	17.46
T97T15	38.15	15.61	18.36	0.8502	37.81	15.59	17.99
T97T16	39.13	15.60	19.43	0.8028	38.30	15.54	18.46
T97T18	38.58	15.58	18.84	0.8271	37.85	15.54	18.18
T97T20	38.03	15.55	18.27	0.8514	37.06	15.50	17.48
T97T39	38.09	15.54	18.36	0.8464	37.25	15.50	17.58
T97T42	37.97	15.53	18.26	0.8502	37.55	15.51	17.88
T97T44	38.22	15.54	18.69	0.8318	37.88	15.52	18.27
Pb triple spike duplicates							
T97T02	37.9848 ± 0.0051	15.5364 ± 0.0016	18.1921 ± 0.0013	0.854019 ± 0.000028	37.355	15.506	17.671
T97T15	38.3919 ± 0.0043	15.6365 ± 0.0013	18.5137 ± 0.0011	0.844606 ± 0.000024	38.052	15.614	18.138
T97T16	38.4088 ± 0.0035	15.5978 ± 0.0011	18.7532 ± 0.0010	0.831741 ± 0.000018	37.601	15.541	17.795
T97T44	38.0478 ± 0.0054	15.5507 ± 0.0017	18.2842 ± 0.0014	0.850504 ± 0.000030	37.714	15.526	17.871

The error of the triple spike analyses is given as two sigma of the mean ($2\sigma_m$) and was computed from the in run precisions of the spiked and unspiked run of each sample. The error for all other ratios is $\pm 10^{-3}$

[1)] Corrected for in situ decay of Th and U using high precision Th, U and Pb concentrations determined by isotope dilution MIC-SSMS

samples (initial ϵ_{Nd} values between -0.6 and +2.4) have both flat and enriched REE patterns, ruling out a simple genetic relationship. Generally, the large variation of initial ϵ_{Nd} and the absent linear correlation in terms of $^{143}Nd/^{144}Nd$ vs. $^{147}Sm/^{144}Nd$ within and in between the different units rules out a comagmatic evolution.

Measured and age-corrected Pb isotopic compositions of samples from all three units are given in Table 3 and shown in Fig. 9. Age correction to 570 Ma was done using high precision Th, U and Pb concentrations determined by isotope dilution MIC-SSMS. The TC and KA group rocks have age-corrected $^{207}Pb/^{204}Pb$ and $^{206}Pb/^{204}Pb$ ratios of 15.49 to 15.61 and 17.39 to 18.46, respectively. In contrast, the AD group rocks display a wider range in age-corrected $^{207}Pb/^{204}Pb$ and $^{206}Pb/^{204}Pb$ of 15.53 to15.78 and 17.19 to 20.33, respectively (Fig. 9a). This is consistent with the wider range in initial ϵ_{Nd} values for this group. Considering measured $^{208}Pb/^{204}Pb$ vs. $^{206}Pb/^{204}Pb$ ratios, the TC and KA group rocks (i.e. IA-rocks) are well correlated (Fig. 9b), whereas the AD group rocks (comprising the BAB-rocks) plot to the right of this array.

3.4 Discussion

3.4.1 Parental magma(s) and fractional crystallization

Low abundances of Cr and Ni and moderately to low Mg# in most of the volcanic rocks, particularly the TC and KA group samples (i.e. IA-rocks, Fig. 5), necessitates substantial fractionation to produce the parental magma of these rocks from a primary melt. Using the Mg# and Cr and Ni concentrations, we infer the composition of the parental magma to have been as follows: Mg# ≥ 0.60, Cr ≥ 180 µg/g and Ni ≥ 95 µg/g (Fig. 5). Decreasing the Cr and Ni concentration of a mantle derived, primary melt (~500 µg/g Cr and ~400 µg/g Ni, respectively; Frey et al. 1978) to these values requires fractionation of about 12 % solid phase with a composition of 95 % olivine and 5 % spinel (assuming Rayleigh fractionation, partition coefficients from Bédard 1994 and Conrad and Kay 1984). This amount seems reasonable with respect to the Mg# of the infered parental magma (e.g. fractionation of about 15 % olivine with an average Fo = 0.81 reduces the Mg# of a melt from 0.70 to 0.61). Therefore fractionation of olivine and spinel from a primary melt could produce the parental magma, from which the TC and KA group rocks further developed. The assumption of solely olivine crystallization is justified since primary melts have only olivine on their liquidus at moderate to low pressures (Hess 1992). As demonstrated by Heath et al. (1998) by investigating calc-alkaline

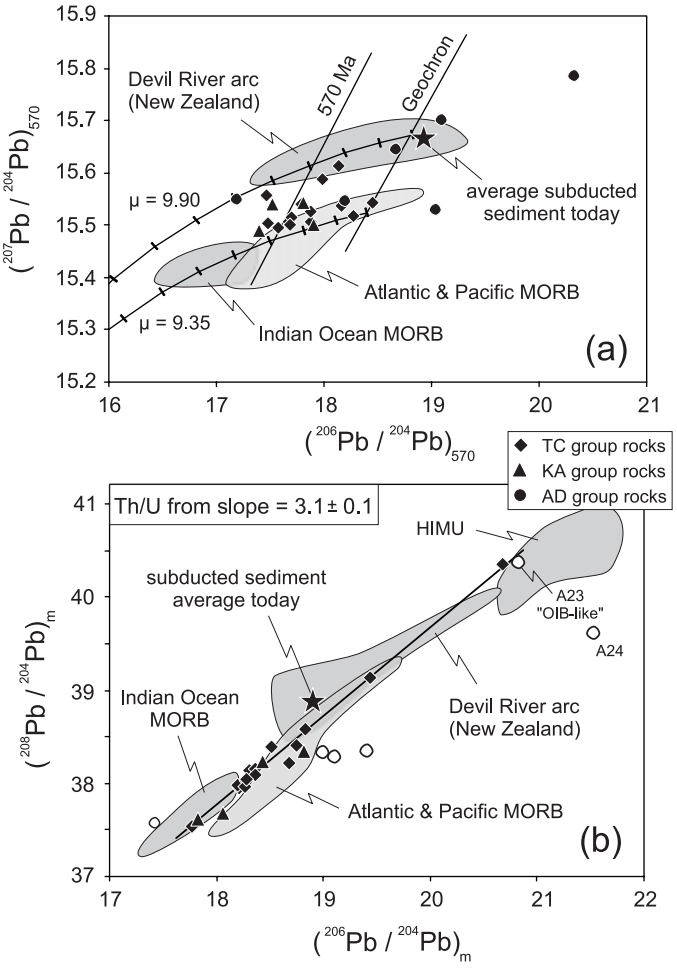

Fig. 9 Pb isotopic composition of volcanic rocks from all three units. (a) age corrected $^{207}Pb/^{204}Pb$ vs. $^{206}Pb/^{204}Pb$ ratios plot between two Pb evolution lines with μ = 9.35 and μ = 9.90, respectively (tick distance is 200 Ma, details see text). Also shown are the geochron and the 570 Ma primary isochron. Data for Atlantic, Pacific and Indian ocean MORB are from Ito et al. (1987) and are recalculated to 570 Ma using μ = 8.92. Also shown are age corrected data from the slightly younger (500 Ma) Devil River arc system in New Zealand (Münker 2000), which is an intra-oceanic arc back-arc system. (b) Measured $^{208}Pb/^{204}Pb$ vs. $^{206}Pb/^{204}Pb$ is linearly correlated for the IA-rocks (filled symbols) with the slope giving a time integrated Th/U ratio for the source of 3.1. The BAB-rocks (open circles) are scattered, but more radiogenic in $^{206}Pb/^{204}Pb$ indicating a slightly lower Th/U ratio of their source. HIMU data from Chauvel et al. (1992), sediment data from Plank and Langmuir (1998)

series from the Lesser Antilles, the assumption of olivine and Cr-spinel as liquidus phases is also valid for primary melts related to arc environments.

Proceeding from the evolved composition of the infered parental magma, fractionation of ~60 % cpx or ~1 % spinel and ~15 % olivine is required to fit the observed range in Mg#, Cr and Ni within the volcanic rocks themselves (Fig. 5). Due to the occurrence of cpx phenocrysts, the absence of olivine phenocrysts, the decreasing CaO with decreasing MgO (Fig. 3a) and the elevated SiO_2 concentration and the quartz normative character of most of the volcanic rocks, we prefer the assumption of predominantly cpx fractionation from the parental magma. Increasing Al_2O_3 with decreasing MgO (Fig. 3b) further indicates that plagioclase was not a dominant liquidus phase during the fractionation of the volcanic series. This is underlined by lacking negative Sr and Eu anomalies within most samples from all three units (Fig. 6 & 7). Negative Ti anomalies (Fig. 6) and decreasing TiO_2 with decreasing MgO (Fig. 4) show that magnetite/ilmenite fractionation played a role during the evolution of the volcanic rocks.

Table 4 Source and melt modes used for melting calculations

Source modes					Melt modes					Source and Ref.
Ol	Opx	Cpx	Sp	Gt	Ol	Opx	Cpx	Sp	Gt	
57	25	16	2	0	-7	25	80	2	0	spinel lherzolite[1)] (cpx out after 20% melting)
60	20	10	0	10	4	-19	105	0	10	garnet peridotite[2)] (cpx out after 10% melting)
83	15	0	2	0	35	63	0	2	0	harzburgite[3)] (opx out after 24% melting)

[1)] Woodhead et al. (1993); [2)] Johnson (1998); [3)] Kelemen et al. (1990)

3.4.2 Degree of melting

Estimating the degree of melting implies several problems due to variable enrichment effects of the magma source caused by subduction-related processes. It is well known that the budget of hydrophile elements (Rb, K, Sr, Ba, U, Pb) in the mantle wedge is controlled by fluids released from the dehydrating slab (Peacock 1993; Ryan et al. 1996; Regelous et al. 1997; Johnson and Plank 1999). On the other hand, the inventory of more immobile, incompatible elements (e.g. Th) may be controlled by melts formed from the slab itself (Peacock et al. 1994) or from subducted sediments, or from sediments directly accreted to the mantle wedge (Hawkesworth et al. 1997; Johnson and Plank 1999). Although all IA-rocks display significant negative Nb anomalies (Fig. 6a, b), absolute abundances of Nb are about a factor of three higher than in BAB-rocks (predominantly AD group rocks) and in N-MORB (Fig. 10). Therefore, the negative Nb anomalies rather indicate an enrichment of LILE relative to Nb and other high-field strength elements (HFSE) than depletion of these elements by subduction-related processes, such as HFSE retention in residual mantle or slab minerals (e.g. rutile). This is consistent with experimental results, which

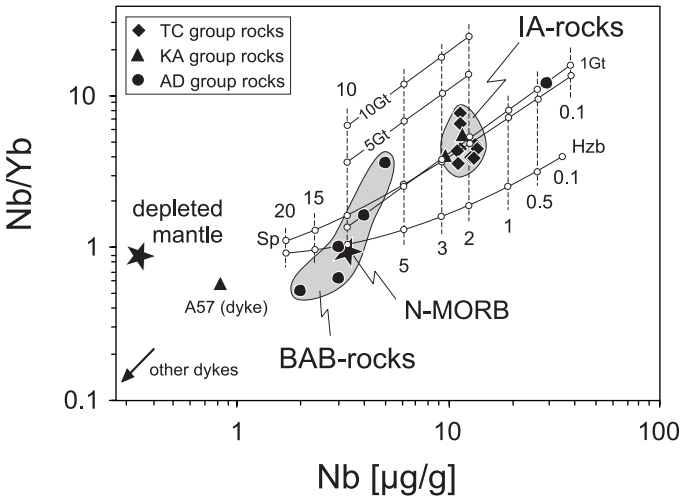

Fig. 10 Nb/Yb vs. Nb concentration. IA-rocks have higher Nb/Yb ratios and higher Nb concentrations than BAB-rocks due to lower degrees of melting, assuming the same source. Curves are calculated melting curves for spinel peridotite (Sp), harzburgite (Hzb), garnet peridotite containing 10 % garnet (10 Gt), 5 % garnet (5 Gt), and 1 % garnet (1 Gt). Details see text and Table 4. Numbers denote degree of melting (non-modal batch melting, partition coefficients from Bédard 1994 and Johnson 1998). Nb concentration is nearly independent of source composition but varies with degree of melting. Nb/Yb ratios are governed by the modal composition of the source

suggest that rutile saturation in island arc magmas is difficult to achieve, thus making the existence of HFSE-retarding phases in the source region of arc magmas unlikely (Ryerson and Watson 1987; Ionov and Hofmann 1995). We therefore assume that the Nb contribution from the slab to the source region of the IA-rocks is negligible, making Nb a potential indicator to estimate the degree of melting of the primary mantle wedge. Similar to the HFSE, the HREE are regarded as conservative elements, for which the contribution from the slab to the mantle wedge is also minimal (Pearce and Peate 1995). Therefore, we used Nb-Yb systematics to calculate the composition of melts produced by different degrees of melting and variable source compositions (Fig. 10), and applying the equation for non-modal batch melting (Shaw 1970; Albarède 1995). Starting concentrations of Nb and Yb in the source are taken as 0.35 µg/g and 0.39 µg/g, respectively. These values are reasonable estimates for the depleted upper mantle and are derived from the N-MORB composition of Hofmann (1988), assuming melting degrees of 10-15 %. The assumed Yb concentration is also in good agreement with the depleted mantle Yb concentration (0.4 µg/g) given by Johnson et al. (1990). Mantle and corresponding melt modes are taken from Woodhead et al. (1993) for spinel lherzolite, from Johnson (1998) for garnet peridotite, and from Kelemen et al. (1990) for harzburgite (Table 4). Additionally, initial garnet abundances are varied from the original composition of 10 % (Johnson 1998) to 5 % and 1 %. The lower garnet modes were compensated by olivine.

Our calculations indicate that the mantle source was either a moderately depleted spinel lherzolite similar to the recent MORB source mantle, or a more refractory garnet peridotite which underwent higher proportions of former melt extraction. Relatively low Nb/Yb ratios rule out a garnet proportion of more than 1-2 %. Independent of the source composition, the degree of melting was low for the IA-rocks (about 2-3 %). This is in good agreement with the degree of melting predicted for hydrous melting above subduction zones (2-8 %; Davies and Bickle 1991),

although our estimate is at the lower limit of this range. This may indicate a generally low fluid flux, as the degree of melting above subduction zones is proportional to the fluid flux from the slab (Stolper & Newman 1994). For the BAB-rocks the degree of melting was probably higher (8-15 %), assuming the same source. The dyke samples of the KA region (including T7) plot off the general trend for IA- and BAB-rocks (Fig. 10). Due to their extremely low Nb concentrations and very low Nb/Yb ratios, they cannot be derived from the same source as IA- and BAB-rocks and thus may represent later stage intrusion events of unknown age.

3.4.3 Source composition

High initial ϵ_{Nd} values up to +8.5 (Table 2) in the metapillows of the AD section (BAB-rocks in Fig. 8) indicate the existence of a long-term depleted mantle beneath Central Asia 570 Ma ago. Compared to the global evolution of Nd isotopes (e.g. Stein and Hofmann 1994), these values are close to the Nd isotopic composition of the depleted mantle 570 Ma ago, assuming that the depleted mantle evolution is defined by the upper limit of global initial ϵ_{Nd} values vs. time. In contrast, the ϵ_{Nd} values of the IA-rocks scatter around +5.5 (Table 2, Fig. 8) and lie on the Nd evolution line for major orogens (see Stein and Hofmann 1994). Therefore, the IA-rocks may either be attributed to a different source, which then would be less depleted than the upper mantle (e.g. a mixed primordial and depleted mantle source as suggested by Stein and Hofmann 1994), or may be the result of mixing and/or assimilation processes, where material derived from older continental crust lowers the initial ϵ_{Nd} values. Due to the variation of initial ϵ_{Nd} values of the IA-rocks, and due to mixing relationships described below, we favour the assumption of a similar source for BAB- and IA-rocks. This source was a long-term depleted mantle.

Pb isotopic compositions (Table 3) constrain the μ-value (= present day $^{238}U/^{204}Pb$) of the mantle source to have been 9.35 as a lower limit (Fig. 9a). We calculated this value by applying a two-stage Pb evolution model following Stacey and Kramers (1975) for the first step and assuming an age of the Earth of 4.57 Ga. The μ-value of 9.35 is slightly higher than the depleted mantle estimate of Doe and Zartman (1979)(μ = 8.92) but nevertheless underlines the existence of a depleted mantle source beneath Central Asia as derived from Nd-isotopes. Furthermore, the μ-value lies close to the more recent estimate of Hofmann (2001) (μ = 9.26), based on the average composition of MORB and assuming a single stage Pb evolution and an age of the Earth of 4.43 Ga. $^{206}Pb/^{204}Pb$ ratios of all samples, except the highly heterogeneous AD-series samples, lie within the range of age-corrected Atlantic, Pacific and Indian MORB (Fig. 9a; MORB data from Ito et al.1987; recalculated to 570 Ma using μ = 8.92). However, considering $^{207}Pb/^{204}Pb$ ratios there is an excess in ^{207}Pb compared to recalculated MORB samples. This excess probably reflects the existence of small amounts of old crustal material, either within the source itself and derived from the subducted slab, or assimilated by ascending melts. An excess in radiogenic ^{207}Pb in arc

magmas was also described by Münker (2000; Fig. 9a) for the 500 Ma old Devil River arc system in New Zealand. He showed, that this excess was produced by subducted sediments derived from an Archaean source.

From the well-defined correlation between $^{208}Pb/^{204}Pb$ vs. $^{206}Pb/^{204}Pb$ within the IA-rocks (Fig. 9b) we deduce a time-integrated Th/U ratio of their source of 3.1 ± 0.1 (1σ; disregarding the AD-series rocks). Compared to the present-day depleted mantle (Th/U ~ 2.5, Galer and O'Nions 1985), this indicates a slight long-term excess in ^{208}Pb over ^{206}Pb, which we also attribute to older crustal components with a long-term increased Th/U relative to the depleted mantle. In contrast, the BAB-rocks plot significantly to the right of the correlation defined by the IA-rocks, indicating an excess in ^{206}Pb, and thus a significantly lower time-integrated Th/U ratio for their source.

3.4.4 Mixing relationships vs. single parental melt

Although Cr and Ni correlations (Fig. 5), as well as Nb/Yb systematics (Fig. 10) allow the assumption of a common parental magma for most of the volcanic rocks, other trace element and isotopic characteristics require additional processes to have taken place during their evolution. In terms of Zr/Nb vs. Nb concentration, the BAB-rocks are characterized by high Zr/Nb ratios up to 50 (Fig. 11). The IA-rocks as well as the metapillows from the TC mélange and sample A23 have lower Zr/Nb ratios, but higher Nb concentrations (Fig. 11). Crystal fractionation fails to explain the correlation between the different groups of samples, as this process is not sufficient enough to produce such a large range in Zr/Nb ratios. This is demonstrated in Fig. 11 by the calculated fractionation trend for cpx, which produces a Zr/Nb variation being an order of magnitude too low to fit the observed data. Fractionation of other mafic phases will yield similar trends (e.g. 50 % Rayleigh fractionation of a primary magma having Zr/Nb = 30 would

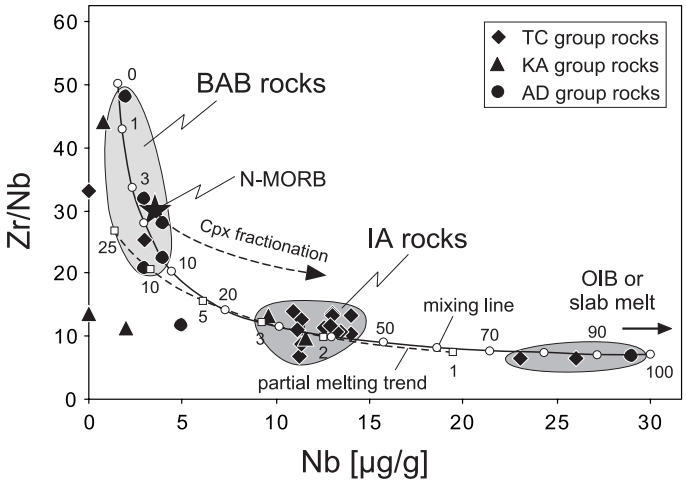

Fig. 11 Zr/Nb vs. Nb concentration. Variation of Zr/Nb ratios is an order of magnitude too large to be explained by fractional crystallization (e.g. cpx fractionation, length of arrow corresponds to 85% Rayleigh fractionation). Partial melting also fails to explain the whole range in Zr/Nb vs. Nb (lower dashed line, numbers denote degree of melting, partition coefficients from Bédard 1994). Therefore we infer a mixing relationship between a Nb-rich component („OIB-like" melt) and a highly depleted melt, superimposed on the partial melting trend connecting the IA- and low-Zr/Nb BAB-rocks. Mixing line was calculated by bulk mixing between the sample having the highest Nb concentration ("OIB-like" sample A23) and the sample having the highest Zr/Nb ratio (metapillow A43). Numbers are mixing proportions in %

lower this ratio to about 28 for cpx fractionation and to about 25 for amphibole fractionation). Partial melting is suitable to explain some of the variations within the IA- and low-Zr/Nb BAB-rocks as described previously and as shown by the partial melting curve for spinel peridotite in Fig. 11 (non-modal batch melting, parameters as given in Table 4). However, partial melting is not sufficient to explain the entire range in Zr/Nb ratios. Therefore, we suggest a mixing relationship superimposed on partial melting and fractional crystallization to explain the variation in Zr/Nb ratios. Bulk mixing between a high-Nb component (represented by the „OIB-like" sample A23) and a highly depleted primary melt, having a low Nb concentration and a high Zr/Nb ratio (represented by metapillow A43) is shown in Fig. 11. According to this, the admixture of up to about 10 % of the „OIB-like" component explains the Zr/Nb variation within the entire suite of BAB-rocks. As discussed in Münker (2000), melts with low Zr/Nb ratios but high Nb concentrations may also result from melting of a subducted slab, where Nb behaves much more incompatibly than Zr. We cannot rule out this assumption and therefore underline that the component termed „OIB-like" could also be a melt derived from slab melting. For example, 3 % modal batch melting of a N-MORB like slab consisting of garnet amphibolite having 10 % garnet results in a melt having ~30 µg/g Nb and Zr/Nb ~9 (Münker 2000). This is very close to sample A23. However, the „OIB-like" samples occur in the mélange of the ophiolite and are related to the forearc region of the subduction-accretion system. Therefore, they may rather represent fragments of an accreted, „OIB-like" terrane than melts derived from a recently subducted slab, where the thermal regime is unlikely to produce significant amounts of slab-derived melts.

Isotopic data provide further constraints on mixing relationships. Radiogenic lead ($^{208}Pb/^{206}Pb$)* is negatively correlated with initial $^{143}Nd/^{144}Nd$ (Fig. 12), and was calculated by subtracting primordial Pb (Tatsumoto et al. 1973) from measured ratios: ($^{208}Pb/^{206}Pb$)* = ($^{208}Pb/^{204}Pb$ - 29.476)/($^{206}Pb/^{204}Pb$ - 9.307). This correlation indicates the contamination of primary magmas with an evolved crustal component as high ($^{208}Pb/^{206}Pb$)* corresponds to a high long-term Th/U in the corresponding reservoir and thus correlates with low $^{143}Nd/^{144}Nd$. No significant differences exist whether age-corrected ($^{208}Pb/^{206}Pb$)* is used or not, indicating that differences in radiogenic Pb compositions derived from different Th/U ratios reflect long-living source heterogeneities. This is also evident from initial $^{207}Pb/^{204}Pb$, where higher values correspond to lower initial ϵ_{Nd}. The AD-pillows A22, A41 and A43 have the lowest ($^{208}Pb/^{206}Pb$)* ratios (0.877-0.913) and the most radiogenic $^{143}Nd/^{144}Nd$ (ϵ_{Nd} = +7.8 to +8.5). As shown above, these samples are thought to represent BAB-related melts from a depleted mantle source where contamination or crustal assimilation played a minor role. On the other hand, the island arc rocks have significantly lower initial $^{143}Nd/^{144}Nd$ (ϵ_{Nd} = +1.9 to +5.9) and slightly higher ($^{208}Pb/^{206}Pb$)* ratios (Fig. 12), indicating the involvement of older continental material during their evolution. To place constraints on the potential contaminant, we calculated a simple bulk mixing relationship between a primary melt

(represented by the BAB pillow lavas), and a sediment component. Due to the lack of geochemical data on regional sediments, we used the average composition of subducted sediments given by Plank and Langmuir (1998). As shown in Fig. 12, the IA-rocks plot along the calculated mixing line, making subducted sediments with moderate to low ϵ_{Nd} values the most likely contaminant during the evolution of the IA-rocks. This observation is consistent with mixing relationships derived from Zr/Nb systematics, but makes the involvement of an „OIB-like" component during melt generation unnecessary. Therefore, the „OIB-like" samples possibly represent isolated rock fragments accreted to the forearc region as described above, rather than components involved during magma genesis. This assumption is confirmed by the scatter in $(^{208}Pb/^{206}Pb)^*$ vs. $^{143}Nd/^{144}Nd$ of three from six AD-group rocks (Fig. 12), which suggests that they do not originate from a single source but rather represent different lithotectonic units.

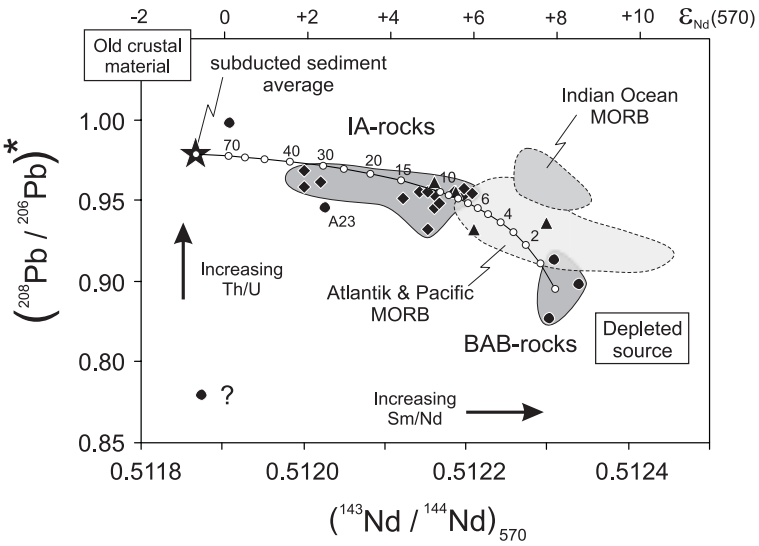

Fig. 12 Present day radiogenic $(^{208}Pb/^{206}Pb)^*$ vs. initial $^{143}Nd/^{144}Nd$. High $(^{208}Pb/^{206}Pb)^*$ indicates a high, long term Th/U of the source (or contaminant) and thus correlates with lower $^{143}Nd/^{144}Nd$. The IA-rocks have lower $^{143}Nd/^{144}Nd$ and increased $(^{208}Pb/^{206}Pb)^*$ compared to the most depleted rocks (BAB-rocks), indicating crustal contamination of the source or primary magma. The line denotes a bulk mixing line between a depleted melt (represented by the BAB pillow basalts) and average subducted sediment (star, data from Plank & Langmuir 1998; recalculated to 570 Ma), numbers give the amount of sediment (in %). Data for Atlantic, Pacific, and Indian Ocean MORB from Ito et al. (1987), age corrected to 570 Ma using the depleted mantle $^{147}Sm/^{144}Nd$ of 0.2140. Symbols as in Fig. 11

3.4.5 Crustal assimilation vs. source contamination

Several authors have estimated the flux and timing of material transfer from the slab to the mantle wedge (e.g. Morris et al. 1990; Hawkesworth et al. 1997; Regelous et al. 1997; Elliot et al. 1997; Johnson and Plank 1999), and constrained the behaviour of different elements during mass transfer. For example, Johnson and Plank (1999) pointed out that Rb, Sr, Ba and Pb are highly fluid mobile elements, whereas Th is only mobilized by melting of subducted sediments. Because most of the investigated samples were remarkably altered during low-grade metamorphism, the influence of fluid phases during melt generation is difficult to assess for the ATCO. On the other hand, as outlined above, low degrees of melting for the IA-rocks suggest low fluid fluxes from the slab. Additionally, we infer from the correlation between initial $(^{208}Pb/^{206}Pb)^*$ vs. $^{143}Nd/^{144}Nd$ (Fig.

12) that the source contaminant was at least partly a sedimentary component. However, as shown in Fig. 12, up to 40 % sediment admixture to a primary melt is required to explain the IA-rock compositions by bulk-mixing, which is rather unlikely due to heat balance considerations. Therefore, either direct sediment entrapment into the mantle source and subsequent melting or post-melting crustal assimilation and simultaneous crystal fractionation (AFC) is required to explain the mixing relationships. To further constrain this, we modelled fractional crystallization and combined crustal assimilation applying the equations of DePaolo (1981). We used Th/Yb ratios vs. initial $^{143}Nd/^{144}Nd$ since Th is sensitive to sediment or crustal contamination due to its low concentration in primary, depleted melts, and because Th is less affected by fluid-related mass transfer (Johnson and Plank 1999). Concentrations for Th and Yb in the contaminant were assumed to be represented by subducted sediment averages (6.5 µg/g and 4.6 µg/g; Plank and Langmuir 1998). Initial ϵ_{Nd} was varied between -10 and +6 to constrain the nature of the potential contaminant. The results are shown in Fig. 13. The ratio of assimilation to fractionation (r-parameter) must have been high assuming AFC processes (>0.8), since low ratios fail to explain the entire range in Th/Yb variation (lower r-values do not affect the shape of the calculated curves but the absolute range in Th/Yb). The results further indicate that a large range in ϵ_{Nd} values of the assimilated material is necessary to explain all data points, and that the ϵ_{Nd} values were not lower than +2 to produce the IA-rocks. Pre-existing Archaean or Proterozoic continental crust was therefore not involved during contamination. Although these considerations give some qualitative hints on the nature of the potential contaminant, and suggest that at least partly AFC processes may have taken place, we prefer the assumption of sediment entrapment into the mantle source and subsequent melting to be responsible for elevated ϵ_{Nd} values and Th excess within the IA-rocks. This is because of the following reasons: (1) assuming solely AFC

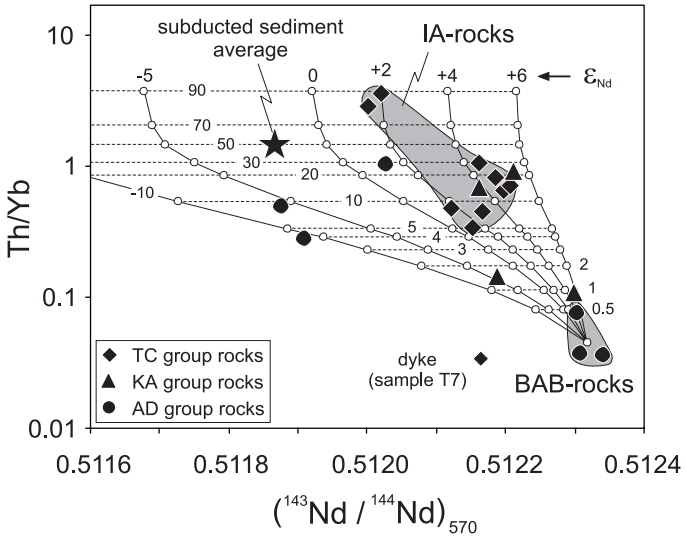

Fig. 13 Results of AFC calculations. Different curves represent different $^{143}Nd/^{144}Nd$ of assimilated material (numbers are ϵ_{Nd} values). Stippled lines are equilines and give the amount of mineral assemblage fractionated (consisting of 20 ol - 40 cpx - 40 plag, amount in %, partition coefficients from Bédard 1994; ratio of assimilation to fractionation: r = 0.8). Trace element composition of assimilated material was assumed to be equal to average subducted sediments (data from Plank & Langmuir 1998). High Th/Yb ratios within the IA-rocks require high amounts of assimilated crustal-like material. Details see text

processes, the ϵ_{Nd} values of the assimilated material must have been highly heterogeneous between at least 0 and +6 which is rather unlikely, (2) AFC processes require large amounts of crust to be assimilated (r = 0.8) which is inconsistent with the restricted range in Mg# of the IA-rocks, (3) signatures of subducted sediments in volcanic rocks from many island arc systems are a common feature (Patchett et al. 1984; White and Dupré 1986; Morris et al. 1990) and (4) because of the well constrained correlation between ($^{208}Pb/^{206}Pb$)* vs. $^{143}Nd/^{144}Nd$ (Fig. 12). Adding sediments prior to melting will not change the calculated shape of the mixing curve in Fig. 12, but will lower the absolute amount of sediment necessary to produce the IA-rocks to about 2-5 % within the source.

3.5 Conclusions

The volcanic rocks of the Agardagh Tes-Chem ophiolite (ATCO) can be subdivided into three groups in terms of their trace element and isotopic characteristics: (1) island arc rocks (IA-rocks) are characterized by enriched REE-patterns, negative Nb-anomalies, enrichment of LILE and intermediate initial ϵ_{Nd} values around +5.5; (2) back-arc basin related rocks (BAB-rocks) are characterized by flat REE patterns very similar to MORB, absent negative Nb-anomalies but highly radiogenic initial ϵ_{Nd} values up to +8.5; (3) intermediate and exotic rocks with both highly depleted and enriched REE patterns but intermediate to low initial ϵ_{Nd} values down to -0.6. The island arc and back-arc rocks are likely to be derived from the same depleted mantle source by different degrees of melting (2-3 % and 8-15 %, respectively). Modification of the mantle wedge by subducted sediments combined with mixing processes superimposed to crystal fractionation is suitable to explain most of the trace element and isotopic data.

Based on these results, we suggest the evolution of the ATCO as part of an intra-oceanic island arc back-arc system. The IA-rocks represent early stage volcanic rocks of a young arc system, where fluids and probably melts released from the downgoing slab initiated low-degree melting of a mantle wedge previously modified by accreted sediments. This led to highly enriched IA-rocks with intermediate initial ϵ_{Nd} values. The preservation of isotopic and trace element heterogeneities within this suite implies a very efficient and fast mechanism to transport the melts up to the surface. It further implies a restricted thickness of the overlying crust, where the storage and mixing of different magma batches is difficult to achieve. Therefore, this crust may have been pre-existing oceanic crust rather than a fragment of continental crust. We further suggested that, simultaneous to the formation of the IA-rocks, the BAB-rocks were formed in the back-arc region from the same depleted mantle source, but without the influence of slab-derived components. These rocks are therefore more depleted in highly incompatible trace elements and are highly radiogenic in $^{143}Nd/^{144}Nd$. This requires a hot, upwelling depleted mantle in the back-arc region to provide sufficient heat to produce these melts.

References

Albarède F (1995) Introduction to Geochemical Modeling. Cambridge University Press, 543 p.

Avdeyev AV (1984) Ophiolite Zones and the Geological History of Kazakhstan from the Mobilistic Standpoint. Intern Geol Rev 26: 995-1004

Bédard JH (1994) A procedure for calculating the equilibrium distribution of trace elements among the minerals of cumulate rocks, and the concentration of trace elements in the coexisting liquids. Chem Geol 118: 143-153

Belichenko VG, Sklyarov EV, Dobretsov NL, Tomurtogoo O (1994) Geodynamic map of Paleoasian ocean: Eastern segment. Russian Geol Geophys 35: 23-32

Berzin NA, Coleman RG, Dobretsov NL, Zonenshain LP, Xuchang X, Chang EZ (1994) Geodynamic map of the western part of the paleoasian ocean. Russian Geol Geophys 35: 5-22

Brenan JM, Shaw HF, Phinney DL, Ryerson FJ (1994) Rutile-aqueous fluid partitioning of Nb, Ta, Hf, Zr, U and Th: implications for high field strength element depletion in island-arc basalts. Earth Planet Sci Lett 128: 327-339

Buchan C, Cunningham D, Windley BF, Tomurhuu D (2001) Structural and lithological characteristics of the Bayankhongor Ophiolite Zone, Central Mongolia. J Geol Soc London 158: 445-460

Chauvel C, Hofmann AW, Vidal P (1992) HIMU-EM: The French-Polynesian connection. Earth Planet Sci Lett 110: 99-119

Coleman RG (1989) Continental growth of northwest China. Tectonics 8: 621-635

Conrad WK, Kay RW (1984) Ultramafic and Mafic Inclusions from Adak Island: Crystallization History, and Implications for the Nature of Primary Magmas and Crustal Evolution in the Aleutian Arc. J Petrol 25: 88-125

Davies JH, Bickle MJ (1991) A physical model for the volume and composition of melt produced by hydrous fluxing above subduction zones. Phil Trans R Soc Lond 335: 355-364

DePaolo DJ (1981) Trace-element and isotopic effects of combined wallrock assimilation and fractional crystallization. Earth Planet Sci Lett 53: 189-202

Didenko AN, Mossakovskii AA, Pecherskii DM, Ruzhentsev SV, Samygin SG, Kheraskova TN (1994) Geodynamics of the Central-Asian Paleozoic Oceans. Russian Geol Geophys 35: 48-61

Doe BR, Zartman RE (1979) Plumbotectonics, The Phanerozoic. In: Barnes HL (ed) Geochemistry of hydrothermal ore deposits, Wiley Interscience, pp 22-70

Eissen JP, Lefevre C, Maillet P, Morvan G, Nohara M (1991) Petrology and geochemistry of the central north Fiji basin spreading center (southwest pacific) between 16 degrees and 22 degrees. Mar Geol 98: 201-239

Elliot T, Plank T, Zindler A, White W, Bourdon B (1997) Element transport from slab to volcanic front at the Mariana arc. J Geophys Res 102: 14991-15019

Ez VV (1983) Correlation of endogenious processes and their role in the early Precambrian crustal development of southern east Siberia. In: Rast N, Delany FM (eds) Profiles of Orogenic Belts, AGU Geodynamic Series, no 10, pp 145-204

Fedorovskii VS, Khain EV, Vladimirov AG, Kargopolov SA, Gibsher AS, Izokh AE (1995) Tectonics, metamorphism, and magmatism of collisional zones of the Central Asian Caledonides. Geotectonics 29: 193-212

Frey FA, Green DH, Roy SD (1978) Integrated models of basalt petrogenesis: a study of quartz tholeiites to olivine melilitites from South Eastern Australia utilizing geochemical and experimental petrological data. J Petrol 19: 463-513

Galer SJG (1999) Optimal double and triple spiking for high precision lead isotopic measurement. Chem Geol 157: 255-274

Galer SJG, O'Nions RK (1985) Residence time of thorium, uranium and lead in the mantle with implications for mantle convection. Nature 316: 778-782

Garcia MO, Ito E, Eiler JM, Pietruszka AJ (1998) Crustal contamination of Kilauea Volcano magmas revealed by oxygen isotope analyses of glass and olivine from Pun Oo eruption lavas. J Petrol 39: 803-817

Goldstein S, O'Nions RK, Hamilton PJ (1984) A Sm-Nd isotopic study of atmospheric dusts and particulates from major river sediments. Earth Planet Sci Lett 70: 221-236

Hawkesworth CJ, Turner SP, McDermott F, Peate DW, van Calsteren P (1997) U-Th Isotopes in Arc Magmas: Implications for Element Transfer from the Subducted Crust. Science 276: 551-555

Hawkins JW Jr (1976) Petrology and geochemistry of basaltic rocks of the Lau Basin. Earth Planet Sci Lett 28: 283-297

Hawkins JW, Melchior JT (1985) Petrology of Mariana trough and Lau basin basalts. J Geophys Res 90: 11431-11468

Heath E, Macdonald R, Belkin H, Hawkesworth C, Sigurdsson H (1998) Magmagenesis at Soufriere Volcano, St. Vincent, Lesser Antilles Arc. J Petrol 39: 1721-1764

Hess PC (1992) Phase equilibria constraints on the origin of ocean floor basalts. Geophysical Monograph 71: 67-102

Hofmann AW (2001) Lead isotopes and the age of the Earth. Submitted to J Geol Soc London

Hofmann AW (1988) Chemical differentiation of the Earth: the relationship between mantle, continental crust, and oceanic crust. Earth Planet Sci Lett 90: 297-314

Ilyn AV (1990) Proterozoic supercontinent, its latest Precambrian rifting, breakup, dispersal into smaller continents, and subsidence of their margins: Evidence from Asia. Geology 18: 1231-1234

Ionov DA, Hofmann AW (1995) Nb-Ta-rich mantle amphiboles and micas: Implications for

subduction-related metasomatic trace element fractionations. Earth Planet Sci Lett 131: 341-356

Ito E, White WM, Göpel C (1987) The O, Sr, Nd and Pb isotope geochemistry of MORB. Chem Geol 62: 157-176

Jacobsen SB, Kaufman AJ (1999) The Sr, C and O isotopic evolution of Neoproterozoic seawater. Chem Geol 161: 37-57

Jenner GA, Longerich HP, Jackson SE, Fryer BJ (1990) ICP-MS - A powerful tool for high-precision trace-element analysis in earth sciences - evidence from analysis of selected USGS reference samples. Chem Geol 83: 133-148

Jochum KP, Laue HJ, Seufert HM, Dienemann C, Stoll B, Pfänder J, Flanz M, Achtermann H, Hofmann AW (1997) Multi-Ion Counting-Spark Source Mass Spectrometry (MIC-SSMS): A new multielement technique in geo- and cosmochemistry. Fresenius J Anal Chem 359: 385-389

Jochum KP, Seufert HM, Midinet-Best S, Rettmann E, Schönberger K, Zimmer M (1988) Multi-element analysis by isotope dilution-spark source mass spectrometry (ID-SSMS). Fresenius J Anal Chem 331: 104-110

Johnson KTM, Dick HJB, Shimizu N (1990) Melting in the oceanic upper mantle: An ion microprobe study of diopsides in abyssal peridotites. J Geophys Res 95: 2661-2678

Johnson KTM (1998) Experimental determination of partition coefficients for rare earth and high-field-strength elements between clinopyroxene, garnet, and basaltic melt at high pressure. Contrib Mineral Petrol 133: 60-68

Johnson MC, Plank T (1999) Dehydration and Melting Experiments Constrain the Fate of Subducted Sediments. Geochem Geophys Geosys

Kelemen PB (1990) Reaction between Ultramafic Rock and Fractionating Basaltic Magma I. Phase Realtions, the Origin of Calc-alkaline Magma Series, and the Formation of Discordant Dunite. J Petrol 31: 51-98

Kelemen PB, Johnson KTM, Kinzler RJ , Irving AJ (1990) High-field strength element depletions in arc basalts due to mantle-magma interaction. Nature 345: 521-524

Kepezhinskas KB (1986) Structural-metamorphic Evolution of late Proterozoic Ophiolites and Precambrian basement in the central Asian foldbelt of Mongolia. Precambr Res 33: 209-223

Kepezhinskas PK, Kepezhinskas KB, Puchtel IS (1991) Lower Paleozoic Oceanic Crust in Mongolian Caledonides: Sm-Nd Isotope and Trace Element Data. Geophys Res Lett 18: 1301-1304

Khain EV, Bibikova EV, Degtyarev KE (1999) The Paleo-Asian Ocean in the Neoproterozoic and early Palaeozoic: New Radiometric Data. In: Geological History of the Proterozoic marginal Palaeoceanic structures of northern Eurasia, St Petersburg, Tema, pp 175-181 (in Russian)

Khain VE, Gusev GS, Khain EV, Vernikovskym VA, Volobuyev MI (1997) Circum-Siberian

Neoproterozoic ophiolite belt. Ofioliti 22: 195-200

Kovalenko VI, Pukhtel IS, Yarmolyuk VV, Zhuravlev DZ, Stosch H, Jagoutz E (1996a) The Sm-Nd isotopic systematics of ophiolites in the Ozernaya Zone (Mongolia). Stratigraphy and Geological Correlation 4: 107-113

Kovalenko VI, Yarmolyuk VV, Kovach VP, Kotov AB, Kozakov IK, Salnikova EB (1996b) Sources of Phanerozoic granitoids in central Asia: Sm-Nd isotope data. Geochem Int 34: 628-640

Kozakov IK (1986) Precambrian infracrustal complexes of Mongolia. Nauka Publ House, Leningrad, 144 p (in Russian)

Kuzmichev AB, Bibikova EV, Zhuralev DZ (2001) Neoproterozoic (~800 Ma) orogeny in the Tuva-Mongolia massif (Siberia): island arc-continent collision an the northeaqst Rodiniaq margin. Precambr Res 110: 109-126

Melnikov AI, Mazukabzov AM, Sklyarov EV, Vasiliev EP (1994) Baikal rift basement: structure and tectonic evolution. Bull Centr Rech Explor Prod Elf Aquitaine 18: 99-122

Mitrofanov FP, Kozakov IK (1993) Precambrian in younger fold belts. In: Rundqvist DV, Mitrofanov FP (eds) Precambrian geology of the USSR, pp 443-498

Morris JD, Leeman WP, Tera F (1990) The subducted component in island arc lavas: constraints from Be isotopes and B-Be systematics. Nature 344: 31-36

Mossakovsky AA, Ruzhentsev SV, Samygin SG, Kheraskova TN (1993) The Central Asian fold belt: geodynamic evolution and formation history. Geotectonics 6: 3-32

Münker C (2000) The Isotope and Trace Element Budget of the Cambrian Devil River Arc System, New Zealand: Identification of Four Source Components. J Petrol 41: 759-788

Navon O, Stolper E (1987) Geochemical consequences of melt percolation - the upper mantle as a chromatographic column. J Geol 95: 285-307

Patchett PJ, White WM, Feldmann H, Kielinczuk S, Hofmann AW (1984) Hafnium/rare earth element fractionation in the sedimentary system and crustal recycling into the Earth's mantle. Earth Planet Sci Lett 69: 365-378

Peacock SM (1993) Large-scale hydration of the lithosphere above subducting slabs. Chem Geol 108: 49-59

Peacock SM, Rushmer T, Thompson AB (1994) Partial melting of subducting oceanic crust. Earth Planet Sci Lett 121: 227-244

Pearce JA, Ernewein M, Bloomer SH, Parson LM, Murton BJ, Johnson LE (1995) Geochemistry of Lau basin volcanic rocks: influence of ridge segmentation and arc proximity. Geol Soc London Spec Publ 81: 53-75

Pearce JW, Peate DW (1995) Tectonic implications of the composition of volcanic arc magmas. Annu Rev Earth Planet Sci 23: 251-285

Pedersen RB, Dunning GR (1997) Evolution of arc crust and relations between contrasting

sources: U-Pb (age), Nd and Sr isotope systematics of the ophiolite terraine of SW Norway. Contrib Mineral Petrol 128: 1-15

Pfänder JA, Jochum KP, Kröner A, Kozakov I, Oidup C, Todt W (1998) Age and geochemical evolution of an early Cambrian ophiolite-island arc system in Tuva, South Central Asia. In: Generation and Emplacement of Ophiolites Through Time. Geol Surv Finland, Spec Paper 26: 42

Pfänder JA, Jochum KP, Sassen A, Stoll B, Maissenbacher P, Murmann M (1999) Determination of Y, Zr and ultra-low Nb concentrations in geological material by multi-ion counting spark-source mass spektrometry (MIC-SSMS). Fresenius J Anal Chem 364: 376-380

Plank T, Langmuir CH (1998) The chemical composition of subducting sediment and its consequences for the crust and mantle. Chem Geol 145: 325-394

Presnall DC, Hoover JD (1987) High pressure phase equilibrium constraints on the origin of mid-ocean ridge basalts. In: Mysen BO (ed) Magmatic processes: Physicochemical Principles, pp 75-89

Rapp RP, Shimizu N, Norman MD, Applegate GS (1999) Reaction between slab-derived melts and peridotite in the mantle wedge: experimental constraints at 3.8 GPa. Chem Geol 160: 335-356

Regelous M, Collerson KD, Ewart A, Wendt JI (1997) Trace element transport rates in subduction zones: evidence from Th, Sr and Pb isotope data for Tonga-Kermadec arc lavas. Earth Planet Sci Lett 150: 291-302

Ryan J, Morris J, Bebout G, Leeman B (1996) Describing chemical fluxes in subduction zones: insights from "depth-profiling" studies of arc and forearc rocks. Geophysical Monograph 96: 263-268

Ryerson FJ, Watson EB (1987) Rutile saturation in magmas: implications for Ti-Nb-Ta depletion in island-arc basalts. Earth Planet Sci Lett 86: 225-239

Salnikova EB, Kozakov IK, Kotov AB, Kröner A, Todt W, Nutman A, Yakovleva SZ, Kovach VP (2001) Age of Palaeozoic granites and metamorphism in the Tuvino-Mongolian massif of the Central Asian Mobile Belt: loss of a Precambrian microcontinent. Precambr Res 110: 143-164

Sengör AMC, Okurogullari AH (1991) The role of Accretionary Wedges in the growth of continents: Asiatic examples from Argand to Plate Tectonics. Eclogae Geol Helv 84: 535-597

Sengör AMC, Natal'in BA, Burtman VS (1993) Evolution of the Altaid tectonic collage and Palaeozoic crustal growth in Eurasia. Nature 364: 299-307

Shaw DM (1970) Trace element fractionation during anatexis. Geochim Cosmochim Acta 34: 237-243

Shervais JW (1982) Ti-V plots and the petrogenesis of modern and ophiolitic lavas. Earth Planet Sci Lett 59: 101-118

Stacey JS, Kramers JD (1975) Approximation of terrestrial lead isotope evolution by a two-stage model. Earth Planet Sci Lett 26: 207-221

Stein M, Hofmann AW (1994) Mantle plumes and episodic crustal growth. Nature 372: 63-68

Stolper E, Newman S (1994) The role of water in the petrogenesis of the Mariana trough magmas. Earth Planet Sci Lett 121: 293-325

Sun Ss, McDonough WF (1989) Chemical and isotopic systematics of oceanic basalts: implications for mantle compositions and processes. Geol Soc Spec Pub 42: 313-345

Swinden HS, Jenner GA, Fryer BJ, Hertogen J, Roddick JC (1990) Petrogenesis and paleotectonic history of the Wild Bight Group, an Ordivician rifted island arc in Central Newfoundland. Contrib Mineral Petrol 105: 219-241

Tatsumi Y (1989) Migration of fluid phases and genesis of basalt magmas in subduction zones. J Geophys Res 94: 4697-4707

Tatsumoto M, Knight RJ, Allègre CJ (1973) Time differences in the formation of meteorites as determined from the ratio of lead-207 to lead-206. Science 180: 1279-1283

Thirlwall MF, Graham AM (1984) Evolution of high-Ca, high-Sr C-series basalts from Grenada, Lesser Antilles: the effects of intra-crustal contamination. J Geol Soc London 141: 427-445

White WM, Dupré B (1986) Sediment Subduction and Magma Genesis in the Lesser Antilles: Isotopic and Trace Element Constraints. J Geophys Res 91: 5927-5941

Woodhead J, Eggins S, Gamble J (1993) High field strength and transition element systematics in island arc and back-arc basin basalts: evidence for multi-phase melt extraction and a depleted mantle wedge. Earth Planet Sci Lett 114: 491-504

Woodhead JD, Eggins SM, Johnson RW (1998) Magma Genesis in the New Britain Island Arc: Further Insights into Melting and Mass Transfer Processes. J Petrol 39: 1641-1668

Zimmer M, Kröner A, Jochum KP, Reischmann T, Todt W (1995) The Gabal Gerf complex: A Precambrian N-MORB ophiolite in the Nubian Shield, NE Africa. Chem Geol 123: 29-51

Zonenshain LP, Kuzmin MI (1978) The Khan-Taishir Ophiolitic Complex of Western Mongolia, Its Petrology, Origin and Comparison with Other ophiolitic Complexes. Contrib Mineral Petrol 67: 95-109

Zonenshain LP, Kuzmin MI, Natapov LM (1990) Geology of the USSR: A Plate-Tectonic Synthesis. AGU Geodynamics Series 21

Appendix: Analytical methods

Major elements and Ba, Y, Sc, V, Cr, Co, Ni, Cu, Zn, and Ga were determined on a Philips PW 1404 X-ray fluorescence spectrometer at Universität Mainz using common XRF techniques on fused and powder pellets. Reproducibility is better than 1 % for major elements and better than 4 % for trace elements. FeO was calculated from Fe_2O_3 assuming that all iron was Fe^{II}. All other trace elements (except Rb, Sr, Sm, and Nd) were determined either by isotope dilution multi-ion counting spark-source mass spectrometry at the Max-Planck-Institut für Chemie in Mainz (MIC-SSMS; Jochum et al. 1997) or by ICP-MS at Memorial University in St. Jones, Newfoundland, Canada, following the technique of Jenner et al. (1990). For the MIC-SSMS measurement of very low Zr and Nb concentrations in Al-rich samples, a special procedure was necessary to correct for isobaric interferences. This procedure includes a high mass resolution (~3000) and a mathematical interference correction, and yields an analytical precision of 2-5 % for concentrations down to 0.02 µg/g and 10 % for lower concentrations (Pfänder et al. 1999). For all other trace elements, the precision of the MIC-SSMS technique is within 3-5 % of the recommended values for international reference materials for elements determined by isotope dilution and within 10 % for elements determined by the internal standard procedure (Jochum et al. 1988). The precision of the ICP-MS analyses is given to be better than 10 %.

Nd-, Sr-, and Pb isotopic compositions were measured on two Finnigan MAT 261 multicollector thermal ion-source mass spectrometers in static mode. Nd and Sr isotopic analyses and Nd, Sm, Sr, and Rb concentrations were analyzed on the same sample powder using mixed ^{150}Nd-^{149}Sm and ^{84}Sr-^{85}Rb spikes. After spiking, the sample powder was dissolved in HF-HNO_3 in closed Teflon® beakers for >48 hours at 200°C. Rb, Sr and REE were separated on Bio-Rad AG 50W-X12 cation-exchange resin. From the REE fraction, Sm and Nd were subsequently separated using HDEHP coated Teflon® powder. Total procedural blanks were <500 pg for Sr and <30 pg for Nd. Measured Sr isotopic ratios were normalized to $^{86}Sr/^{88}Sr = 0.1194$, Nd isotopic ratios to $^{146}Nd/^{144}Nd = 0.7219$. Repeated measurements of the NBS 987 Sr standard resulted in $^{87}Sr/^{86}Sr = 0.710212 \pm 0.000036$ and $^{84}Sr/^{86}Sr = 0.056495 \pm 0.000053$ (errors 2σ, N = 10). Repeated mesurements of the La Jolla Nd standard gave $^{143}Nd/^{144}Nd = 0.511839 \pm 0.000025$, $^{145}Nd/^{144}Nd = 0.348402 \pm 0.000017$ and $^{150}Nd/^{144}Nd = 0.236478 \pm 0.000082$ (2σ, N = 33). Pb was isolated from hand-picked rock chips up to 200 mg by weight. After leaching in hot 6M HCl for several hours and rinsing in ultrapure water, the chips were dissolved in closed Teflon® beakers using hot HF-HNO_3 for >48 hours. Pb separation was carried out on Bio-Rad AG1-X8 anion-exchange resin using a HBr-HCl procedure. Total procedural blanks are <200 pg. Mass fractionation was determined by repeated measurements of the NBS 981 Pb standard for each batch of samples and was between 1.02 ± 0.20 and 1.32 ± 0.05 ‰ per amu (± 2σ). Measured ratios of the NBS 981 Pb standard were

$^{208}Pb/^{204}Pb$ = 36.696 ± 0.049, $^{207}Pb/^{204}Pb$ = 15.490 ± 0.015, $^{206}Pb/^{204}Pb$ = 16.933 ± 0.012, $^{207}Pb/^{206}Pb$ = 0.91481 ± 0.00030 (± 2σ, N = 10, corrected for fractionation). Selected samples were re-measured for Pb isotopic composition by using the highly precise triple spike technique (Galer 1999). This technique requires the run of a spiked and unspiked sample aliquot to correct for instrumental mass fractionation but improves the accuracy of the isotopic ratios by at least a factor of 10. Sample dissolution was similar to the procedure described above, but separation was done on AG1-X8 resin using a diluted HBr-HNO_3 eluent to improve purity and blank on eluted Pb. Total procedural blanks using this technique were between 8 - 40 pg.

Chapter 4

Ultramafic cumulates and gabbros from boninitic primary melts and lower oceanic crustal evolution in the Agardagh Tes-Chem ophiolite (Tuva, Central Asia) - petrological and geochemical constraints

Jörg A. Pfänder, Klaus Peter Jochum, Choigun Oidup, Alfred Kröner

to be submitted to ***Journal of Petrology***

ABSTRACT

This study outlines the magmatic evolution of the mantle and lower plutonic section of a late Neoproterozoic island arc-related fragment of mafic crust, preserved in the Agardagh Tes-Chem ophiolite (ATCO) in Tuva, Central Asia (50.5° N, 95° E). Residual mantle rocks are characterized by high ratios of whole-rock Mg/Si, but low Al/Si, indicating a highly refractory character. This is consistent with high Cr# in dunite and harzburgite spinel (up to 0.83). The total degree of melt extraction from the residual mantle rocks was estimated to have been about 25 %, based on spinel compositions. Trace element abundances in clinopyroxene from ultramafic cumulates (pyroxenites and wehrlites) are extremely low between 0.1 and 1 times chondritic for rare-earth elements, with strongly light rare-earth element depleted patterns (chondrite-normalized $(La/Yb)_c$ = 0.27 - 0.52). Calculated equilibrium melts of ultramafic cumulates suggest boninitic primary magmas. The occurrence of ultramafic cumulates, associated with both primitive and highly evolved gabbroic rocks in the ATCO is explained by a two-stage magmatic process. Ultramafic cumulates were formed at the crust-mantle boundary within a deep-level, open-system magma chamber, where boninitic melts from the mantle wedge pooled and passed through on their way to the crust. These boninitic melts were produced by remelting of a refractory mantle in the mantle wedge of a subduction zone. The heat necessary for remelting most likely was supplied by an adjacent back-arc spreading center, which possibly was progagating towards the active arc system. More evolved magmas with lower densities were periodically expelled from the deep-level magma chamber to form mostly isolated (”trapped”), smaller intrusions in shallower crustal levels. These intrusions crystallized without significant replenishment, thus forming a wide variety of gabbroic rocks within a small region. However, trace element modifications of crystallizing melts occurred during wall-rock assimilation, leading to a large variation of Th/La ratios in the gabbros without a significant shift in Nd isotopic compositions. Assimilated crust was therefore pre-existing island arc crust rather than (older) continental crust.

4.1 Introduction

Ultramafic, mafic and intermediate plutonic rocks occur in different tectonic settings, and for mid-ocean ridge and supra-subduction zone type settings they are major constituents of the crust. For example, roughly two third of the oceanic crust consist of gabbroic rocks, including ultramafic cumulates and intrusions (Nicolas et al., 1996; Phipps Morgan et al., 1994), whereas volcanic rocks including sheeted dykes make up only less than a third of the total thickness of the oceanic crust. For island arc-like mafic crust, these proportion may be even more shifted towards plutonic rocks, depending on the age and crustal thickness of the magmatic arc system. Based on the investigation of volcanic rocks (e.g. Woodhead et al., 1998; Gamble et al., 1996), on experimental results (e.g. Kushiro 1990; Davies & Bickle, 1991) and, to a lesser extent, on xenoliths from calc-alkaline arc lavas (Conrad & Kay, 1984), some models have been proposed on how the magmatic plumbing system beneath active island arc systems works. A critical point, however, is that arc magmas pass through the entire crustal section before eruption, and this may obliterate primary signatures indicative for the formation of deeper crustal rocks. Especially for mature arc systems with already thickened crust, fractionation, assimilation and mixing processes are responsible for the elimination of primary melt signatures. Investigations focused on *in situ* petrogenesis of plutonic rocks and on the architecture of the deeper crust beneath island arc systems are therefore restricted to ophiolites (and to lesser extent to mafic xenoliths), which allow sampling of different levels of oceanic and island arc-like crust. Ophiolites have the special advantage in most cases to be directly linked to former island arc systems (e.g. Shervais, 2001), therefore frequently representing mafic arc-related juvenile crust. Numerous studies have elaborated on the framework of ophiolite formation, either by a structural approach and by combining field observations and geophysical results from active spreading systems (e.g. Nicolas 1989; Boudier et al. 1997; Phipps Morgan et al., 1994), or by geochemical investigations of mainly volcanic rocks (e.g. Rautenschlein et al., 1985; Smewing 1981). Additional information comes from petrological studies of mafic plutonic rocks, but geochemical and isotopic investigations of mafic plutonic rocks are scarce and restricted to a few well-known ophiolites (MacLeod & Yaouancq, 2000; Thompson et al., 1997; Briqueu et al., 1991; Göpel et al., 1984; Pallister & Knight, 1981).

This study presents mineral compositions measured by ion- and electron microprobe as well as major and trace element and Sr, Nd and Pb isotopic data of ultramafic and mafic to intermediate plutonic rocks from the well-preserved late Neoproterozoic Agardagh Tes-Chem ophiolite (ATCO) in Tuva, Central Asia (Fig. 1). The evolution of this ophiolite is closely related to a subduction zone, and due to deep-level erosion, the southwestern part offers a unique opportunity to examine the petrological and geochemical composition and magmatic evolution of ultramafic plutonic rocks that build the lowest part of island arc-related crust. An associated, well-preserved and undisturbed gabbroic intrusion in the central part of the ophiolite (Fig. 1) is further ideally suited to investigate

crystal fractionation and wall-rock assimilation that operate during gabbro formation in mid-crustal levels in a virtually closed magmatic system. In this context we constrain (1) the nature of the ultramafic rocks, whether they are residual mantle rocks or ultramafic cumulates, (2) the composition and origin of primary melts generated in the sub-arc mantle wedge of the ATCO, (3) the petrological and isotopic composition of the mantle source and the total degree of melt extraction, (4) the genetic relationships between the ultramafic and gabbroic rocks, and their relation to the volcanic rocks of the ATCO, (5) the order of crystallization and depth of gabbro formation, (6) the nature of the gabbroic intrusion, whether open or closed system, and (7) the composition of pre-existing arc-crust assimilated during gabbro crystallization.

Based on our data we propose a comprehensive petrogenetic model to explain the evolution of the lower and middle crust in the ATCO. This model suggests a combined evolution of ultramafic and gabbroic rocks within a young intra-oceanic island arc back-arc system. Ultramafic cumulates crystallized in a deep-level, open-system magma chamber, whereas gabbroic rocks formed from more evolved melts by static crystallization of a smaller intrusion at shallower crustal levels.

4.2 Geological setting

The geology of the ATCO (Fig. 1) and its evolution as part of the Central Asian Mobile Belt (CAMB, also called Altaides; see Sengör et al., 1993) was described elsewhere (Pfänder et al., submitted) and will only briefly be summarized here. The ophiolite is a fragment of mafic crust generated as part of an intraoceanic island arc back-arc system (Pfänder et al., submitted). During the early stage of accretion of the CAMB, the ATCO was obducted onto the passive continental margin of the Tuva-Mongolian microcontinent (Kuzmichev et al., 2001). The age of the ophiolite is 569.6 ± 1.7 Ma and was derived from single zircon Pb-Pb evaporation data of a plagiogranite body associated with ultramafic and gabbroic rocks (unpublished data; Pfänder et al. 1998). The entire ophiolite section is tectonically disturbed and embedded within a tectonic mélange consisting of metasedimentary rocks, carbonates and cherts as well as sheared pillow lavas and massive basaltic andesites. Three units are distinguished (Fig. 1): (1) the Agardagh zone (ADZ) which is dominated by variably serpentinized ultramafic rocks, (2) the Karachat zone (KAZ) which represents an intrusive body dominated by hornblende-bearing gabbros, and (3) the Tes-Chem zone (TCZ) which is regarded as the lower to intermediate part of a sheeted dyke complex comprising mainly basaltic rocks and microgabbros.

In the ADZ, highly serpentinized harzburgites and dunites are chaotically associated with slices of wehrlite, pyroxenite and gabbro. Small bodies of chromitite are also present. Serpentinite shear zones, up to several tens of metre wide contain blocks of massive basalts, pillow lavas and mafic to intermediate plutonic rocks. The entire ADZ is overlain by sedimentary rocks comprising

carbonates, shales, schists and cherts interlayered with intermediate massive volcanic rocks (Fig. 1).

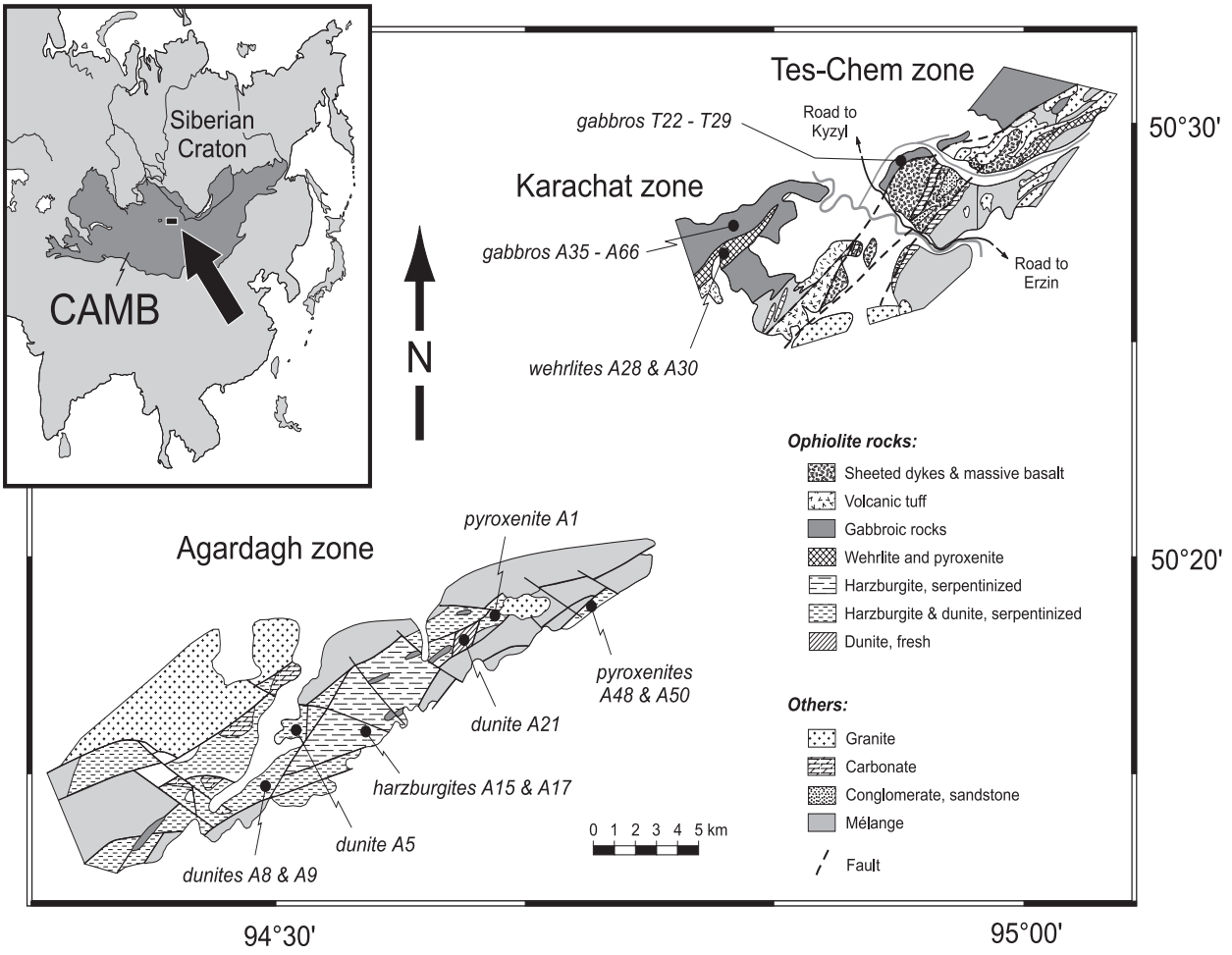

Fig. 1 Simplified geological map of the Agardagh Tes-Chem ophiolite with sampling locations. Inset: position of the ophiolite within the Central Asian Mobile Belt (CAMB).

Field observations in the plutonic section (KAZ) of the ATCO suggest a relatively small magmatic body, about 4-5 km long, 1-2 km wide and several 100 m thick (Fig. 1). This body consists of a wide variety of plutonic rocks, comprising isotropic and modally layered olivine-gabbros, hornblende-bearing gabbros, gabbronorites, norites and minor diorites. Layering within the lower gabbroic section of the KAZ is striking about N-S, dipping to the E by about 60°. More evolved quartz-bearing gabbros and gabbrodiorites occur to the W, thus tending towards the top of the proposed magma chamber, whereas to the E more primitive, clinopyroxene-rich cumulates occur. The internal stratigraphy of the KAZ is disturbed, i.e. the upper level of the intrusion borders the ultramafic unit to the W, whereas the lower level borders the sheeted dyke and volcanic complex to the E. The gabbroic complex continues to the NE (TCZ, Fig. 1), where the internal

stratigraphy is repeated. We propose that the entire gabbroic complex was tectonically thickened along fault systems during obduction, now forming a repeated duplex structure.

The samples analyzed within this study are dunites and harzburgites from the ADZ, wehrlites and pyroxenites from the ADZ and from the basal section of the KAZ as well as gabbroic rocks from the KAZ and from the northern part of the TCZ.

4.3 Petrography and mineral compositions

4.3.1 Petrographic description

A condensed petrographic description and modal compositions of ultramafic rocks and gabbros are given in Tab. 1. Modes were calculated using a least-square fit based on whole-rock analyses and mineral compositions (Metzner & Grimmeisen, 1990). Where mineral compositions are not available, these were calculated by assuming ideal solid solutions between mineral end-members. This treatment usually provides good agreements with modes calculated from mineral compositions. All modes were calculated as hornblende-free, as hornblende is regarded as a late-stage, subsolidus phase.

Ultramafic rocks comprise harzburgites and dunites as well as pyroxenites and wehrlites. The degree of serpentinization of the dunites is variable between about 30 % up to nearly 100 %. The harzburgites are completely serpentinized with no primary mineral phases preserved, except one sample which contains relict spinel (T97A15, note that samples will be denoted without „T97" in the following). The pyroxenites and wehrlites are fresh with few or no secondary mineral phases (such as hornblende). Interstitial plagioclase is absent. Chrome spinel is present as a disseminated, interstitial phase in all dunites, one wehrlite, one pyroxenite and one harzburgite. Idiomorphic, cumulus spinel is generally absent. Harzburgites and dunites (except dunite A21) are strongly sheared with nearly horizontal foliations and lineations trending roughly NW-SE. Gabbroic rocks comprise norite, gabbronorite, olivine-gabbro, quartz-bearing gabbro, hornblende-gabbro, gabbrodiorite and diorite. Magmatic twins are scarce in gabbro clinopyroxenes, whereas orthopyroxene (opx) exsolutions are abundant, indicating subsolidus re-equilibration. As a result of low-grade metamorphism, clinopyroxene (cpx) is partly recrystallized. Zonation in plagioclase is nearly absent, indicating slow cooling. Green hornblende (hbl) is abundant in most gabbroic rocks and occurs either as interstitial or poikilitic phase, typically enclosing cpx. Clinopyroxene to hornblende transitions, where hornblende replaces cpx, are common. Opaque phases are magnetite and ilmenite, where rutile exsolution from ilmenite is frequent. The degree of alteration of the gabbros is variable. Secondary phases, if present, are chlorite, zoisite, clinozoisite, epidote and actinolite.

Table 1: Petrographic description and modal compositions of ultramafic and gabbroic rocks

					Modal compositions[2]									Comment
Rock type	**Sample**	**Loc.[1]**	**Alteration**	**Minerals**	**ol**	**plag**	**cpx**	**opx**	**mag**	**ilm**	**sp**	**qz**	**sum**	
Ultramafic rocks														
Dunite	T97A5	ATZ	high	ol, sp, mag										ol inclusion in sp
Dunite	T97A8	ATZ	high	ol, sp										
Dunite	T97A9	ATZ	high	ol, sp										
Dunite	T97A21	ATZ	low	ol, sp										
Harzburgite	T97A15	ATZ	very high	serp, sp										secondary cc, strongly serpentinized, only sp preserved
Pyroxenite	T97A1	ATZ	low-middle	cpx										cpx twins, ol inclusion (Fo = 0.96) in cpx
Pyroxenite	T97A48	ATZ	low	cpx, sp, mag										sp inclusions in cpx
Pyroxenite	T97A50	ATZ	low	cpx, mag										cpx twins, sp free
Wehrlite	T97A28	KAZ	low	ol, cpx, mag, ±sp	38	--	56	--	3.8	--	+/-	--	98.1	cpx exsolution, cpx twins, cpx inclusion in ol, very less sp
Wehrlite	T97A30	KAZ	low	ol, cpx, mag, ±sp	26	--	68	--	3.5	--	+/-	--	97.4	Al-rich spinel
Gabbros														
Ol-gabbro	T97A54	KAZ	low	ol, cpx, plag, mag	20	43	35	--	1.3	0.2	--	--	99.8	primary & scondary cpx, cpx exsolution, plag inclusions in cpx
Gabbro	T97A64	KAZ	high	cpx, plag, mag, ilm	--	55	41	--	1.1	0.5	--	--	97.3	
Leucogabbro	T97A55	KAZ	middle	cpx, plag, mag, ilm	--	81	18	--	0.4	0.2	--	--	99.8	
Leucogabbro	T97A66	KAZ	middle	cpx, plag, mag, ilm	--	75	24	--	0.6	0.2	--	--	99.5	
Gabbronorite	T97A35	KAZ	low	opx, cpx, plag, mag, ilm	--	31	37	29	2.3	0.6	--	--	99.7	exsolution in opx and cpx, ilm exsolution, hbl free
Gabbronorite	T97A60	KAZ	low	opx, cpx, hbl, plag, ilm, Ti-mag	--	56	21	22	1.6	0.3	--	--	100.7	opx exsolution
Hbl-gabbro	T97A36	KAZ	high	plag, hbl, ilm	--	57	39	--	1.9	1.1	--	--	99.1	ilm exsolution
Hbl-gabbro	T97A56	KAZ	middle-high	hbl, plag, cpx,mag, Ti-mag, ±qz	--	58	37	--	2.5	2.4	--	+/-	99.5	
Gabbrodiorit	T97A61	KAZ	low-middle	hbl, cpx, plag, qz, mag, Ti-mag	--	55	31	--	1.7	1.3	--	10	99.7	poikilitic (hbl matrix)
Gabbrodiorit	T97A53	KAZ	middle	hbl, plag, qz, garnet, apatite	no data available									
Gabbrodiorit	T97A62	KAZ	middle	hbl, plag, qz	--	47	42	--	1.5	1.0	--	8.7	99.6	plag and qz inclusions in hbl
Diorite	T97A63	KAZ	high	qz, hbl, plag, ±sp, ±sphene	--	54	28	--	1.1	0.7	--	16	99.6	contains low Cr-spinel and sphene
Gabbrodiorite	T97T21	TCZ	middle-high	cpx, plag, mag, qz	no data available									
Norite	T97T27a	TCZ	middle-high	plag, opx, hbl	--	74	--	24	0.9	0.4	--	--	99.7	plag dominates, interstitial hbl
Hbl-gabbro	T97T27b	TCZ	middle-high	cpx, plag, hbl	--	17	80	--	1.6	1.0	--	--	99.2	
Hbl-gabbro	T97T28	TCZ	middle-high	cpx, hbl, plag	--	59	39	--	1.0	0.4	--	--	99.1	
Hbl-gabbro	T97T29	TCZ	middle-high	cpx, hbl, plag	--	60	40	--	0.9	0.0	--	--	100.3	secondary hbl with low-Al and alkalines

[1] ATZ = Agardagh zone, KAZ = Karachat zone, TCZ = Tes-Chem zone. [2] Modes calculated from whole-rock analyses using a least-square fit (details see text, after Metzner & Grimmeisen, 1990) ol = olivine, opx = orthopyroxene, cpx = clinopyroxene, plag = plagioclase, hbl = hornblende, qz = quartz, serp = serpentinite, sp = spinel, mag = magnetite, ilm = ilmenite, cc = calcite

Table 2: Average mineral compositions (wt%) of ultramafic and gabbroic rocks

	Olivine compositions							**Clinopyroxene compositions**									
	Dunites, wehrlites and gabbros							**Pyroxenites and Wehrlites**					**Gabbros**				
	ADZ				**KAZ**			**ADZ**			**KAZ**		**KAZ**				
Sample	T97A5	T97A8	T97A9	T97A21	T97A28	T97A30	T97A54	T97A1	T97A48	T97A50	T97A28	T97A30	T97A35	T97A54	T97A56	T97A60	T97A61
Type	Dunite^{m}	Dunite^{m}	Dunite^{m}	Dunite	Wehrlite	Wehrlite	Gabbro	Pyxite	Pyxite	Pyxite	Wehrlite	Wehrlite	Gabbro	Gabbro	Gabbro	Gabbro	Gabbro
SiO_2	41.38	41.43	40.83	40.29	39.11	39.09	37.05	52.75	52.76	53.06	51.99	52.30	52.09	50.83	52.10	52.29	51.21
TiO_2	0.00	0.01	0.00	0.00	0.00	0.00	0.01	0.07	0.09	0.08	0.10	0.12	0.22	0.23	0.22	0.22	0.22
Al_2O_3	0.00	0.00	0.01	0.01	0.00	0.00	0.01	1.90	2.39	2.34	3.01	2.58	1.88	2.83	1.55	1.69	1.61
Cr_2O_3	0.02	0.06	0.04	0.02	0.02	0.02	0.01	0.80	0.71	0.55	0.27	0.28	0.07	0.12	0.05	0.02	0.01
FeO	2.00	5.31	4.55	8.71	17.21	18.17	25.11	3.30	3.34	3.60	4.52	4.26	9.69	6.05	12.21	11.26	12.35
MgO	56.61	53.00	54.64	51.68	43.89	43.08	37.99	18.09	17.48	17.33	16.74	16.74	13.80	15.98	12.28	13.16	12.06
MnO	0.40	0.65	0.46	0.13	0.28	0.29	0.39	0.13	0.13	0.13	0.14	0.14	0.28	0.19	0.47	0.39	0.50
CaO	0.00	0.03	0.03	0.02	0.01	0.01	0.01	22.87	23.50	23.48	23.55	23.93	21.88	22.84	21.92	21.71	21.15
NiO	0.37	0.19	0.33	0.38	0.07	0.08	0.04	0.03	0.02	0.01	0.01	0.02	0.01	0.00	0.02	0.02	0.00
Na_2O	0.00	0.00	0.01	0.01	0.01	0.01	0.00	0.18	0.16	0.12	0.04	0.05	0.28	0.17	0.27	0.31	0.31
K_2O	0.01	0.01	0.00	0.01	0.00	0.00	0.01	0.00	0.01	0.00	0.00	0.00	0.01	0.00	0.00	0.00	0.01
Total	100.8	100.7	100.9	101.2	100.6	100.8	100.6	100.1	100.6	100.7	100.3	100.4	100.2	99.25	101.1	101.1	99.42
Mg#	0.98	0.95	0.96	0.91	0.82	0.81	0.73	0.91	0.90	0.90	0.87	0.88	0.72	0.82	0.64	0.68	0.64
Cr#	--	--	--	--	--	--	--	--	--	--	--	--	--	--	--	--	--
An	--	--	--	--	--	--	--	--	--	--	--	--	--	--	--	--	--

ADZ = Agardagh zone, KAZ = Karachat zone, TCZ = Tes-Chem zone. Pyxite = Pyroxenite, ^{m} = metamorph. Note that gabbro is used for all gabbroic rocks

Table 2: continued

	Clinopyroxene compositions					Orthopyroxene compositions			Hornblende compositions							
	Gabbros					Gabbros			Gabbros							
		TCZ				KAZ		TCZ	KAZ						TCZ	
Sample	T97A64	T97T21	T97T27a	T97T28	T97T29	T97A35	T97A60	T97T27a	T97A36	T97A56	T97A60	T97A61	T97A62	T97A63	T97T27a	T97T28
Type	Gabbro	Gabbro	Gabbro	Gabbro	Gabbro	Gabbro	Gabbro	Gabbro	Gabbro	Gabbro	Gabbro	Gabbro	Gabbro	Gabbro	Gabbro	Gabbro
SiO_2	53.37	50.84	53.29	51.99	52.01	52.64	52.19	55.45	49.39	46.10	48.14	43.58	47.38	46.18	49.92	51.80
TiO_2	0.13	0.66	0.15	0.32	0.32	0.11	0.10	0.07	0.71	1.35	1.07	1.52	1.07	0.95	0.99	0.24
Al_2O_3	4.55	2.31	1.09	2.36	4.12	1.17	0.97	1.41	6.82	8.71	7.52	10.36	8.20	7.68	6.36	4.90
Cr_2O_3	0.15	0.01	0.13	0.13	0.07	0.05	0.03	0.06	0.03	0.01	0.02	0.01	0.09	0.06	0.20	0.08
FeO	9.27	9.27	7.70	6.75	10.14	24.34	27.03	17.89	13.57	17.61	15.02	19.25	16.04	15.46	11.61	8.80
MgO	18.23	16.00	14.68	15.30	17.49	21.71	19.58	21.96	14.88	11.41	13.67	9.56	12.52	12.93	16.35	18.30
MnO	0.27	0.34	0.24	0.18	0.23	0.60	0.81	0.57	0.25	0.29	0.25	0.33	0.31	0.37	0.19	0.15
CaO	12.65	19.84	23.39	22.63	13.39	0.78	0.87	1.56	11.35	11.35	11.46	11.02	10.94	10.92	11.76	11.80
NiO	0.01	0.00	0.01	0.01	0.00	0.03	0.02	0.01	0.02	0.02	0.01	0.00	0.03	0.00	0.02	0.02
Na_2O	0.46	0.33	0.29	0.22	0.43	0.01	0.01	0.15	0.81	1.22	0.93	1.54	0.95	1.05	0.90	0.64
K_2O	0.06	0.00	0.01	0.01	0.10	0.01	0.01	0.01	0.05	0.17	0.10	0.31	0.20	0.20	0.09	0.08
Total	99.17	99.60	101.0	99.89	98.29	101.4	101.6	99.13	97.89	98.24	98.20	97.47	97.71	95.80	98.39	96.82
Mg#	0.78	0.75	0.77	0.80	0.75	0.61	0.56	0.69	0.66	0.54	0.62	0.47	0.58	0.60	0.72	0.79
Cr#	--	--	--	–	--	–	--	--	–	--	--	–	--	--	--	--
An	--	--	--	–	--	–	--	--	–	--	--	–	--	--	--	--

Table 2: continued

	Spinel compositions							Plagioclase compositions								
	Ultramafic rocks							Gabbros								
	ADZ						KAZ	KAZ						TCZ		
Sample	T97A5	T97A8	T97A9	T97A21	T97A15	T97A48	T97A30	T97A35	T97A36	T97A56	T97A60	T97A61	T97A62	T97T27a	T97T28	T97T29
Type	Dunite	Dunite	Dunite	Dunite	Harzb.	Pyxite	Wehrlite	Gabbro	Gabbro	Gabbro	Gabbro	Gabbro	Gabbro	Gabbro	Gabbro	Gabbro
SiO_2	0.12	0.25	0.12	0.12	0.23	0.12	0.12	45.80	46.17	48.65	48.36	50.25	48.64	46.61	44.45	44.02
TiO_2	0.00	0.00	0.07	0.00	0.02	0.17	0.13	0.00	0.00	0.00	0.01	0.02	0.02	0.01	0.01	0.01
Al_2O_3	11.90	11.82	8.86	21.71	13.21	27.84	40.00	34.56	34.06	32.34	32.63	30.77	31.38	34.12	34.43	34.88
Cr_2O_3	58.64	58.17	62.43	47.29	55.47	34.07	17.09	0.02	0.02	0.02	0.02	0.00	0.02	0.02	0.01	0.00
FeO	19.94	20.24	18.46	20.49	21.17	29.09	33.01	0.21	0.28	0.23	0.23	0.16	0.84	0.29	0.35	0.05
MgO	10.31	9.96	11.39	11.77	10.00	9.48	9.69	0.01	0.01	0.00	0.01	0.00	0.09	0.11	0.01	0.00
MnO	0.38	0.37	0.36	0.35	0.36	0.42	0.32	0.03	0.02	0.03	0.02	0.02	0.04	0.02	0.01	0.01
CaO	0.01	0.01	0.00	0.01	0.01	0.01	0.02	17.91	17.67	16.06	16.33	13.67	17.09	17.44	18.19	18.68
NiO	0.04	0.04	0.03	0.07	0.05	0.07	0.06	0.01	0.01	0.03	0.01	0.00	0.01	0.02	0.00	0.00
Na_2O	0.00	0.02	0.02	0.01	0.02	0.01	0.02	1.32	1.54	2.57	2.45	3.68	1.04	1.65	0.95	0.84
K_2O	0.00	0.00	0.00	0.00	0.01	0.00	0.01	0.00	0.01	0.02	0.02	0.03	0.35	0.03	0.03	0.01
Total	101.3	100.9	101.7	101.8	100.5	101.3	100.5	99.88	99.79	99.95	100.1	98.59	99.52	100.3	98.42	98.51
Mg#	0.48	0.47	0.52	0.51	0.46	0.37	0.34	--	--	--	--	--	–	--	--	--
Cr#	0.77	0.77	0.83	0.59	0.74	0.45	0.22	--	--	--	--	--	--	--	--	--
An	--	--	–	–	--	--	--	0.88	0.86	0.78	0.79	0.67	0.90	0.85	0.91	0.92

4.3.2 Olivine compositions

Olivine compositions range from Fo_{91} to Fo_{98} in dunites and are around Fo_{82} in wehrlites (Tab. 2). Only one olivine-gabbro is present having Fo_{73}. Fo-content in dunite olivine is extremely high for two samples (A5 and A9) and exceeds the range usually measured in abyssal peridotites (0.90 - 0.91; Dick, 1989; Ross & Elthon, 1997a; Elthon et al., 1992) and oceanic cumulates (0.85 - 0.90; Ross & Elthon, 1993). Comparably high Fo contents are only known from metamorphic olivines (up to $Fo_{98.6}$), which tend to have increased Fo with increasing degree of metamorphism (O'Hanley, 1996; Evans, 1977). Therefore, dunite olivine may be at least partly recrystallized serpentinite, although typical metamorphic textures and parageneses are absent in the dunite samples. NiO concentrations (Tab. 2) are between 0.18 % and 0.38 % in dunite olivine, and between 0.04 % and 0.08 % in wehrlite and gabbro olivine (Tab. 2). Dunite sample A9 contains two olivine generations with nearly the same Fo content (0.95 and 0.96, respectively), but significantly different NiO concentrations (0.15 % and 0.45 %, respectively). We attribute this to olivine recrystallization from serpentinite during low grade metamorphism, which may also explain the spread in NiO concentrations in sample A8. MnO in dunite olivine is variable between 0.13 % and 0.62 %, in wehrlite olivine 0.28 % and 0.29 %, and 0.39 % in olivine-gabbro A54. Abyssal peridotites in contrast have lower MnO concentrations between 0.09 % and 0.21 % (Dick, 1989; Hellebrand et al., submitted). Elevated MnO contents in dunite olivine are therefore consistent with deserpentinization caused by a low-grade metamorphic overprint.

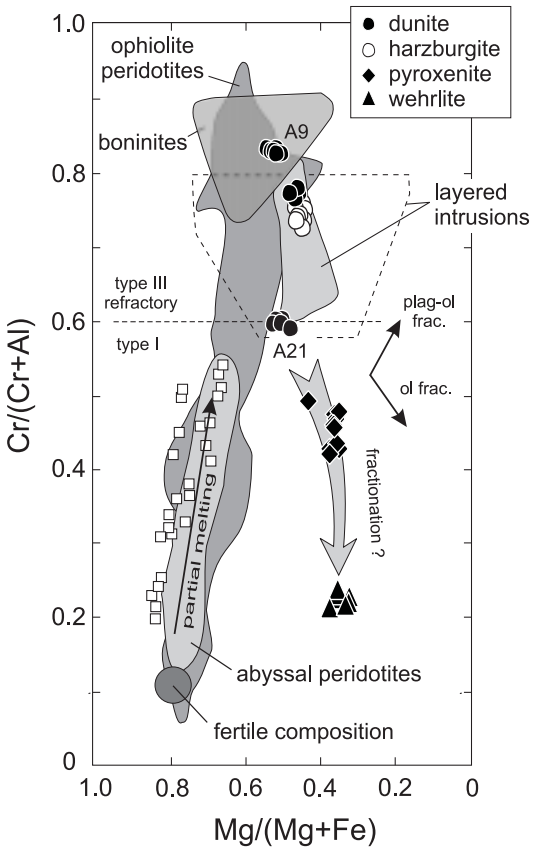

Fig. 2 Spinel compositions of ultramafic rocks (each point represents a mineral average). Dunite and harzburgite plot within the refractory fields of ophiolite peridotites and layered intrusions. Note relatively low Cr# in dunite sample A21. Pyroxenite and wehrlite have Cr# comparable to abyssal peridotites but much lower Mg# due to preceeding olivine and/or olivine-spinel fractionation. White squares: composition of spinels from East Pacific MORB (data from Allan et al., 1988). Boninite field: spinels from Mariana forearc boninites (data from Bloomer 1983, diagram modified from Dick and Bullen, 1984).

4.3.3 Orthopyroxene compositions

Orthopyroxene (opx) is absent in ultramafic rocks and scarce in gabbroic rocks, i.e. only three samples are opx-bearing. From these three samples, two are gabbronorites and one is a norite

(Tab. 1). Orthopyroxene is Ca-poor hypersthene with Mg-numbers (Mg# = molar $Mg/[Mg+Fe^{II}]$) between 0.56 and 0.69, and CaO between 0.78 % and 1.56 %. Al_2O_3 varies between 0.97 % and 1.41 %, and Cr_2O_3 concentrations are 0.03 % - 0.06 %. TiO_2 is low and varies between 0.07 and 0.11 %.

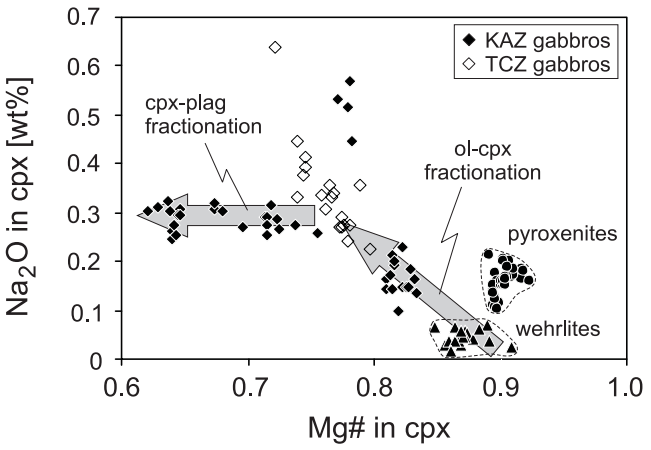

Fig. 3 Na_2O vs. Mg# in clinopyroxene of ultramafic rocks and gabbros. Circles: pyroxenites, triangles: wehrlites, rhombs: gabbros (open: TCZ, filled: ATZ). Each point represents a mineral average. Na-content in cpx increases with decreasing Mg# indicating ol-cpx and subsequent cpx-plag fractionation. Pyroxenites plot off the general trend. TCZ gabbro cpx tends to have more Na than ATZ gabbro cpx.

4.3.4 Spinel compositions

Dunite and harzburgite spinels have high Mg# and Cr-numbers (Cr# = molar $Cr^{III}/[Cr^{III}+Al]$) from 0.46 - 0.52 and 0.59 - 0.83, respectively (Tab. 2, Fig. 2). Cr# is generally higher and Mg# is lower than in most abyssal peridotites (Fig. 2). Pyroxenite and wehrlite spinels have lower Mg# (0.37 and 0.34, respectively) and Cr# (0.45 and 0.22, respectively) and plot away from the fields of ultramafic cumulates and residual abyssal peridotites (Fig. 2). TiO_2 decreases with increasing Cr# and is equal or lower than 0.07 % in dunite and harzburgite spinel, attesting to the residual nature of these rocks. Ti concentrations are significantly higher in pyroxenite and wehrlite spinel (0.17 and 0.13 %, respectively).

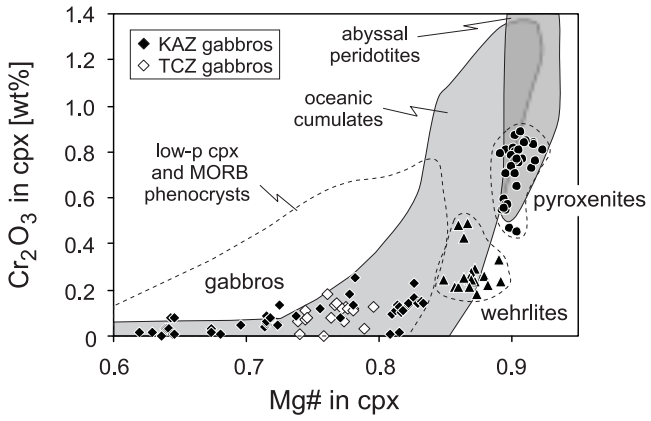

Fig. 4 Cr_2O_3 vs. Mg# in clinopyroxene of ultramafic rocks and gabbros. Each point represents a mineral average. Also shown are cpx compositions in abyssal peridotites, oceanic cumulates (Elthon et al., 1992) and low pressure cpx from experiments and MORB phenocrysts (Elthon, 1987).

4.3.5 Clinopyroxene compositions

Clinopyroxenes in wehrlites and pyroxenites are diopsides with Mg# between 0.87 and 0.88 in wehrlites, and between 0.90 and 0.91 in pyroxenites (Tab. 2). Gabbro clinopyroxenes are Ca-rich augites with Mg# between 0.64 and 0.82. Na_2O in wehrlite cpx is low (0.04 % - 0.05%, respectively) and significantly higher in pyroxenite cpx (0.12 % - 0.18 %; Tab. 2, Fig. 3). In gabbro cpx, Na_2O is between 0.17 % and 0.46 % (Tab. 2, Fig. 3). The average Cr_2O_3 content in wehrlite cpx (~ 0.28 %)

is lower than in pyroxenite cpx (0.55 % - 0.80 %, Tab. 2, Fig. 4), whereas Cr_2O_3 in gabbro cpx is variable between 0.01 % and 0.13 %.

Trace element compositions of clinopyroxenes from two pyroxenites and two wehrlites are given in Tab. 3 and shown in Fig. 5. Incompatible trace element abundances are lower than in clinopyroxene from ultramafic cumulates from the supra-subduction zone Troodos ophiolite in Cyprus (Batanova et al., 1996), but are comparable to concentrations in clinopyroxenes from residual abyssal peridotites (Hellebrand et al., submitted). Light rare-earth elements (LREE) are strongly depleted relative to chondrite and relative to middle and heavy-(H)REE (Fig. 5a) with chondrite-normalized $(La/Yb)_c$ = 0.034 - 0.042, $(La/Sm)_c$ = 0.071 - 0.100 and $(Gd/Yb)_c$ = 0.69 - 0.70. All four samples have negative Zr anomalies (Zr/Sm = 2.6 - 4.0), and positive Sr anomalies (Sr/Nd = 15 - 44; Fig. 5b). Troodos ultramafic cumulates also have negative Zr anomalies (Zr/Sm = 4.3 - 8.0), but positive Sr anomalies are absent and Sr/Nd is significantly lower (Sr/Nd = 6.5 - 18).

Table 3: Representative average trace element concentrations (µg/g) in clinopyroxene[1)]

	Agardagh				**Tes-Chem**			
Sample	T97A1		T97A50		T97A28		T97A30	
Type	Pyroxenite	σ (%)	Pyroxenite	σ (%)	Wehrlite	σ (%)	Wehrlite	σ (%)
Ti	444	22	441	14	471	3	697	6
V	123	10	133	15	161	2	197	5
Cr	4316	4	2998	38	2020	2	2449	40
Sr	3.6	8	3.8	3	4.6	9	5.0	6
Y	2.8	10	2.3	5	1.3	5	1.6	7
Zr	0.60	21	0.53	8	0.23	3	0.33	17
Ba	0.16	47	0.16	35	0.04	91	0.13	52
La	0.02	13	0.02	13	0.01	8	0.02	42
Ce	0.13	10	0.10	17	0.06	3	0.11	26
Nd	0.25	31	0.19	25	0.10	18	0.12	2
Sm	0.15	13	0.16	17	0.09	19	0.10	21
Eu	0.06	20	0.07	22	0.05	6	0.06	16
Gd	0.33	12	0.31	20	0.17	14	0.18	10
Dy	0.48	12	0.44	11	0.27	12	0.31	4
Er	0.35	11	0.29	17	0.18	10	0.24	11
Yb	0.38	8	0.36	7	0.20	4	0.22	6

[1)] Three to five spots on at least two grains were measured per sample

4.3.6 Hornblende compositions

Green hornblende is common in nearly all gabbros and is a magnesian-rich calcic amphibole (magnesio-hornblende after IMA classification; Leake 1978). Na_2O, K_2O and TiO_2 abundances are low with Na_2O = 0.64 % - 1.54 %, K_2O = 0.05 % - 0.31 %, and TiO_2 = 0.24 % - 1.52 %; Tab. 2). Mg# varies between 0.47 and 0.79 and is well correlated with Na_2O and Al_2O_3. Total Al (Al^T) varies between 0.81 and 1.81, indicating intermediate to low pressures of crystallization (Hammarstrom & Zen, 1986). Low Ti contents also suggest low temperatures of hornblende formation (Helz 1973; Otten 1984).

4.3.7 Plagioclase compositions

All ultramafic rocks are plagioclase-free. In gabbroic rocks plagioclase spans a compositional range from An_{67} to An_{92}. These An-contents are at the upper end of the range defined by oceanic cumulates (An_{28} - An_{95}; Elthon et al., 1992; Bloomer et al., 1989) and are comparable to mantle-transition zone and lower crustal gabbros from the Oman ophiolite (An_{82} - An_{91}; unpublished data and Korenaga & Kelemen, 1997). Highly calcic plagioclase is also a common feature in supra-subduction zone ophiolites (Bloomer et al., 1995).

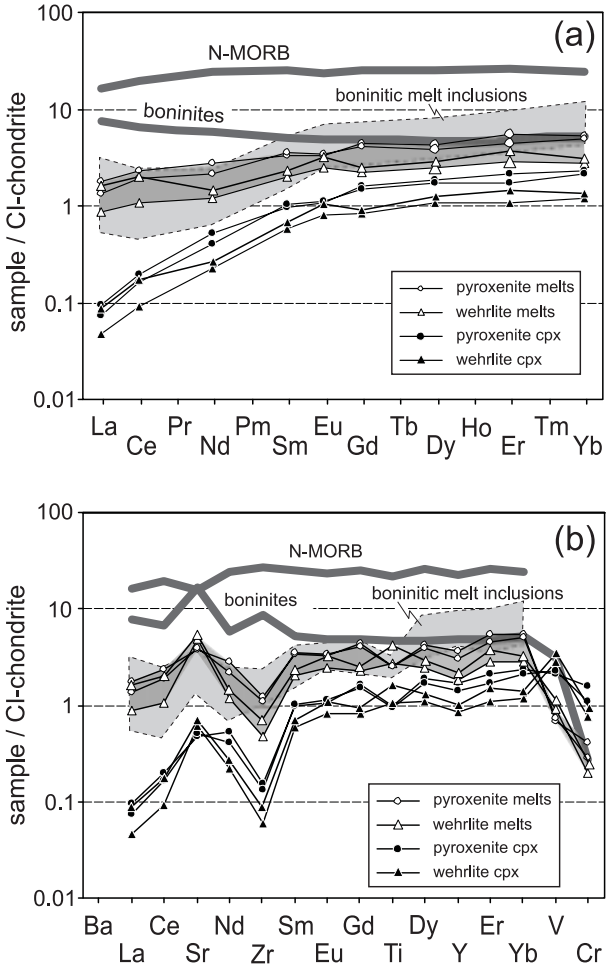

Fig. 5 Chondrite-normalized clinopyroxene compositions of ultramafic cumulates and corresponding equilibrium melts (dark grey fields, partition coefficients from Bédard, 1994). Also shown is the N-MORB composition of Hofmann (1988) and the average composition of boninites (see text; boninite data from Pearce et al., 1992 and Hickey & Frey, 1982). The light grey field gives the composition of boninitic melt inclusions from the Troodos ophiolite and represents primary boninitic magma compositions (data from Portnyagin et al., 1996). Note similarity to pyroxenite and wehrlite equilibrium melts, especially concerning the positive Sr anomaly.

4.4 Geochemistry

4.4.1 Major elements

Whole rock major element compositions of ultramafic and gabbroic rocks are given in Tab. 4. Mg# in ultramafic rocks is 0.94 for harzburgites and 0.90 - 0.85 for pyroxenites and wehrlites. MgO is highest in harzburgites (~ 49 %) and decreases from wehrlites (25.9 % and 30.0 %) to pyroxenites (20.2 % - 24.2 %). TiO_2 abundances are generally low (< 0.09 %) and close to detection limit. Whole rock Al/Si is low and Mg/Si is high in harzburgites (around 0.01 and 1.5, respectively) indicating a highly refractory character (Fig. 6).

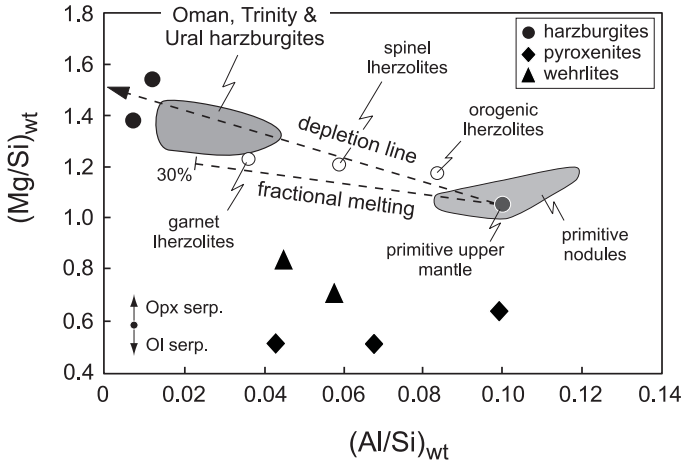

Fig. 6 $(Mg/Si)_{wt}$ vs. $(Al/Si)_{wt}$ for harzburgites, wehrlites and pyroxenites. The harzburgites are highly refractory and more depleted than harzburgites from several other ophiolites (data for Oman, Trinity and Ural harzburgites from Quick, 1981, and Sharma et al., 1995). The depletion line is the "terrestrial fractionation trend" of Jagoutz et al. (1979), the fractional melting line gives the residual composition after melting (Sharma et al., 1995). Also shown is the range for primitive nodules (Jagoutz et al., 1979) as well as average compositions of primitive upper mantle and orogenic lherzolites (Hart & Zindler, 1986), spinel lherzolites (McDonough, 1990) and garnet lherzolites (Jordan, 1978).

For gabbroic rocks, Mg# is between 0.80 - 0.42 (except plagiogranite: 0.29). MgO varies in a wide range between 1.8 % and 14.6 % (except plagiogranite: 0.25%; Tab. 4) and is negatively correlated with Na_2O (0.2 % - 2.2 %; Fig. 7a), Al_2O_3 (5.6 % - 29.4 %; Fig. 7b) and TiO_2 (0.05 % - 0.79 %). TiO_2 concentrations are generally low compared to many other ophiolite gabbros (see for example MacLeod & Yaouancq, 2000; Barnes et al., 1995; Gruau et al., 1995; Zimmer et al., 1995). CaO/Al_2O_3 decreases with decreasing MgO (Fig. 7c), primarily indicating decreasing ratios of modal clinopyroxene/plagioclase.

4.4.2 Trace elements

Ni in harzburgites is about 2100 µg/g and 2400 µg/g, for wehrlites and pyroxenites between 270 µg/g and 488 µg/g, and significantly lower for gabbros between 88 µg/g and 6 µg/g (Tab. 4, Fig. 7d, Fig. 8). Cr concentrations are highest in pyroxenites (4430 µg/g - 3273 µg/g) and lower in harzburgites (2494 µg/g and 1920 µg/g, respectively) and wehrlites (1941 µg/g and 941 µg/g, respectively). Cr concentrations in gabbros vary between 1228 µg/g and 13 µg/g (except plagiogranite; Tab. 4, Fig. 7).

Table 4: Major element (wt%, LOI corrected) and trace element (µg/g) composition of gabbros from the Agardagh Tes-Chem ophiolite. FeO* was calculated treating all iron as FeO and assuming that $FeO/(FeO+Fe_2O_3) = 0.85$

	ADZ	**Karachat zone: gabbroic rocks**										
	5621 *pg*	T97A35 *gn*	T97A36 *hbl-ga*	T97A54 *ol-ga*	T97A55 *ga*	T97A56 *hbl-ga*	T97A60 *gn*	T97A61 *gd*	T97A62 *gd*	T97A63 *di*	T97A64 *ga*	T97A66 *ga*
SiO_2	79.08	49.34	46.53	45.79	45.22	45.59	49.89	53.58	54.25	58.70	45.94	45.22
TiO_2	0.04	0.15	0.30	0.11	0.08	0.79	0.38	0.66	0.51	0.36	0.13	0.05
Al_2O_3	12.75	10.88	19.95	15.41	29.44	19.92	17.66	17.67	14.89	16.54	20.26	27.24
Fe_2O_3	1.41	15.07	11.36	8.69	2.64	14.61	12.23	11.84	10.62	7.63	6.88	4.11
MnO	0.03	0.30	0.20	0.14	0.07	0.24	0.22	0.22	0.19	0.13	0.13	0.08
MgO	0.25	12.65	7.01	14.52	1.78	4.45	6.07	3.64	7.61	4.48	9.38	4.75
CaO	0.48	11.41	13.75	14.76	20.69	13.03	11.70	10.63	10.32	9.80	16.86	18.47
Na_2O	6.54	0.36	0.80	0.21	0.27	1.13	1.07	1.65	1.48	2.15	0.51	0.14
K_2O	0.36	0.01	0.02	0.07	0.04	0.03	0.03	0.03	0.19	0.19	0.02	0.00
P_2O_5	0.02	0.00	0.00	0.00	0.00	0.01	0.00	0.04	0.04	0.04	0.00	0.00
Cr_2O_3	0.00	0.02	0.01	0.05	0.01	0.00	0.01	0.00	0.05	0.02	0.04	0.04
NiO	0.00	0.01	0.00	0.01	0.00	0.00	0.00	0.00	0.01	0.00	0.00	0.00
LOI	0.74	0.42	1.56	3.23	2.56	0.84	0.65	0.50	1.35	1.97	3.08	3.85
Total	101.0	100.2	99.94	99.77	100.2	99.80	99.25	99.96	100.2	100.0	100.2	100.1
FeO*	1.08	11.53	8.69	6.65	2.02	11.17	9.35	9.06	8.12	5.84	5.26	3.14
Mg#	0.29	0.66	0.59	0.80	0.61	0.42	0.54	0.42	0.63	0.58	0.76	0.73
Sc	13	80	60	52	29	63	57	51	71	48	56	32
V	1	190	411	143	69	356	329	240	211	219	140	85
Cr		175	58	371	87	18	44	18	381	193	313	420
Co	2	58	39	61	7	36	38	28	39	25	40	26
Ni	5	51	19	88	9	8	16	6	66	18	35	38
Cu		31	121	142	5	83	35	45	2	35	6	3
Zn		117	73	43	14	120	94	114	91	72	48	27
Ga		10	16	8	15	22	17	18	13	14	11	13
Rb	4	2	2	2		2		2	3	3	2	2
Sr	27	65	110	67	163	149	119	147	105	97	96	130
Ba	155	25	16	22	18	15	23	26	53	78	18	19
Y		4.41		1.83	1.46	4.90	4.09		23.0	12.7		0.66
Zr		1.29		1.34	0.89	2.13	1.68		18.9	18.2		0.36
Nb		0.021		0.021	0.014	0.065	0.030		0.408	0.407		0.007
U		0.004		0.003	--	0.010	0.007		0.037	0.038		0.003
Th		0.008		0.004	--	0.014	0.044		0.043	0.061		0.124
Pb		0.450		0.395	0.585	0.750	0.882		2.87	2.21		0.671
La	3.97	0.25		0.32	0.64	0.45	0.43		1.32	1.30		
Ce	8.69	0.61		0.58	0.65	0.95	0.79		5.20	4.25		
Pr		0.10		0.08	0.07	0.15	0.10		0.86	0.68		
Nd	3.54	0.58		0.30	0.50	0.86	0.59		5.32	4.50		
Sm	0.90	0.33		0.14	0.20	0.40	0.28		2.27	1.61		
Eu	0.10	0.13		0.08	0.09	0.25	0.17		0.65	0.31		
Gd	1.04	0.48		0.24	0.28	0.57	0.43		3.63	1.84		
Dy	1.70	--		--	--	--	--		--	--		
Ho		0.23		0.11	0.08	0.22	0.19		1.03	0.56		
Er	1.62	--		--	--	--	--		--	--		
Yb	2.30	0.80		0.23	0.19	0.64	0.54		3.81	1.67		
Lu		0.09		0.04	0.03	0.09	0.06		0.39	0.22		

ADZ = Agardagh zone, hzb = harzburgite, wht = wehrlite, pyx = pyroxenite, ga = gabbro, ol-ga = olivine-gabbro, hbl-ga = hornblende-gabbro, gn = gabbronorite, no = norite, gd = gabbrodiorite, di = diorite, pg = plagiogranite. Sm and Nd by TIMS, all other trace elements by MIC-SSMS except Rb, Sr, Ba, Sc, V, Cr, Co, Ni, Cu, Zn and Ga by XRF.

Table 4: continued

	Tes Chem zone: gabbroic rocks						**Agardagh and Karachat zones: Ultramafic rocks**						
	T97T22 *ga*	T97T23 *ga*	T97T27a *no*	T97T27b *hbl-ga*	T97T28 *hbl-ga*	T97T29 *hbl-ga*	T97A1 *pyx*	T97A15 *hzb*	T97A17 *hzb*	T97A48 *pyx*	T97A50 *pyx*	T97A28 *wht*	T97A30 *wht*
SiO_2	44.65	48.38	48.04	50.97	47.67	49.56	51.57	41.78	44.95	49.04	51.12	46.80	48.01
TiO_2	0.48	0.09	0.09	0.34	0.08	0.12	0.07	0.01	0.01	0.07	0.08	0.07	0.09
Al_2O_3	17.60	16.81	25.24	5.63	20.71	19.65	1.96	0.44	0.27	4.29	3.05	1.86	2.45
Fe_2O_3	15.37	8.04	5.72	10.34	6.47	6.53	5.33	7.87	6.85	7.07	6.14	11.31	10.37
MnO	0.23	0.16	0.10	0.21	0.12	0.13	0.13	0.36	0.07	0.12	0.11	0.15	0.16
MgO	6.83	9.73	5.84	14.58	9.16	7.99	20.34	49.93	48.05	24.17	20.22	30.04	25.86
CaO	12.68	15.15	13.34	17.11	14.80	13.45	20.40	0.13	0.06	15.58	19.46	10.59	13.57
Na_2O	0.68	0.33	1.39	0.46	0.66	0.90	0.11	0.04	0.00	0.09	0.10	0.01	0.06
K_2O	0.08	0.04	0.06	0.04	0.09	0.19	0.00	0.00	0.00	0.00	0.01	0.00	0.00
P_2O_5	0.00	0.00	0.01	0.01	0.00	0.01	0.00	0.00	0.00	0.00	0.00	0.00	0.00
Cr_2O_3	0.01	0.02	0.01	0.16	0.04	0.03	0.58	0.36	0.44	0.49	0.44	0.13	0.26
NiO	0.00	0.01	0.00	0.01	0.01	0.01	0.04	0.39	0.41	0.07	0.04	0.04	0.04
LOI	0.25	1.05	1.34	1.22	1.66	0.00	2.25	20.81	16.39	4.76	2.53	6.60	4.82
Total	98.62	98.77	99.85	99.86	99.82	98.56	100.5	101.3	101.1	101.0	100.8	101.0	100.9
FeO*	11.76	6.15	4.37	7.91	4.95	4.99	4.08	6.02	5.24	5.41	4.70	8.65	7.93
Mg#	0.51	0.74	0.70	0.77	0.77	0.74	0.90	0.94	0.94	0.89	0.88	0.86	0.85
Sc	79	61	24	115	45	47	61	n.d.	n.d.	50	71	53	70
V	567	167	70	389	113	129	168	18	12	132	172	144	180
Cr	13	165	125	1228	308	197	4430	1921	2494	3671	3273	941	1941
Co	49	45	28	46	34	30	43	123	124	68	50	109	87
Ni	11	67	31	86	61	51	285	2122	2437	488	282	274	270
Cu	8	299	25	73	8	70	41	2	4	n.d.			
Zn	85	44	44	60	37	40	68	31	28	28	26	35	37
Ga	16	11	16	8	13	12	5	3	3	5	6	4	5
Rb	4		2	2	2	5							
Sr	142	105	167	33	117	130							
Ba	25	20	43	20	34	76							
Y	3.74		0.85	7.27	0.98	3.15							
Zr	1.66		1.72	3.05	0.54	6.03							
Nb	0.063		0.051	0.045	0.008	0.122							
U	0.015		0.028	0.022	0.002	0.037							
Th	0.059		0.091	0.105	0.051	0.088							
Pb	1.57		0.788	2.33	0.585	1.39							
La	0.37		0.46	0.29	0.55	0.65							
Ce	0.71		0.80	1.10	0.64	1.74							
Pr	0.10		0.08	0.19	0.08	0.24							
Nd	0.51		0.38	1.15	0.20	1.31							
Sm	0.26		0.10	0.58	0.09	0.40							
Eu	0.13		0.12	0.24	0.10	0.23							
Gd	0.45		0.13	0.97	0.21	0.57							
Dy	--		--	--	--	--							
Ho	0.18		0.03	0.30	0.08	0.13							
Er	--		--	--	--	--							
Yb	0.45		0.13	0.83	0.19	0.33							
Lu	0.07		0.02	0.12	0.03	0.05							

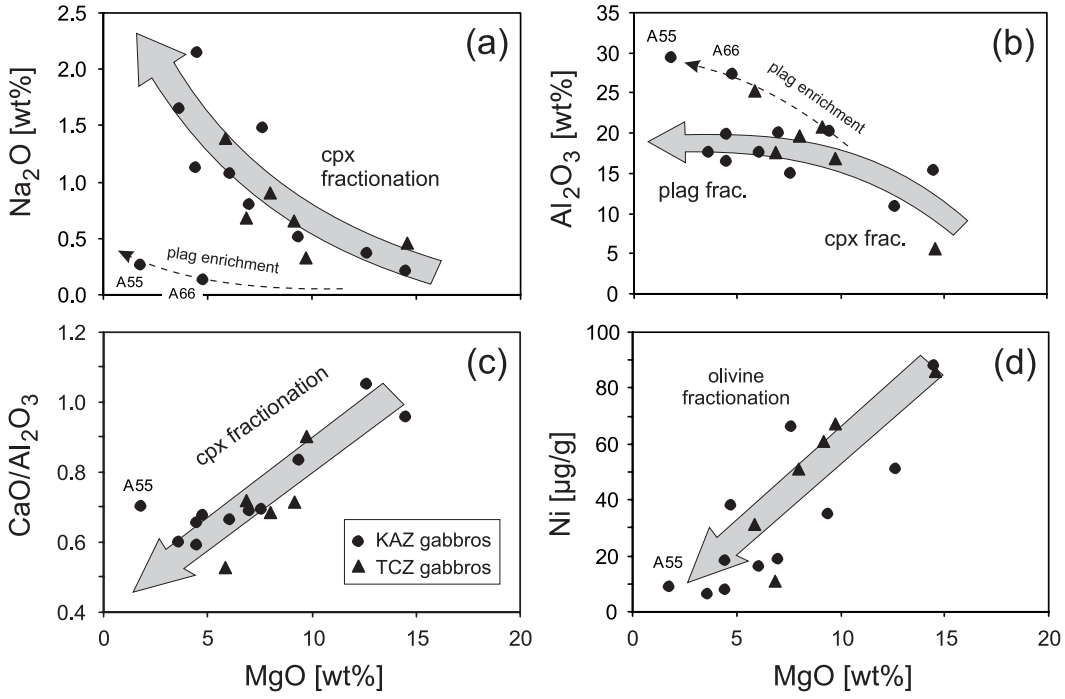

Fig. 7 Major element data of gabbroic rocks. Note that major elements, although principally consistent with olivine - cpx - plag fractionation, primarily reflect modal compositions.

Primitive mantle-normalized trace element abundances for KAZ and TCZ gabbros are shown in Fig. 9. No differences in absolute concentrations exist between the two units. In general, abundances of incompatible trace elements in ATCO gabbros are somewhat lower than in gabbros from the Oman ophiolite (MacLeod & Yaouancq, 2000; Fig. 9), but are comparable to gabbros from the Gabal Gerf ophiolite in the Nubian Shield of NE Africa (Zimmer et al., 1995; Fig. 9). Both ophiolites have been proposed to represent „true“ mid-ocean ridge-like oceanic crust. Differences to Oman and Gabal Gerf gabbros exist in high-field strength element (HFSE) abundances, especially in Nb and Zr, which are significantly depleted in ATCO gabbros forming strongly negative anomalies (Fig. 9). Ti anomalies are variable for different ATCO samples, reflecting different amounts of modal

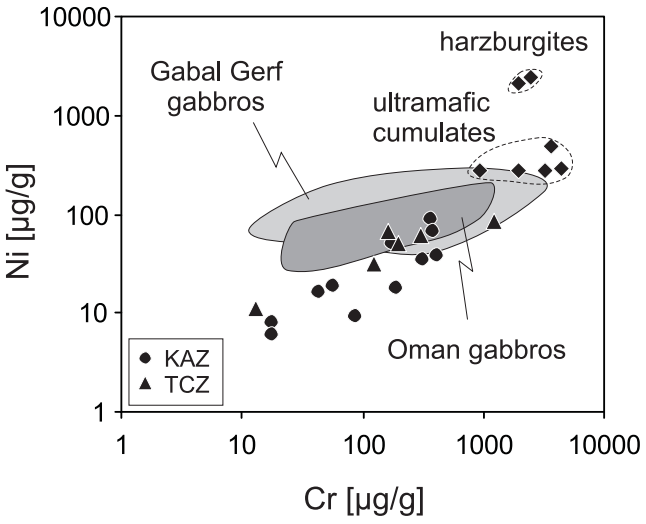

Fig. 8 Ni vs. Cr concentration in ATCO ultramafic and gabbroic rocks. Also shown are gabbros from the Gabal Gerf (Zimmer et al., 1995) and the Oman ophiolite (MacLeod & Yaouancq, 2000).

ilmenite. Primitive mantle-normalized $(Th/La)_n$ ratios in KAZ gabbros (0.1 - 0.8) are lower than in TCZ gabbros (0.7 - 2.8; Fig. 13) whereas no significant differences exist in $(Nb/La)_n$ ratios (0.02 - 0.31 and 0.01 - 0.19, respectively). $(Nb/La)_n$ ratios are generally low indicating a strong depletion of Nb with respect to the LREE. Sr is enriched in all gabbroic rocks with $(Sr/Nd)_n$ ratios between 1.3 and 21 for KAZ gabbros, and between 1.9 and 39 in TCZ gabbros. However, the variation in Sr/Nd ratios primarily reflects variable abundances of modal plagioclase within the samples, as Sr is predominantly partitioned into plagioclase. We therefore normalized the Sr concentration of a sample to the abundance of modal plagioclase in this sample by dividing the Sr concentration by the whole-rock Al_2O_3 content ($[Sr]_{Al}$ = µg/g Sr / wt% Al_2O_3), which is a good approximation for the amount of modal plagioclase in a sample. The resulting $[Sr]_{Al}$-values are dimensionless but comparable numbers, representing Sr concentrations arbitrarily normalized to 1% Al_2O_3. From the normalized Sr concentrations, we calculated $[Sr]_{Al}$/Nd ratios to express *variations* in Sr anomalies caused by other processes than by variable amounts of modal plagioclase. Doing this, $[Sr]_{Al}$/Nd ratios are still variable in ATCO gabbros, with lower values for KAZ gabbros ($[Sr]_{Al}$/Nd = 1.3 - 13.5) than for TCZ gabbros ($[Sr]_{Al}$/Nd = 5.1 - 28.5). Large-ion lithophile elements (LILE) are enriched in ATCO gabbros as indicated by high $(Ba/La)_n$ ratios (3.4 - 10 in KAZ gabbros and 6.3 - 12 in TCZ gabbros).

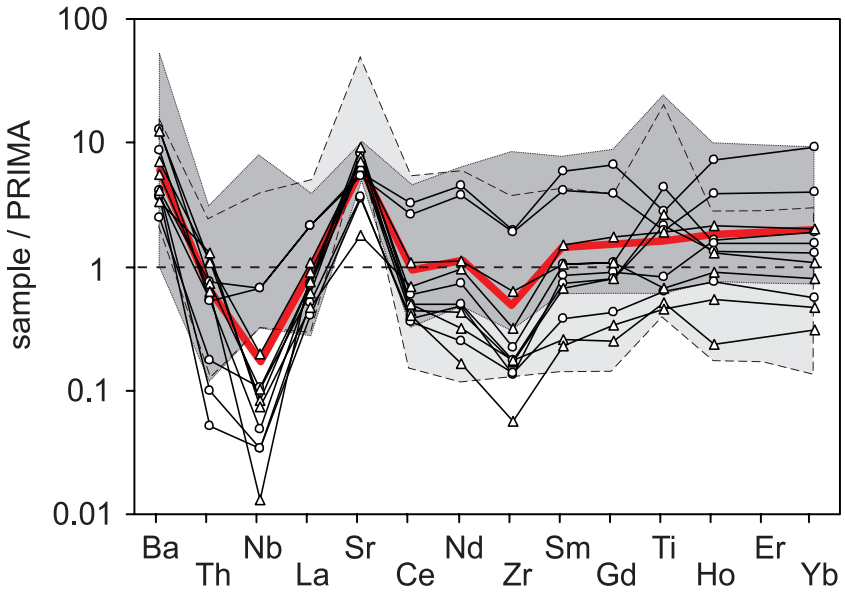

Fig. 9 Primitive mantle (PRIMA; Hofmann, 1988) normalized trace element abundances of KAZ (circles) and TCZ gabbros (triangles). No differences exist between the two groups. All samples are characterized by negative Th, Nb and Zr anomalies. Ti is variable due to variable amounts of ilmenite. Sr is enriched in all samples, resulting in strongly positive anomalies. Dark grey field: Layered and massive gabbros from the Oman ophiolite; light grey field: Gabbros from the Gabal Gerf ophiolite (data sources: MacLeod & Yaouancq, 2000; Zimmer et al., 1995). Thick line: average concentration of all samples.

4.4.3 Rare earth elements

Rare earth elements (REE) are variably depleted in all gabbroic rocks relative to N-MORB and compared to varitextured gabbros from the Oman ophiolite (Fig. 10). KAZ gabbros comprise LREE depleted but U-shaped samples having positive Eu-anomalies and chondrite-normalized $(La/Yb)_c$ = 0.50 - 0.98, $(La/Sm)_c$ = 0.72 - 1.41 and $(Sm/Yb)_c$ = 0.59 - 0.70. These samples are similar or even more depleted than layered gabbros from the Oman ophiolite (Fig. 10a). Two other samples have higher abundances of REE and negative Eu-anomalies, but are also depleted in LREE with $(La/Yb)_c$ = 0.25 - 0.56, $(La/Sm)_c$ = 0.38 - 0.52, and $(Sm/Yb)_c$ = 0.66 - 1.07. These two gabbros resemble varitextured gabbros from the Oman ophiolite (Fig. 10a). TCZ gabbros tend to be either LREE depleted (Fig. 10b) with $(La/Yb)_c$ = 0.25 - 0.60, and $(Sm/Yb)_c$ = 0.65 - 0.78, or LREE enriched (Fig. 10c) with $(La/Yb)_c$ = 1.41 and 2.63, and $(Sm/Yb)_c$ = 0.88 - 1.34. Enrichment in La and Ce relative to Nd and Sm is also observed in some TCZ gabbros resulting in a large range of $(La/Sm)_c$ between 0.32 - 2.98. Eu-anomalies are absent in the LREE depleted samples (Fig. 10b), and positive in the LREE enriched samples (Fig. 10c). Generally, all TCZ gabbros resemble the more depleted KAZ gabbros and layered gabbros from Oman (Fig. 10), with one sample (T27a) being more depleted.

4.4.4 Isotopic compositions

Sr and Nd isotopic compositions and initial ϵ_{Nd} values calculated for an age of 570 Ma are given in Tab. 5. Initial ϵ_{Nd} values are +5.8 to +7.1 for

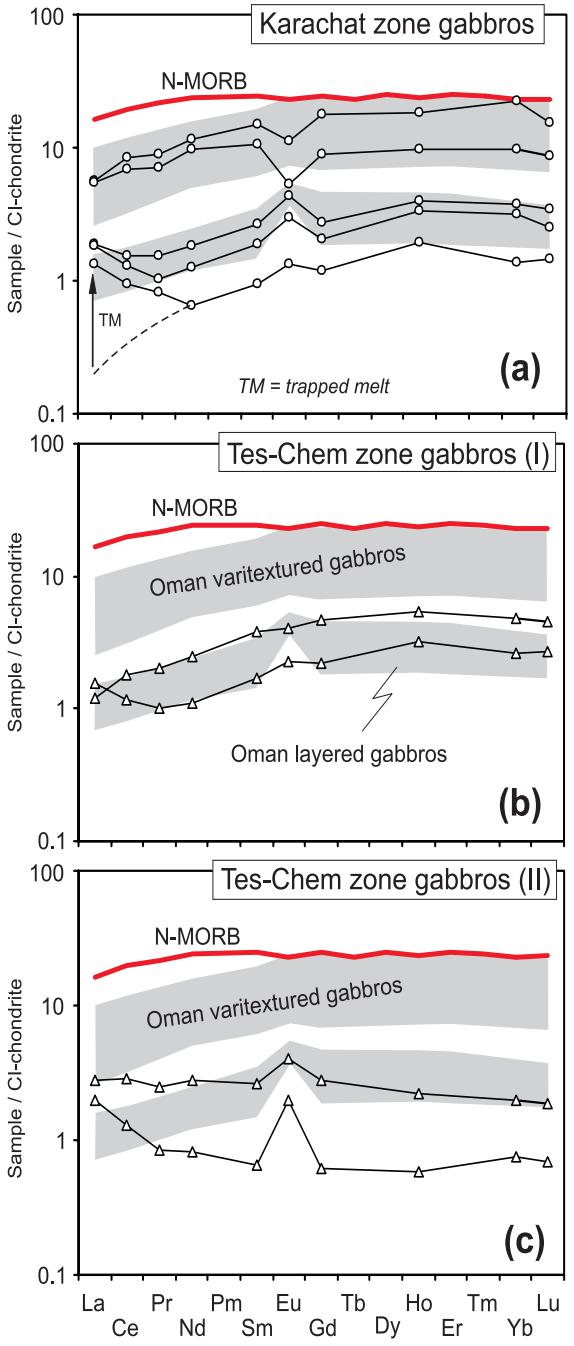

Fig. 10 Chondrite-normalized rare earth element abundances of gabbroic rocks. (a) KAZ gabbros have LREE-depleted patterns with variable Eu anomalies. Some samples have U-shaped LREE patterns with enrichment of La and Ce relativ to Nd. (b) LREE-depleted TCZ gabbros are very similar to KAZ gabbros but Eu anomalies are nearly absent. (c) LREE-enriched TCZ gabbros with positive Eu anomalies due to high modal plag. Thick line: N-MORB composition from Hofmann (1988), grey fields: compositional range of Oman gabbros (data from MacLeod & Yaouancq, 2000), upper fields: varitextured gabbros, lower fields: layered gabbros.

KAZ gabbros, +4.8 to +6.2 for TCZ gabbros and +6.3 for the plagiogranite sample. Except for two samples (A62 & A63), all KAZ gabbros, two TCZ gabbros and the plagiogranite have identical ϵ_{Nd} values within error (+5.6 to +6.3) and fit an isochron in terms of $^{143}Nd/^{144}Nd$ vs. $^{147}Sm/^{144}Nd$ with an age of 546 ± 18 Ma (Fig. 11), and an initial ϵ_{Nd} value of +6.2 ± 0.6. However, three spatially related TCZ gabbros have slightly lower initial ϵ_{Nd} values (+4.8 to + 5.2) and plot below the isochron. Calculating an age from the linear correlation of these samples yields an identical age of 553 ± 28 Ma, but a lower initial ϵ_{Nd} value of +5.1 ± 0.9.

Pb isotopic compositions of selected whole rocks and plagioclase separates are given in Tab. 6 and are shown in Fig. 12. Whole rock $^{206}Pb/^{204}Pb$ ratios vary between 17.855 and 18.089, $^{207}Pb/^{204}Pb$ ratios between 15.530 and 15.576, and $^{208}Pb/^{204}Pb$ ratios between 37.590 and 37.720 (except plagiogranite: $^{206}Pb/^{204}Pb$ = 18.452, $^{207}Pb/^{204}Pb$ = 15.554, $^{208}Pb/^{204}Pb$ = 37.810). Pb isotopic variations in plagioclase separates are *higher* than in whole rocks, with $^{206}Pb/^{204}Pb$ ratios between 17.854 and 18.282, $^{207}Pb/^{204}Pb$ ratios between 15.586 and 15.665, and $^{208}Pb/^{204}Pb$ ratios between 37.693 - 38.246 (except plagiogranite: $^{206}Pb/^{204}Pb$ = 18.231, $^{207}Pb/^{204}Pb$ =15.543, $^{208}Pb/^{204}Pb$ = 37.693).

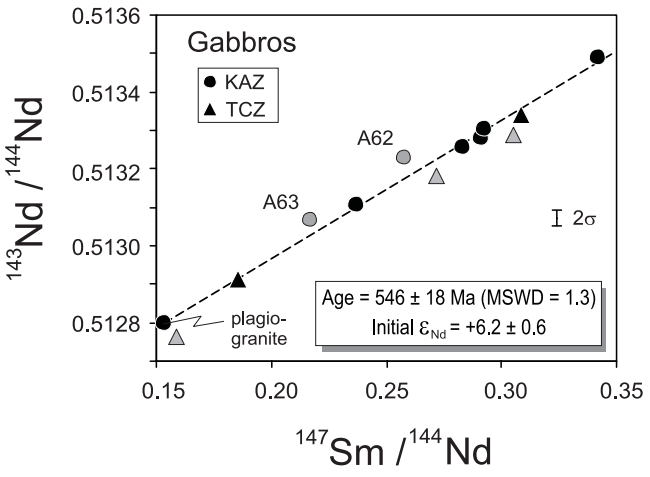

Fig. 11 Sm-Nd isotopic data of Karachat and Tes-Chem zone gabbros. Most samples fit an isochron corresponding to an age of 546 ± 18 Ma. The more evolved gabbros A62 and A63 plot above the isochron, and three TCZ gabbros plot below the isochron due to slightly different initial $^{143}Nd/^{144}Nd$ ratios. Grey points are excluded from regression.

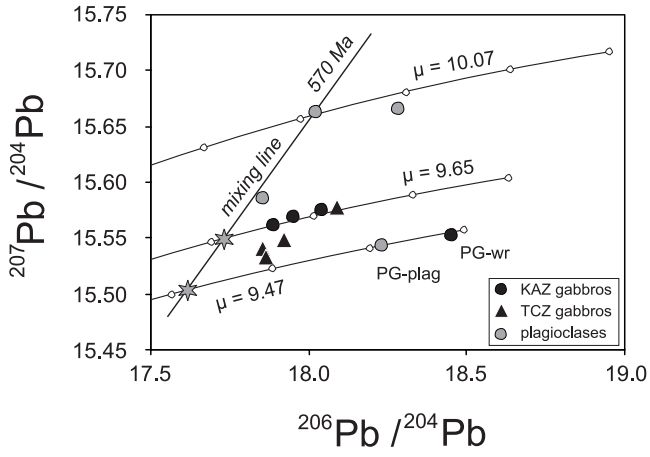

Fig. 12 Pb isotopic composition of selected whole rock samples and plagioclase separates. Also shown are three Pb evolution lines calculated by assuming a two-stage model according to Stacey & Kramers (1975) but varying the second stage μ-value to fit the data points. Stars: inferred starting compositions of KAZ and TCZ gabbroic rocks, produced by mixing of an unradiogenic, mantle-derived component and a more radiogenic, possibly slab-derived component. Tick distance: 200 Ma.

Table 5: Sr and Sm-Nd data for gabbroic rocks

Sample	Type	Sr (µg/g)	$(^{87}Sr/^{86}Sr)_m$	Sm (µg/g)	Nd (µg/g)	$^{147}Sm/^{144}Nd$	$(^{143}Nd/^{144}Nd)_m$	$(^{143}Nd/^{144}Nd)_i$	$(\varepsilon_{Nd})_i$
5621	pg			0.896	3.535	0.1531	0.512800 ± 9	0.512228	6.3
T97A35	hbl-ga	67.03	0.703674 ± 16	0.328	0.580	0.3419	0.513489 ± 9	0.512212	6.0
T97A54	ol-ga	87.35	0.703769 ± 10	0.145	0.301	0.2910	0.513278 ± 15	0.512192	5.6
T97A55	ga	171.3	0.703581 ± 12	0.196	0.499	0.2371	0.513108 ± 10	0.512223	6.2
T97A56	hbl-ga	141.6	0.703683 ± 11	0.402	0.859	0.2830	0.513256 ± 7	0.512199	5.8
T97A60	gn	122.1	0.703618 ± 13	0.284	0.588	0.2922	0.513302 ± 7	0.512211	6.0
T97A62	gd	101.2	0.704198 ± 12	2.268	5.316	0.2580	0.513230 ± 10	0.512267	7.1
T97A63	di	96.85	0.703975 ± 10	1.611	4.498	0.2166	0.513067 ± 8	0.512258	6.9
T97T22	ga	143.9	0.704091 ± 19	0.262	0.513	0.3087	0.513341 ± 11	0.512188	5.6
T97T27a	no	166.5	0.703376 ± 20	0.100	0.383	0.1588	0.512762 ± 13	0.512169	5.2
T97T27b	hbl-ga	31.82	0.704640 ± 12	0.580	1.150	0.3052	0.513288 ± 7	0.512149	4.8
T97T28	hbl-ga	139.0	0.703399 ± 15	0.089	0.198	0.2716	0.513181 ± 11	0.512167	5.1
T97T29	hbl-ga	134.7	0.704250 ± 12	0.402	1.308	0.1856	0.512914 ± 4	0.512221	6.2

m = measured ratios, i = initial ratios calculated for an age of 570 Ma. Error of the measured ratios is the in run precision, given as $2\sigma_m$ in the last two digits. The error of the ε_{Nd} values is ±0.4 based on the external reproducibility. pg = plagiogranite, hbl-ga = hornblende-gabbro, ol-ga = olivine-gabbro, ga = gabbro, gn = gabbronorite, gd = gabbrodiorite, di = diorite, no = norite

Table 6: Pb isotopic compositions for gabbroic rocks

Sample	Loc	Type	$^{206}Pb/^{204}Pb$	$^{207}Pb/^{204}Pb$	$^{208}Pb/^{204}Pb$	$^{207}Pb/^{206}Pb$
5621	ADZ	pg (wr)	18.4521 ± 0.0013	15.5535 ± 0.0015	37.8100 ± 0.0046	0.842913 ± 0.000024
5621	ADZ	pg (plag)	18.2311 ± 0.0014	15.5428 ± 0.0017	37.6773 ± 0.0054	0.852544 ± 0.000031
T97A35	KAZ	hbl-ga (plag)	18.2820 ± 0.0036	15.6654 ± 0.0046	37.9430 ± 0.0148	0.856883 ± 0.000085
T97A54	KAZ	ol-ga (plag)	18.0221 ± 0.0013	15.6622 ± 0.0015	38.2458 ± 0.0047	0.869058 ± 0.000026
T97A55	KAZ	ga (plag)	17.8543 ± 0.0031	15.5862 ± 0.0040	37.6931 ± 0.0128	0.872962 ± 0.000075
T97A62-1	KAZ	gd (wr)	17.8871 ± 0.0019	15.5615 ± 0.0018	37.6590 ± 0.0050	0.870000 ± 0.000024
T97A63-1	KAZ	di (wr)	18.0359 ± 0.0012	15.5757 ± 0.0014	37.7017 ± 0.0043	0.863595 ± 0.000024
T97A63-2	KAZ	di (wr)	17.9478 ± 0.0007	15.5701 ± 0.0008	37.6585 ± 0.0023	0.867528 ± 0.000013
T97T22	TCZ	ga (wr)	17.8552 ± 0.0007	15.5374 ± 0.0008	37.5901 ± 0.0024	0.870196 ± 0.000014
T97T27a	TCZ	no (wr)	18.0894 ± 0.0017	15.5746 ± 0.0017	37.7199 ± 0.0048	0.860989 ± 0.000024
T97T27b	TCZ	hbl-ga (wr)	17.8653 ± 0.0007	15.5304 ± 0.0009	37.6080 ± 0.0027	0.869306 ± 0.000016
T97T29	TCZ	hbl-ga (wr)	17.9222 ± 0.0009	15.5454 ± 0.0012	37.6385 ± 0.0035	0.867387 ± 0.000020

pg = plagiogranite, hbl-ga = hornblende-gabbro, ol-ga = olivine-gabbro, ga = gabbro, gd = gabbrodiorite, di = diorite, no = norite, wr = whole rock, pl = plagioclase. Errors given are in run precisions ($2\sigma_m$), calculated from the spiked and unspiked run for each sample (details see text)

4.5 Discussion

4.5.1 Origin of ultramafic rocks

A general question concerning the ultramafic rocks of the ATCO is whether they are residual mantle rocks or cumulates derived from cooling and fractionating mafic liquids. Although it is most likely from petrographic and field relationships that the wehrlites and pyroxenites are ultramafic cumulates, this is difficult to assess for dunites and harzburgites.

4.5.1.1 Dunites and harzburgites

A residual origin for dunites and harzburgites is suggested by high Cr# and very low TiO_2 in dunite and harzburgite spinels (Cr# = 0.74 - 0.83; Fig. 2, except sample A21). However, high Cr# in spinel is also observed in layered intrusions and ultramafic cumulates (Irvine 1967, 1977; Dick & Bullen, 1984), boninites (Bloomer, 1983) and high-magnesian andesites (Straub et al., 2001), and is therefore not reliable in discriminating between ultramafic cumulates and residual mantle rocks. On the other hand, high Cr# in spinel indicates a refractory melt and thus a refractory mantle source, independent of whether the spinel is regarded as cumulate or residual phase. Compared to other dunites, dunite sample A21 has a significantly lower Cr# in spinel (0.59). Additionally, this sample is undeformed and was taken from the eastern part of the ATCO, closely related to pyroxenite and wehrlite occurrences. In contrast, all other dunite samples are strongly sheared with distinct lineations and are spatially related to harzburgites and serpentinites (Fig. 1). We therefore regard sample A21 as cumulate dunite, whereas other dunites and harzburgites are assumed to represent residual mantle rocks, possibly from the mantle-transition zone as observed in several other ophiolites (e.g. Oman ophiolite, Bay of Islands ophiolite; Boudier & Nicolas, 1995; Suhr & Robinson, 1994). As described by Kelemen et al. (1995, 1997), residual dunites in the mantle transition zone may result from opx dissolution from harzburgite by upwards migrating, opx undersaturated melts. We suggest this mechanism as having been responsible for the formation of the ATCO dunites, but underline that residual dunites usually contain small amounts of interstitial cpx or plag, which is absent in ATCO dunites.

Whole rock ratios of Al/Si and Mg/Si are sometimes used to infer the degree of depletion of residual mantle rocks (Jagoutz et al., 1979; Sharma et al., 1995). Whereas primitive upper mantle estimates for Al/Si and Mg/Si are ~ 0.1 and ~ 1.05 (Hart & Zindler, 1986), depleted mantle rocks tend to have higher Mg/Si ratios but lower Al/Si ratios, following a depletion line. This depletion line is shown in Fig. 6, together with Al/Si and Mg/Si ratios for harzburgites, wehrlites and pyroxenites. The harzburgites have extremely low Al/Si ratios (~ 0.01) and correspondingly high Mg/Si ratios (~ 1.4 - 1.6). This underlines their highly refractory character as derived from Cr# in spinel, and the degree of depletion exceeds the range infered for several other ophiolite

harzburgites (Fig. 6). Although serpentinization may shift whole rock compositions and thus Mg/Si ratios, Al/Si ratios are generally less affected (O'Hanley 1996; Fig. 6). Therefore, no significant shift along the depletion line is expected, although the harzburgites are highly serpentinized. In contrast to the harzburgites, wehrlites and pyroxenites plot away from the depletion line, most likely due to their origin as cumulates (Fig. 6).

4.5.1.2 Pyroxenites and wehrlites

Pyroxenites and wehrlites have significantly lower Fo contents (0.81 - 0.82) and Cr# in spinel (0.22 - 0.45, Fig. 2) than dunites, further underlining that they are cumulates. A cumulus origin for these rocks is also suggested by Cr and Mg# compositions of cpx, which plot within the range of oceanic cumulates as given by Elthon et al. (1992; Fig. 4). Regarding spinel compositions, dunite sample A21 as well as wehrlite A30 and pyroxenite A48 qualitatively follow an olivine/spinel fractionation trend with pyroxenite fractionation preceeding wehrlite formation (Fig. 2). This is also suggested by higher Cr and higher Mg# in pyroxenite cpx (Fig. 4). However, contrary to this, pyroxenite cpx also have higher sodium contents (Fig. 3) and higher concentrations of incompatible trace elements than wehrlite cpx (Fig. 5), making their formation from a common parental magma unlikely. Additionally, the range of Cr# in spinel is too large to be explained by fractionation of a single melt batch, and it is also unlikely that pyroxenite fractionation directly follows dunite fractionation from a single melt before wehrlite formation occurs. We therefore suggest that pyroxenites and wehrlites represent different batches of a primary melt emplaced within different levels of the island arc crust. This is underlined by field observations, where pyroxenites occur in the ADZ and are therefore closely related to residual mantle rocks, whereas the wehrlites belong to the KAZ and are associated with gabbroic rocks (Fig. 1). The occurrence of wehrlites associated with gabbros is a well known feature, and is observed, for example, in the Oman ophiolite, where the wehrlites intruded layered gabbros in the lower oceanic crust (Jousselin & Nicolas, 2000). In this case, the wehrlites have not originated as cumulates but represent tholeiitic melts squeezed out from the mantle below, dragging residual olivine as a mush. Therefore, these wehrlites are characterized by olivine compositions typically observed in mantle rocks (Fo ~ 0.90). Wehrlites and pyroxenite sills are also described for the supra-subduction zone Coast Range ophiolite in California (Shervais 2001). Here, they crosscut layered gabbros or build sill-like intrusions, and are therefore regarded as second stage melts from a mantle previously depleted to form melts from which the layered gabbros crystallized (Shervais 2001).

Wehrlites are also abundant in layered mafic intrusions, where they occur as sills and small intrusions, typically intruding gabbros (e.g. Kap Edward Holm Layered Series, KEHLS; Bernstein et al., 1996). In the KEHLS, the wehrlite cumulates represent hydrous high-MgO parental melts with cpx Mg# between 0.73 and 0.88 (0.87 - 0.88 in ATCO wehrlites) and olivine with Fo_{66} to Fo_{88}

(Bernstein et al., 1992). However, the KEHLS wehrlites are plagioclase- and hornblende-bearing (Bernstein et al., 1996), whereas these phases are absent in ATCO wehrlites, suggesting an even more refractory melt than, for example, derived for the KEHLS. In mafic intrusions developed from more evolved melts, such as the Skaergaard intrusion (e.g. McBirney, 1996), wehrlites are absent, underlining that their occurrence is closely related to refractory, MgO-rich melts. Whereas pyroxenites are not described for the KEHLS or the Skaergaard intrusion, they occur as layers between cumulus dunite and harzburgite in the Bushveld complex, which originated from SiO_2 and MgO-rich (~ 12.5 % MgO), but CaO-poor melts, resembling boninites (Cawthorn & Davies, 1983; Eales & Cawthorn, 1996). However, due to low abundances of CaO in primary magmas of the Bushveld complex, pyroxenites are generally Ca-poor orthophyroxenes, wheres the pyroxenites of the ATCO consist exclusively of clinopyroxene. Olivine from cumulus dunite and harzburgite of the most primitive, lower parts of the Bushveld complex (Lower and Critical Zones) have Fo between 0.77 and 0.90 (Eales & Cawthorn, 1996), and are therefore comparable to wehrlite and cumulate dunite A21 olivine compositions (between Fo_{81} - Fo_{91}). The ultramafic cumulates of the ATCO must therefore have crystallized from similar, highly refractory melts with high MgO contents ($\geq$12 %). This is consistent with a model proposed by Kelemen (1990), who pointed out that wehrlites may occur as crystallization products of tholeiitic melts enriched in MgO by reaction with mantle peridotite. Such reactions may especially occur in island arc settings, where primary melts pass high-temperature mantle rocks, leading to olivine oversaturated liquids. Crystallization of these liquids in the lower arc crust then would produce cpx-bearing dunites or olivine-rich wehrlites (Kelemen, 1990).

On the other hand, wehrlites may even be residues of hydrous melting of fertile peridotite, where incongruent melting of opx could produce opx-free residues with high olivine/cpx ratios (Gaetani & Grove, 1998). However, due to high modal abundances of cpx in ATCO wehrlites (56 % and 68 %, respectively), and due to their association to the gabbros of the ATCO, we rule out this mechanism to have played a major role in the formation of these rocks.

4.5.2 Origin of gabbroic rocks

4.5.2.1 Mineral compositions

Cr_2O_3 in gabbro cpx is at the lower end of the range defined by Elthon et al. (1992) for oceanic cumulates, and also in the lower range of the compositional field given for low-p cpx from experiments and for MORB phenocrysts (Elthon 1987; Fig. 4). Cr_2O_3 contents are also lower than in Leg 153 gabbros from the Mid-Atlantic Ridge (Ross & Elthon 1997b). This is consistent with prior spinel and/or cpx fractionation and implies that the gabbros crystallized from already evolved

melts, which possibly were derivative liquids of wehrlite formation. This assumption is supported by the closely associated occurrence of gabbros and wehrlites, and also by lower Na_2O concentrations in wehrlite cpx than in gabbro cpx (Fig. 3). Pyroxenites have higher Na_2O abundances in cpx and are therefore most likely not cogenetic with the gabbros (Fig. 3). The overall scarcity of olivine in the gabbros, the low Mg# and very low NiO concentrations in gabbro and wehrlite olivine (<0.08 %) further indicate that substantial olivine fractionation occurred from a primary liquid prior to gabbro and possibly to wehrlite formation. Comparable to Cr in cpx, NiO in olivine from the most primitive gabbro sample (A54) is at the lower end of the compositional range given for oceanic cumulates (Elthon et al., 1992). Additionally, whole rock Ni concentrations are lower in ATCO gabbros than in Gabal Gerf and Oman gabbros (Fig. 7d), underlining the assumption of olivine fractionation prior to gabbro formation. Further evidence comes from calculated Mg# in olivine equilibrium melts of wehrlites and gabbro A54 (Mg# = 0.47 - 0.60 using $D^{ol/melt}$(FeO/MgO) = 0.33, Roeder & Emslie, 1970; Longhi et al., 1978), which are significantly lower than in primitive ocean floor basalts (0.66 - 0.76, Presnall & Hoover, 1987). These observations suggest that the first stage fractionation of primary magmas occurred prior to the formation of these gabbros.

4.5.2.2 Crystallization from a single intrusion

In terms of cpx Cr_2O_3 vs. cpx Mg#, all gabbroic rocks define a correlation where Cr_2O_3 decreases with decreasing Mg# (Fig. 4). Simultaneously, Na_2O in gabbro cpx first increases and then remains nearly constant (Fig. 3). These trends are consistent with the assumption of cpx (and possibly olivine) fractionation, leading to increasing Na_2O but decreasing Cr_2O_3 in gabbro cpx, followed by cpx - plagioclase fractionation. We therefore suggest that all gabbroic rocks were derived from a single parental melt by successive fractionation and that no significant replenishment of the magma chamber occurred during gabbro crystallization. These assumptions are underlined by the large modal and chemical variations in the gabbroic suite, ranging from primitive ol-gabbros (sample A54) to highly evolved diorites (sample A63). Additionally, whole rock compositions vary in a wide range but are consistent with olivine, cpx and plagioclase fractionation from a single melt (Fig. 7). Compared to the size of the gabbro body, the variations in mineralogy and whole rock compositions are large and thus inconsistent with multiple replenishment, which would probably result in monotonous modal and chemical compositions. This was shown, for example, for several mafic intrusions in which multiple replenishment occurred, leading to low variations in mineral compositions (e.g. Bushveld complex, Eales & Cawthorn, 1996; or KEHLS layered intrusion, Bernstein et al., 1996). In contrast, intrusions formed from a single melt batch are highly variable in mineralogy and mineral chemistry (e.g. Skaergaard intrusion, McBirney, 1996).

4.5.2.3 Order of crystallization

Based on the assumption that the gabbroic rocks crystallized from a single intrusive body, we derive the following order of gabbro formation from petrography, mineral compositions (Figs. 3 & 4) and whole rock geochemistry (Tab. 4, Figs. 7 & 8): olivine-gabbros - norites - gabbronorites - (hbl-)gabbros - gabbrodiorites - diorites. This order is consistent with field observations concerning the top-bottom relationship with the more evolved gabbros in the western part of the KAZ and more primitive olivine-gabbros and norites in the eastern part. The early occurrence of norites and gabbronorites as well as the occurrence of wehrlites as described above, implies that clinopyroxene and orthopyroxene were early liquidus phases during the evolution of the ATCO plutonic rocks. This agrees well with the order of crystallization given for hydrous basaltic melts associated with subduction zone settings, where cpx crystallizes prior to plagioclase (Cameron et al., 1980, Hebert & Laurent, 1990). It is also consistent with experimental results for the crystallization of hydrous basaltic (tholeiitic) liquids under moderate pressures (0.2 - 1.1 GPa), where cpx reaches the liquidus prior to plagioclase and the order of crystallization is olivine - cpx - (hornblende) - plagioclase (e.g. Yoder & Tilley, 1962).

4.5.2.4 Depth of gabbro formation

The occurrence of plagioclase on the liquidus of basaltic melts not only depends on melt composition and water content but also on pressure and thus depth of crystallization. Whereas under low-p conditions (up to ~ 0.2 GPa) plagioclase (and olivine) is an early liquidus phase for both dry and hydrous basaltic liquids (Sisson & Grove, 1993), the stability fields for plagioclase (and also olivine) decrease with increasing pressure, whereas the stability field for cpx increases. Considering the early occurrence of cpx on the liquidus during the formation of the ATCO plutonic rocks, this suggests their origin in a magma chamber located in mid-crustal levels under pressures higher than about 0.1 - 0.2 GPa. This inference is supported by the abundant occurrence of hornblende in many of the sampled gabbros, which allows to estimate pressure and temperature conditions of hornblende formation based on aluminium in hornblende (Blundy & Holland, 1990; Hammarstrom & Zen, 1986; Hollister et al., 1987; Schmidt, 1992) and hornblende-plagioclase equilibrium (Blundy & Holland, 1990). These estimates indicate subsolidus reequilibration of mineral assemblages in the ATCO gabbros between 0.2 and 0.4 GPa, corresponding to a minimum depth of hornblende formation of about 7 km within a temperature range between about 830°C - 750°C. Due to deficiencies of the Al in hornblende barometer and a dependency of calculated pressure not only from Al^T but also from the degree of water saturation, f_{O2} and temperature (Anderson & Smith, 1995), the given upper pressure limit may be an overestimation of the maximum depth of hornblende formation. Nevertheless, it seems reasonable to assume an intermediate to shallow level of final crystallization of the mafic to calc-alkaline magma between 7

and 12 km. Crystallization of primary phases such as olivine and clinopyroxene to form wehrlites and pyroxenites must have occurred earlier and thus most likely deeper under higher pressures. According to experimental results (Gust & Perfit, 1987; Tatsumi, 1982; Tatsumi et al., 1983), fractionation of olivine and cpx typically occurs from high-Mg basalts under both hydrous and dry conditions within a pressure range of 1.0 - 1.5 GPa. Low-pressure fractionation would produce plagioclase-bearing assemblages from the same parental melt (Grove et al., 1982).

4.5.3 Equilibrium melts

Mineral compositions of ultramafic cumulates and gabbros are used to infer the composition of equilibrium melts, assuming thermodynamic equilibrium between melts and fractionating phases. Applying the FeO/MgO partition coefficients for olivine-melt ($D^{ol/melt}$ = 0.32 - 0.33; Roeder & Emslie, 1970; Hirose & Kushiro, 1993; Longhi et al., 1978) and cpx-melt ($D^{cpx/melt}$ = 0.23 - 0.25; Walker et al., 1979) we calculated the Mg# of equilibrium melts from individual microprobe analyses and by using cpx sample averages. Using individual analyses yields the maximum compositional range due to compositional variations in each sample. We further calculated the Na_2O, Al_2O_3, Cr, Ti and Ni concentration of the equilibrium melts using cpx/melt and ol/melt partition coefficients, respectively. For wehrlites and pyroxenites, we also calculated the trace element composition of equilibrium melts from ion-microprobe data of samples A1, A28, A30 and A50 (Tab. 3). Trace element partition coefficients used are those compiled by Bédard (1994). The results are shown in Tab. 7 and Fig. 5.

4.5.3.1 Primary melt composition(s)

The most primitive equilibrium melt corresponds to the pyroxenites, with a range in Mg# = 0.66 - 0.69 (Tab. 7). This range lies well within the range given for primary magmas from different tectonic settings, including island arcs (0.62 - 0.76; Conrad & Kay, 1984) and primitive ocean floor basalts (0.66 - 0.76; Presnall & Hoover, 1987). Heath et al. (1998) described parental magmas from the Soufriere Volcano (Lesser Antilles), having ~ 12.5 % MgO and Mg# ~ 0.75, underlining the well known circumstance that island arc primary magmas are typically high-Mg melts from refractory mantle sources. Calculated Cr concentrations in pyroxenite equilibrium melts are 986 µg/g - 1440 µg/g (Tab. 7) and exceed the range given for primary magmas from mid-ocean ridge and island arc settings (200 µg/g - 1370 µg/g, average ~ 560 µg/g; Conrad & Kay, 1984; Frey et al., 1978). In contrast, Al_2O_3 and Na_2O concentrations are comparatively low (Tab. 7). The range in Ti concentration (1072 - 1362 µg/g; Tab. 7) is in the lower range of primary island arc magmas (420 - 6115 µg/g; Conrad & Kay, 1984), and also much lower than the average value of ~ 4800 µg/g given by Presnall and Hoover (1987) for primitive ocean floor basalts and below the average

Table 7: Compositional range of parental melts calculated from cpx-melt partition coefficients

	Mg#	Al_2O_3 [wt%]	Na_2O [wt%]	Cr [µg/g]	Ti [µg/g]	$(La/Yb)_n$ [4)]
$D^{cpx/melt}$	0.23[1)]	0.21[2)]	0.12[2)]	3.8[3)]	0.384[3)]	----
Pyroxenites						
Individual analyses[5)]	65 - 74	6.5 - 12.7	0.85 - 1.78	805 - 1600	515 - 2092	----
Sample averages[6)]	66 - 69	9.0 - 11.4	1.00 - 1.48	986 - 1440	1072 - 1362	0.27 - 0.33
Wehrlites						
Individual analyses	56 - 70	6.6 - 16.4	0.13 - 0.59	158 - 879	952 - 2217	----
Sample averages	60 - 62	12.3 - 14.3	0.36 - 0.40	477 - 502	1498 - 1853	0.31 - 0.52
Gabbroic rocks						
Individual analyses	27 - 53	3.7 - 28.7	0.83 - 5.34	8 - 410	1210 - 10575	----
Sample averages	29 - 52	7.4 - 21.7	1.38 - 3.87	10 - 226	2337 - 10247	----

[1)] Value for FeO/MgO partition between cpx/melt (Walker et al., 1979). [2)] Meyer et al. (1989). [3)] Bédard (1994). [4)] Chondrite normalized.
[5)] Compositional range calculated from individual grains. [6)] Compositional range calculated from sample averages.

MORB value (~ 9700 µg/g; Hofmann, 1988). Our estimates indicate that the parental melt attributed to the ATCO pyroxenites was a Cr-rich high-MgO magma derived from a highly refractory mantle wedge which underwent earlier melt extraction. High Cr concentrations also suggest that little or no spinel fractionation occurred from these melts prior to pyroxenite crystallization. On the other hand, assuming a common parental magma for dunite A21 and pyroxenites as considered above from spinel compositions, an even higher Mg# of 0.78 for the equilibrium melt of cumulate dunite A21 suggests that olivine fractionation occurred prior to pyroxenite formation. This is confirmed by the calculated Ni concentration in dunite A21 equilibrium melt (~ 304 µg/g), which is slightly lower than usually proposed for primary magmas (~ 400 µg/g, Frey et al., 1978; Hess, 1992). Using $D_{Ni}^{ol/melt}$ = 9.9 (calculated as a function of Fo; see Bédard, 1994), the fractionation of about 3.5 % olivine would reduce the Ni concentration from ~ 400 µg/g to ~ 300 µg/g (equilibrium crystallization). Further fractionation of about 7 % olivine having the composition of dunite A21 olivine would then reduce the Mg# of the melt to about 0.74, which is the upper limit of the pyroxenite equilibrium melt (Tab. 7). We therefore propose that the pyroxenite equilibrium melt is a good approximation of the primary liquid from which the plutonic section of the ATCO developed, although ~ 10 % olivine may have fractionated prior to pyroxenite crystallization.

4.5.3.2 Parental melts of wehrlites and gabbros

The melt from which the wehrlites crystallized (Mg# = 0.58 - 0.60 from olivine, Mg# = 0.60 - 0.62 from cpx, Tab. 7) was more evolved than the primary magma derived above. This is consistent with lower Cr# in wehrlite spinel (Fig. 2) and lower Cr concentrations in wehrlite

equilibrium melts (Tab. 7). However, contrary to this, Na concentrations and REE abundances in wehrlite equilibrium melts are also lower than in pyroxenite equilibrium melts (Tab. 7, Fig. 5). This rules out a common parental magma as outlined above and suggests that pyroxenites and wehrlites represent different melt batches. Additionally, low Ni concentrations in wehrlite equilibrium melts (~ 30 µg/g), as well as low Cr- and elevated Al_2O_3 and Ti concentrations (Tab. 7) indicate that wehrlites crystallized from a melt which underwent earlier fractionation of olivine and spinel, and thus wehrlite equilibrium melts do not represent primary magmas. It is likely that the wehrlite parental melts were derived from the same source as the pyroxenite parental melts, but during a second stage melting process, and possibly by higher degrees of melting. This would result in lower abundances of incompatible trace elements, whereas lower Mg# and Cr-contents could be explained by olivine and spinel fractionation preceeding wehrlite formation. Considering only moderate amounts of olivine and spinel fractionation, incompatible trace element abundances will not increase significantly, but Mg#, Ni and Cr will be reduced considerably. For example, fractionation of about 12 % olivine in equilibrium with a primary melt (~ Fo_{88}) would reduce the Mg# of this melt from ~ 70 to ~ 60, but would increase the incompatible trace element abundances by only about 14 %.

Gabbro equilibrium melts span a wide compositional range, with the most primitive members being more evolved than pyroxenite and wehrlite equilibrium melts. Very low Cr (10 µg/g - 226 µg/g) and Ni concentrations (~ 13 µg/g from olivine in sample A54) as well as elevated Ti and Na concentrations in gabbro equilibrium melts (Tab. 7) indicate that the parental melts of the gabbroic rocks underwent significant fractionation of olivine, cpx and spinel prior to gabbro formation.

4.5.4 Evidence for a boninitic source and degree of melting

4.5.4.1 Boninitic source characteristics

As shown in Fig. 5, the equilibrium melts of pyroxenites and wehrlites are strongly depleted in incompatible trace elements compared to N-MORB and to boninites from the Izu Bonin, Mariana and Papua New Guinea arcs. Instead, they closely resemble primary boninitic melt inclusions in olivine-phenocrysts (Fo up to 0.92) from boninitic lavas of the Troodos ophiolite (Portnyagin et al., 1996; Fig. 5). These boninites were formed in a supra-subduction zone mantle wedge from a highly refractory mantle source, and the melt inclusions are regarded as primary melts of their host boninites. Based on similar incompatible trace element abundances in pyroxenite and wehrlite equilibrium melts and boninitic melt inclusions from Cyprus, we propose a similarly depleted mantle source for the ATCO. This is in good agreement with the highly refractory character of the residual mantle rocks as described above. Both boninitic melt inclusions from Cyprus as well as

pyroxenite and wehrlite equilibrium melts are characterized by positive Sr anomalies, with higher $(Sr/Nd)_n$ ratios in wehrlite equilibrium melts (3.7 and 4.0, respectively) than in pyroxenite equilibrium melts (1.4 and 1.8, respectively). Positive Sr anomalies are also observed in recent boninites from different island arcs (Fig. 5) and in the volcanic rocks of the ATCO (Pfänder et al., submitted). Sr enrichment in ATCO parental melts is thus a source property and not related to partial melting of a plagioclase-rich source, as the ATCO source was shown to have been highly depleted. In contrast to the ATCO boninitic parental melts, MORB and OIB have either slightly negative or no Sr anomalies (e.g. Hofmann, 1997; see Fig. 5). Therefore, Sr excess is restricted to island arc environments and thus most likely produced by fluid transfer from the slab to the mantle wedge. For the ATCO ultramafic cumulates this implies that the slab influence increased over time from pyroxenite to wehrlite parental melt formation since wehrlite parental melts have higher positive Sr anomalies and were derived from the same source than pyroxenite parental melts as suggested above. In contrast to boninites and boninitic melt inclusions, wehrlite and pyroxenite equilibrium melts have strongly negative Zr and moderately negative Ti anomalies (Fig. 5). Negative Zr anomalies are a common feature in cpx due to a low cpx-melt partition-coefficient compared to Sm and Nd, and are observed in clinopyroxene from ultramafic cumulates from the Troodos ophiolite (Batanova et al., 1996) and in most residual abyssal peridotite clinopyroxenes (Johnson et al., 1990; Hellebrand et al., submitted). However, equilibrium melts calculated for the Troodos ultramafic cumulates lack this negative Zr anomaly, consistent with absent negative Zr anomalies in boninitic melt inclusions from the Troodos ophiolite (Portnyagin et al., 1996; Fig. 5). In boninites from the Izu Bonin, Mariana and Papua New Guinea arcs, Zr anomalies are also absent or positive, consistent with positive Zr anomalies typically observed in forearc boninites. Due to the widespread occurrence in forearc boninites, positive Zr anomalies are usually regarded as indicative for this specific tectonic setting (Pearce et al., 1992; Taylor et al., 1994). In contrast, negative Zr anomalies are common in most island arc basalts (e.g. McCulloch & Gamble, 1991) but have also been reported in boninitic parental melts of pyroxenite cumulates from the Bay of Islands ophiolite in Newfoundland (Sassen, 1999) as well as in a few back-arc related boninites (Kamenetsky et al., 1997; Hawkins & Melchior, 1985; Falloon & Crawford, 1991). We therefore suggest that the negative Zr anomaly in the ATCO boninitic melts is a source feature, although it is not yet clear which processes are responsible for producing them. This implies, that their evolution is most likely *not* related to the forearc region of the ophiolite, but possibly more close to the magmatic arc or even back-arc system. Arc back-arc boninitic suites are, for example, also known from the Mid-Palaeozoic Yukon-Tanana terrane in Canada (Piercey et al., 2001). Thus, the occurrence of boninites is not strictly limited to forearc regions. The evolution of the boninitic melts in the ATCO, however, would require an additional heat source beneath the island arc back-arc region, to enable higher degrees of melting of an already refractory mantle. This heat source could

be hot upwelling mantle material, rising in response to an increased back-arc spreading rate, as is a well known effect at mid-ocean ridges (e.g. Niu et al., 2001). Alternatively, as suggested by Kamenetsky et al. (1997) to explain the occurrence of boninitic primary melts in the Valu Fa back-arc region of the Tonga Ridge, a back-arc spreading center propagating towards the ridge system may have provided sufficient heat to produce boninitic melts from the refractory sub-arc mantle. A similar explanation was given by Falloon & Crawford (1991) in order to explain the boninite occurrences in the northern part of the Tonga arc, where the northeastern end of the Lau basin spreading center propagates towards the northern Tonga arc. In both cases, hot upwelling asthenosphere is proposed to be responsible for the remelting of a refractory, sub-arc mantle in the mantle wedge of the Tonga subduction zone.

Although orthopyroxene is able to fractionate the HFSE from the middle-(M)REE as $D^{opx/cpx}$ is about a factor of ten higher for the HFSE than for the MREE (Rampone et al., 1991; Sun & Kerrich, 1995; Dobosi et al., 1998), we exclude opx to have been a responsible phase in producing the observed HFSE anomalies in the ATCO boninitic parental melts. This is mainly because producing large negative Zr anomalies from primary melts would require significant orthopyroxene fractionation from these melts. This assumption, however, is rather unlikely with respect to high Mg# and Cr in pyroxenite cpx, and due to the absence of opx in ultramafic cumulates. On the other hand, we cannot rule out the existence of residual orthopyroxene in the source of the parental melts of the ATCO ultramafic cumulates, which may be in part responsible for the negative Zr and Ti anomalies.

4.5.4.2 Degree of melting from spinel compositions

As outlined above, harzburgites and most dunites preserved in the ATCO are regarded as residual mantle rocks, although some dunites may have partly originated from deserpentinization. Although nearly completely serpentinized, one harzburgite sample (A15) contains relict, disseminated spinel having a high Cr# (0.74) comparable to dunite spinels (Cr# = 0.77 - 0.83, except cumulate dunite A21; Tab. 2, Fig. 2). As shown by several authors, Cr# and Mg# of spinel are very sensitive to the degree of melting in residual mantle rocks such that Cr# increases with increasing degree of melting (e.g. Dick and Bullen, 1984). From highly correlated HREE abundances in residual cpx and Cr# in residual spinel, Hellebrand et al. (2001) found that the degree of melting, calculated from cpx compositions, can be expressed as a function of Cr# in spinel. As they only studied abyssal peridotites, the range in Cr# is restricted to an upper limit of 0.6, corresponding to a degree of melting of ~ 19 %. Nevertheless, high Cr# in residual mantle rocks of the ATCO suggests a high degree of melt extraction, exceeding 20% starting from a fertile spinel peridotite (Hellebrand et al., 2001). This is underlined by very low TiO_2 concentrations in dunite and harzburgite spinels (<0.07 %). Batanova et al. (1998) published a similar relationship,

also based on cpx compositions and Cr# in spinel, but they used residual mantle peridotites from the Bay of Islands ophiolite to estimate the degree of melting from Cr# in spinel. Using this relationship, the ATCO mantle rocks experienced about 25 % of total melt extraction. This high degree of melting agrees well with the low Al/Si ratios in the mantle rocks as described above (Fig. 6) but strongly contrasts with the low degree of melting that produced the volcanic rocks of the ATCO (Pfänder et al., submitted). Based on trace element compositions, Pfänder et al. (submitted) suggested that 2 - 3 % melting of a depleted mantle source modified by subducted sediments produced the island arc basalts, whereas the back-arc basalts of the ATCO were generated by 8 - 15 % melting of a similar source. Reconciling this discrepancy requires (1) the existence of a previously depleted mantle that entered the source region of the ATCO prior to melting, and (2) multiple melting events from the same source. The first melting event produced enriched melts represented by the volcanic rocks. These melts quickly passed the so far little thickened arc crust, thus sustaining initial isotopic heterogeneities (Pfänder et al., submitted). Further melting, triggered by hot upwelling mantle material as suggested above, then produced successively more depleted melt batches from the previously depleted source. Additionally, higher degrees of melting may have been responsible for the generation of more depleted melts. From these melts the ultramafic cumulates and gabbros developed.

4.5.5 Trace element compositions of gabbroic rocks and trapped-melt effects

4.5.5.1 Complications in the interpretation of trace element patterns

A general problem concerning whole-rock trace element compositions of plutonic rocks is that they do *a priori* not give melt compositions. Instead, whole-rock trace element compositions of plutonic rocks are mixtures of several components. Main components in this sense are the different mineral phases hosting different amounts of trace elements due to different mineral-melt partition coefficients. Therefore, trace element variations reflect different modal abundances superimposed on primary melt variations. For example, as shown by several authors (e.g. Sun & Kerrich,1995; Dobosi et al., 1998; Garrido & Bodinier, 1998), olivine and orthopyroxene have complementary anomalies for Ti, Zr, Hf and Nb relative to clinopyroxene. Nevertheless, we suggest that whole-rock trace element patterns such as negative Th and Nb anomalies in the ATCO gabbroic rocks (Fig. 9) qualitatively mimic the correponding melt compositions due to generally low partition coefficients for these elements in all gabbroic mineral phases. Therefore, the patterns of highly incompatible trace elements are regarded as source characteristics. Possible exceptions are Sr, Eu and Ba, which are moderately incompatible (Ba, Eu) and compatible (Sr) in plagioclase. Small anomalies of these elements may therefore be caused solely

by variable modal plagioclase abundances.

Further complications concerning trace element patterns in cumulate rocks arise from different amounts of trapped melt, e.g. melt fractions isolated from the main magma reservoir during the last stages of solidification, or during late-stage melt percolation. Generally, trapped intercumulus melts increase the abundances of incompatible trace elements in the whole-rock, dependent on the melt composition.

4.5.5.2 REE composition of gabbros and trapped-melt effects

Although petrological data allow the assumption that wehrlites and gabbros were derived from a common parental melt and that the gabbros crystallized from a single intrusive body, whole-rock trace element and isotopic data suggest that additional processes were involved during gabbro formation. Based on REE systematics, the ATCO gabbros can be classified into three different groups (Fig. 10): (1) LREE depleted rocks with absent or slightly positive Eu anomalies due to plagioclase accumulation (Figs. 10a & b). The REE abundances and patterns of this group are similar to depleted layered gabbros from the Oman ophiolite, which represent the lower part of the oceanic crust; (2) depleted, but slightly LREE enriched gabbros with positive Eu anomalies (Fig. 10c). Although represented by only two samples, the occurrence of these rocks indicates a highly depleted parental melt from which the gabbros crystallized; (3) enriched, but slightly LREE depleted rocks with negative Eu anomalies. These rocks are similar to varitextured gabbros from the Oman ophiolite (Fig. 10a). Based on the negative Eu anomaly and the overall enriched character compared to other gabbros, we conclude that these rocks are frozen melts, therefore resembling liquid compositions. An obvious feature in some ATCO gabbroic rocks are U-shaped LREE patterns with a selective enrichment of La, Ce and Pr relative to Nd. Such U-shaped LREE patterns are typically regarded as secondary enrichment effects due to late stage melt percolation or due to different amounts of trapped intercumulus melt. However, as the D-ratio between La and Nd for plagioclase is about 1.5, significant amounts of cumulate plagioclase should also produce a U-shaped LREE pattern. As the La/Nd ratio of the gabbros is well correlated with total Al_2O_3, and thus with modal plagioclase, we attribute the enrichment of La, Ce and, to lesser extent, of Pr in some of the samples mainly to high amounts of cumulate plagioclase rather than to variable amounts of trapped melt, which would only have a minor effect on total Al_2O_3. This assumption, however, implies a very efficient separation of intercumulus melt and residual minerals. On the other hand, assuming the La enrichment to be solely the result of melt addition, this allows to estimate the amount of intercumulus melt by assuming a reasonable composition for the trapped melt. By using the two samples with the most pronounced U-shaped LREE pattern (A55 & T28), we have estimated the maximum amount of trapped melt for the ATCO gabbros. To do so, we have extrapolated the depleted REE pattern of sample A55 and T28 downwards from Nd to La as

is shown in Fig. 10a (dashed line). This gives a hypothetical La concentration, and from the difference between the hypothetical and the measured La concentration, the amount of trapped melt was estimated by assuming that the intercumulus melt had a composition similar to N-MORB (3.9 µg/g La). The amounts of trapped melt estimated by this method are about 15.0 % (A55) and 13.6 % (T28), respectively. However, assuming the more realistic case, namely that the intercumulus melt had the equilibrium melt composition of sample A55 (~ 1.9 µg/g La), these amounts would be much higher (31 % and 28 %, respectively). Nevertheless, as outlined above, these estimates are upper limits as they do not consider La and Ce enrichment due to higher amounts of cumulus plagioclase.

4.5.6 Source composition, mixing relationships and assimilation

4.5.6.1 Isotopic constraints

In terms of $^{143}Nd/^{144}Nd$ vs. $^{147}Sm/^{144}Nd$ (Fig. 11) most gabbros including the plagiogranite fit an isochron corresponding to an age of 546 ± 18 Ma. This age is close to the zircon evaporation age of 569.6 ± 1.7 Ma for the plagiogranite sample (Pfänder et al., 1998), indicating a cogenetic relationship. This further underlines the assumption of gabbro formation from a single melt reservoir, at least for the samples lying on the isochron. However, two KAZ gabbros plot above the isochron, whereas three TCZ gabbros plot below it. This indicates a slightly higher initial ϵ_{Nd} value for the two KAZ gabbros (+6.9 and +7.1), and a slightly lower initial ϵ_{Nd} value for the three TCZ gabbros (+4.8 to +5.2) compared to the average value of +6.2 ± 0.6. Although these variations are low, they indicate either a heterogeneous source, or a mixing relationship caused by assimilation processes during the final crystallization of the intrusion. As the samples fit well to a mixing relationship in terms of initial ϵ_{Nd} vs. Nd concentration, we prefer the assumption of wall-rock assimilation, as this is most likely during the solidification of an intrusive body. However, in terms of their REE composition, the two KAZ gabbros having the highest initial ϵ_{Nd} values are more evolved with higher abundances of incompatible trace elements (Figs. 9 & 10) and, therefore, are late-stage fractionation products located at the top of the magmatic body. This is also consistent with the modal occurrence of quartz in these rocks. The average initial ϵ_{Nd} value of +6.2 ± 0.6 further indicates a slightly enriched or isotopically modified source compared to the depleted mantle 570 Ma ago (depleted mantle $\epsilon_{Nd}(570) = 8.75$; Goldstein et al., 1984).

Pb isotopic compositions of selected gabbros and plagioclase separates are shown in Fig. 12. Although there is a large variation that resulted from wall-rock assimilation as will be outlined below, we calculated the apparent range in µ-values (µ = present day $^{238}U/^{204}Pb$) of the parental melt of the gabbroic rocks. We applied a two-stage Pb evolution model following Stacey and

Kramers (1975) for the first step and then varied the second stage μ-value to fit the observed data. The age of the Earth was taken as 4.57 Ga. The range of μ = 9.47 - 10.07 for the gabbroic rocks (Fig. 12) overlaps well with the range given for the ATCO volcanic rocks (9.35 - 9.90; Pfänder et al., submitted), but the lower value is higher than the value given for the depleted mantle today (8.92; Doe & Zartmann, 1972). This underlines the assumption of a depleted but slightly modified source as constrained by initial ϵ_{Nd} values. In terms of $^{208}Pb/^{204}Pb$ vs. $^{206}Pb/^{204}Pb$ the gabbroic rocks, including the plagiogranite, yield a linear correlation giving a time-integrated Th/U of 3.5 - 3.8. This value is significantly higher than the depleted mantle value today (~ 2.5; Galer & O'Nions, 1985), and is therefore consistent with elevated μ and low initial ϵ_{Nd} values.

4.5.6.2 Trace element constraints

Further constraints on the source compositon of the parental melts of the ATCO plutonic rocks comes from trace elements, although there are difficulties in the interpretation of whole-rock trace element compositions as discussed above. However, variations in highly incompatible trace element ratios are straightforward in characterizing source compositions, if their mineral-melt partition coefficients are far below unity and if trapped melt fractions are low. Fig. 13 shows whole-rock $(Th/La)_n$ ratios vs. whole-rock Th concentrations of gabbroic rocks. The KAZ and TCZ gabbros plot within two distinct fields but define a good correlation between high $(Th/La)_n$ ratios and high Th concentrations in TCZ gabbros and lower $(Th/La)_n$ ratios and Th concentrations in KAZ gabbros. As various amounts of trapped melt would define a mixing line inconsistent with such a linear correlation, we interpret these variations as rock-specific properties reflecting variable melt compositions, although this is not entirely consistent with Nd isotopic data. Additionally, the highest $(Th/La)_n$ ratios and Th concentrations do not correspond with the samples having possibly high amounts of trapped melt as derived from REE systematics.

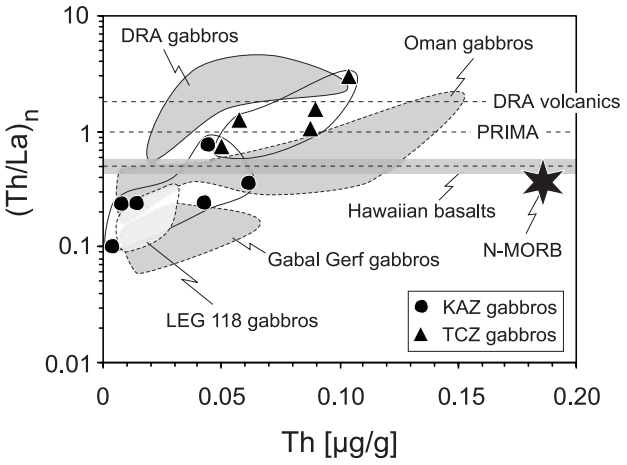

Fig. 13 Primitive mantle-normalized $(Th/La)_n$ vs. Th concentrations. TCZ gabbros have higher $(Th/La)_n$ ratios than KAZ and Gabal Gerf gabbros, due to Th enrichment. $(Th/La)_n$ ratios in TCZ gabbros are also higher than in N-MORB (star) and Hawaiian basalts (black line represents average value of Hofmann & Jochum, 1996, grey bar is 2σ). Note that low-Th Oman and Gabal Gerf gabbros (dashed fields) also have $(Th/La)_n$ < 1.0 (data sources: MacLeod & Yaouancq, 2000; Zimmer et al., 1995). DRA = Devil River Arc gabbros from New Zealand for comparison (data from Münker 2000). Data for Leg 118 gabbros from Hart et al. (1999).

Fig. 14 shows $(Th/La)_n$ vs. $(Th/Ba)_n$ of gabbroic rocks. This diagram is frequently used to constrain the source of oceanic island basalts which contain some amount of recycled oceanic crust (e.g. Hofmann & White, 1982; Hofmann & Jochum, 1996). The ATCO gabbros define a linear correlation corresponding to an average $(Ba/La)_n$ of 7.2 ± 0.7 (σ), and thus are characterized by Ba-excess relative to N-MORB, Hawaiian basalts and LEG 118 gabbros from the SW Indian Ridge. This Ba-excess is also expressed by lower $(Th/Ba)_n$ ratios and is obviously a feature common to ophiolite gabbros (Fig. 14), although only a few trace element data including Th concentrations are available so far. Contrary to this, there is now growing evidence that oceanic gabbros lack this Ba-excess, as shown by Snow et al. (pers. comm.) and Hart et al. (1999). An explanation for the Ba-excess in ophiolite gabbros would be Ba additon from the downgoing slab to the source region of primary melts of supra-subduction zone ophiolites, as Ba is a fluid-mobile element during slab dehydration (Johnson & Plank, 1999). However, as both the Oman and the Gabal Gerf ophiolites are suggested to be mid-ocean ridge type ophiolites (e.g. Nicolas 1989; Zimmer et al., 1995), this assumption is difficult to assess. Another feature characteristic of ophiolite gabbros is a larger range in $(Th/La)_n$ compared to oceanic gabbros (Fig. 14). For the ATCO we demonstrate below, that the variations in $(Th/La)_n$ were at least partly produced by wall-rock assimilation and crystal fractionation. However, this processes may not be transferable to other ophiolite gabbros and, therefore, we emphazise that the variations in $(Th/La)_n$ could possibly also be slab effects. For example, as shown by Johnson & Plank (1999), Th is mobilized during melting of subducted sediments, which has been proposed to play a role during the evolution of the ATCO volcanic rocks (Pfänder et al., submitted).

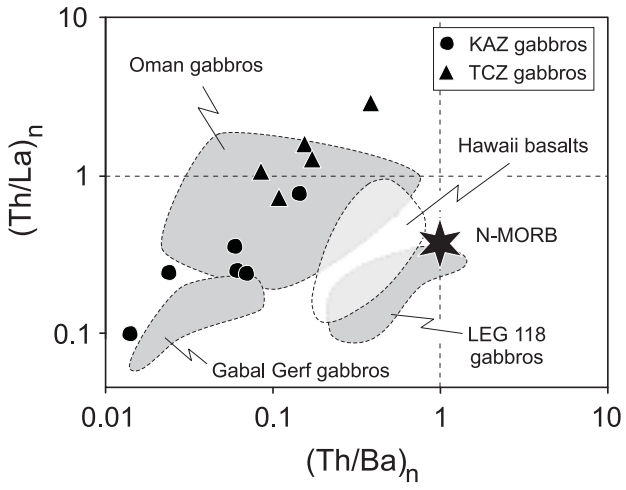

Fig. 14 Primitive mantle-normalized $(Th/La)_n$ vs. $(Th/Ba)_n$ of ATCO gabbros. Also shown are Gabal Gerf gabbros (Zimmer et al., 1996), Oman gabbros (MacLeod & Yaouancq, 2000), LEG 118 gabbros (Hart et al., 1999) and Hawaiian basalts (Hofmann & Jochum, 1996). TCZ gabbros have higher Th/La and Th/Ba ratios than KAZ gabbros. Generally, ophiolite gabbros tend to have lower Th/Ba ratios than oceanic gabbros and oceanic basalts, including MORB (N-MORB value from Hofmann, 1988). This is due to Ba excess rather than Th depletion as shown by comparable Th/La ratios in ophiolitic and oceanic gabbros.

4.5.6.3 Assimilation of pre-existing arc crust

The variation in Th/La ratios as well as Th concentrations is extremely large and higher than expected for a single intrusion (Fig. 15). This requires additional processes which efficiently modify the budget of highly incompatible trace elements inside the magma chamber without significantly affecting Nd isotopic compositions. Additionally, an elevated magma viscosity is required to preserve these heterogeneities. To evaluate the effects of combined crystallization and wall-rock assimilation on Th/La ratios and Th concentrations, we have carried out AFC calculations using the formalism given by DePaolo (1981) and using the calculated equilibrium melt compositions of the gabbros (Fig. 15). Equilibrium melts were calculated using bulk-rock distribution coefficients from mineral modes and mineral-melt partition coefficients given by Bédard (1994). As starting melt composition we have taken the equilibrium melt of the most primitive gabbro (olivine-gabbro A54), having ~ 0.1 µg/g Th and ~ 6.0 µg/g La. Th and La concentrations in the assimilated material are 11 µg/g Th and 30 µg/g La (Fig. 15a), and 5 µg/g and 25 µg/g (Fig. 15b). The former figures are average values for the upper continental crust as given by Taylor & McLennan (1995), whereas the latter values are from the most enriched volcanic rocks of the ATCO (Pfänder et al., submitted). The modal composition of the fractionating assemblage was 50 % cpx and 50 % plagioclase, but variable modal abundances of these phases in the fractionating assemblages only cause negligible effects due to very low partition coefficients of Th and La. As a general result, we found that the spread in Th/La vs. Th concentration is best explained by assuming variable r-values (r = assimilation rate / fractionation rate) between 0.03 and 0.8, combined with different fractionation rates up to ~ 80 % (Fig. 15). These conditions are realistic based on the assumption of an isolated, poorly mixed intrusion, where the marginal parts are characterized by higher r-values than the central parts. This also correlates well with field

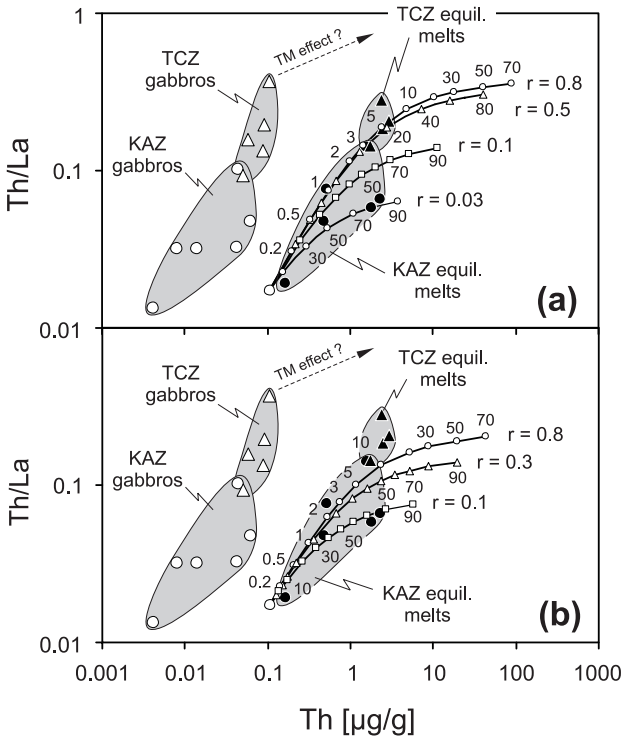

Fig. 15 Th/La vs. Th concentrations for KAZ and TCZ gabbros and equilibrium melt compositions. Curves show residual melt evolution produced by AFC. Numbers denote amount fractionated. (a) assimilation of "average upper continental crust", (b) assimilation of enriched ATCO volcanic rocks. Melt compositions are calculated from mineral modes and mineral-melt partition coefficients, r = ratio of assimilation rate to fractionation rate. Details see text.

relationships, where the TCZ gabbros in the northeastern part of the ophiolite (Fig. 1) represent the marginal and upper parts of the magma chamber (with elevated r-values of ~ 0.5 to ~ 0.8) and with slightly lower initial ϵ_{Nd} values (Fig. 11). In contrast, the KAZ gabbros are from the central and lower parts of the intrusion, experiencing lower assimilation rates, and are characterized by lower amounts of fractionation (up to 10 %) and slightly higher ϵ_{Nd} values (Fig. 11). Due to higher Th concentrations and higher Th/La ratios, the model assuming „average upper continental crust" assimilation (Fig. 15a) fits the data better than using enriched ATCO volcanic rocks as assimilated material (Fig. 15b). However, the assumption of crustal assimilation is rather unlikely, first because the ATCO evolved as part of an intra-oceanic island arc system most likely away from continental crust and, second, because the assimilation of large amounts of crustal material should result in a larger shift in Nd isotopic compositions, at least if this crust was significantly older than the ATCO. We therefore prefer the assumption of the assimilation of volcanic rocks, which have been shown to represent the initial phase of ophiolite formation in the ATCO (Pfänder et al., submitted), and because these volcanic rocks have only slightly lower initial ϵ_{Nd} values than the gabbroic rocks. Additionally, it is most likely that the variations in $(Th/La)_n$ are somewhat lower than in Fig. 14, since no trapped-melt was considered for the calculation of the equilibrium melts. Accounting for small amounts of trapped-melt would slightly lower the variations in Th/La. Although we prefer the crustal assimilation scenario to explain the isotopic and trace element variations in the gabbroic rocks of the ATCO, we cannot rule out that some of the variations in Th/La may be an inherited feature from the source which was modified by subducted components. This is because it was shown, that source heterogeneities are preserved in the volcanic rocks of the ATCO (Pfänder et al., submitted). We emphasize, however, that the large variations in Th/La are very difficult to achieve solely by source contamination, partial melting and subsequent melt migration. Additionally, it was shown that the plutonic and volcanic sections of the ophiolite underwent different evolutions (Pfänder et al., 1999a).

Pb isotoic compositions are highly variable (Fig. 12) in the gabbroic rocks and thus are consistent with wall-rock assimilation of ATCO volcanic rocks which also have highly variable Pb isotopic compositions (Pfänder et al., submitted). As shown in Fig. 12, the Pb isotopic compositions of two plagioclase fractions plot along a line with a slope corresponding to an age of 570 Ma, which is the age of the ATCO. We interpret this line as a mixing line between the parental melt of the gabbroic rocks ($\mu \leq 9.47$, initial $^{207}Pb/^{204}Pb \leq 15.50$, initial $^{206}Pb/^{204}Pb \leq 17.62$) and the wall-rocks ($\mu \geq 10.07$, initial $^{207}Pb/^{204}Pb \geq 15.66$, initial $^{206}Pb/^{204}Pb \geq 18.02$), and assimilation produced this mixing relationship after the emplacement of the intrusion about 570 Ma ago. Therefore, the gabbros finally crystallized with slightly different µ-values due to incomplete homogenization during solidification of the magma chamber, leading to variable present-day Pb isotopic compositions.

4.5.7 Evolution of the lower oceanic crust in the ATCO

4.5.7.1 Geodynamic setting and crustal structure

As shown by Pfänder et al. (submitted), the evolution of the ATCO is closely related to an island arc system, active around 570 Ma ago. Whereas the volcanic rocks of the ophiolite comprise both island arc and back-arc related basalts, the plutonic rocks of the ATCO bear typical petrological and geochemical features of an island arc origin. These are especially opx-bearing gabbroic rocks (Tab. 1), refractory spinel compositions (Fig. 2), as well as highly calcic plagioclase compositions (Tab. 2). Additionally, all gabbroic rocks are characterized by negative Nb anomalies (Fig. 9) with $(Nb/Th)_n$ = 0.01 - 0.87 (except A62: 1.25) and $(Nb/La)_n$ = 0.01 - 0.31. These ratios are significantly lower than in N-MORB (2.5 and 0.90, respectively; Hofmann, 1988) and lower than in gabbroic rocks from the N-MORB type Oman and Gabal Gerf ophiolites ($(Nb/Th)_n$ = 0.43 - 4.7 in Oman gabbros and 0.64 - 14 in Gabal Gerf gabbros; $(Nb/La)_n$ = 0.42 - 2.6 in Oman gabbros and 0.19 - 1.5 in Gabal Gerf gabbros). This clearly indicates an island arc related origin for the parental melts of the ATCO gabbros as mentioned above. In addition, positive LILE anomalies (Fig. 9), expressed by high $(Ba/La)_n$ ratios (3.4 - 12), indicate the influence of slab-derived components on the mantle source of the parental melts of the ATCO gabbros. This is also confirmed by positive Sr anomalies (Fig. 9) with $[Sr]_{Al}/Nd$ = 1.3 - 29. The slab-derived components also led to lower initial ϵ_{Nd} values in the ATCO gabbros (+4.8 to +7.1) than expected for mantle-derived rocks ($\epsilon_{Nd}(570)$ = +8.75 for the depleted mantle, assuming a linear evolution after Goldstein et al., 1984). Instead, initial ϵ_{Nd} values in the ATCO gabbros are on average identical to island arc volcanic rocks from the ATCO (Pfänder et al., submitted), further underlining a subduction-related origin. Pb isotopic compositions are more radiogenic than expected for purely mantle-derived rocks. A similar environment as for the volcanic rocks of the ATCO is therefore expected for the evolution of the ultramafic and gabbroic rocks.

As described by several authors (Gill, 1981; Kersting & Arculus, 1994; Yanagi & Maeda, 1998), magma reservoirs may be located beneath island arcs at the crust-mantle boundary, possibly due to a density contrast. These magma reservoirs crystallize ultramafic and mafic cumulates to build up the lowermost crust in magmatic arc systems (Conrad & Kay, 1984; Lapierre et al., 1992). More evolved magmas from which olivine, spinel and pyroxene already crystallized, resulting in a lower liquid density, subsequently rise to shallower crustal levels to form gabbroic and dioritic intrusions. We propose a similar mechanism for the evolution of the ultramafic and gabbroic rocks in the ATCO. According to this, the ultramafic cumulates developed within an open-system magma chamber at the base of the island arc crust, or even within the mantle itself, where refractory magmas were fed from the melting region in the mantle wedge below (Fig. 16). High pressure fractionation occurred where cpx was the dominant liquidus phase, leading to predominantly

pyroxenite and possibly wehrlite formation. This assumption is consistent with experimental results (Green & Ringwood, 1968) which have shown that in hydrous, quartz-normative basaltic liquids cpx is the only liquidus phase at pressures > 1 GPa. More evolved, and therefore less denser, magmas left the magma chamber at the top, intruding shallower levels of the arc crust (Fig. 16). One of these intrusions is possibly represented by the ATCO gabbroic rocks which in this case crystallized in a closed system, except that magma modification occurred by wall-rock assimilation and crystal fractionation.

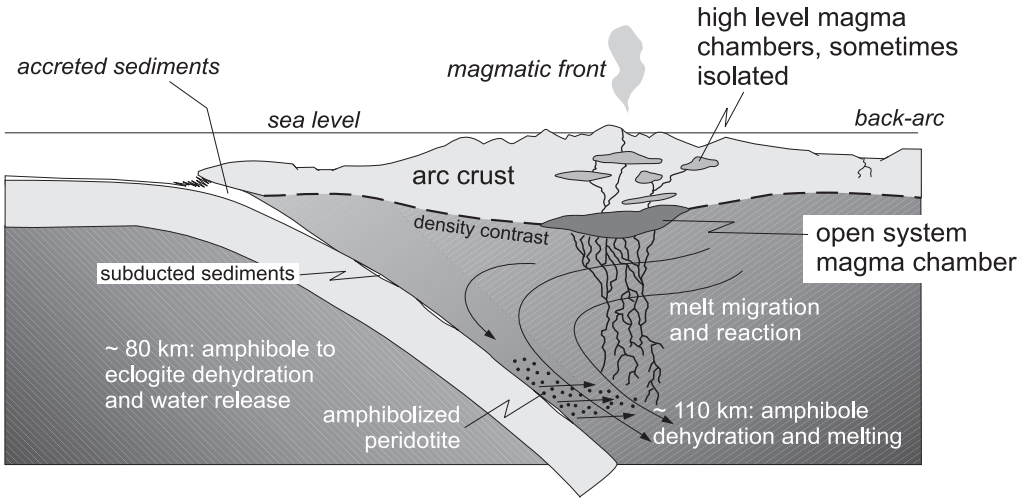

Fig. 16 Schematic model showing evolution of the crust in the ATC magmatic arc. First stage fractionation of refractory melts occurred at a deep level, open system magma chamber, leading to the formation of ultramafic cumulates. Evolved melts intruded into shallower levels, and crystallization occurred simultaneously with assimilation of more enriched, pre-existing arc crust.

4.5.7.2 Open system magma chamber evolution

In Fig. 17 we outline three schematic models describing different mechanisms possible for the evolution of the lower crust in the ATCO. All models are based on the assumption of a magma reservoir in the deep arc crust as described above. This magma reservoir operates as an open system in which primary melts from the mantle wedge undergo multiple fractionation (X) and replenishment (R), and where eruptions (E) of evolved melts occur periodically (note that „erupted“ melts also may end up as shallow-level gabbroic intrusions). In model (a) only fractionation and replenishment occurs (E = 0), and the replenishment rate is equal to the fractionation rate ($\partial R/\partial t = \partial X/\partial t$). Therefore, the magma mass is constant over time, and the magma chamber is migrating upwards such that crustal growth is equal to $\partial X/\partial t$. This scenario requires volatile-poor melts and moderate replenishment rates to prevent eruptions for a distinct time interval. Additionally, for this

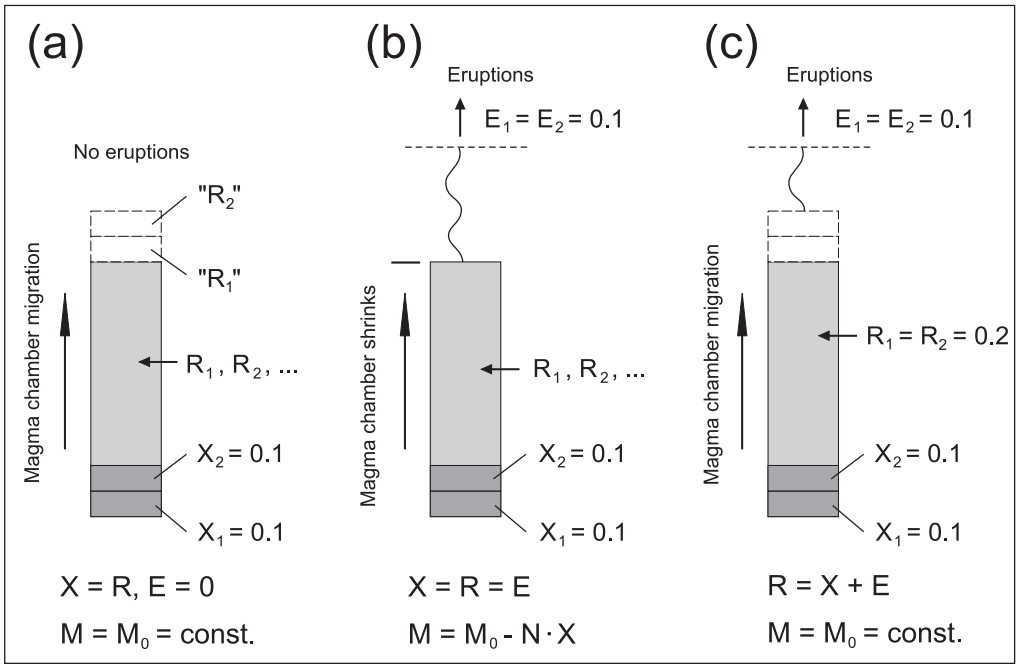

Fig. 17 Three simplified schematic models describing different possible mechanisms for the evolution of the lower crust in the ATCO. X = amount fractionated per cycle, E = amount erupted per cycle, R = amount replenished per cycle, N = number of cycles, M = mass of magma (M0 = initial mass). (a) No eruptions (E = 0), replenishment is equal to fractionation (R = X), magma mass is constant, magma chamber is migrating upwards and crustal growth is equal to X for each cycle. (b) Rates of fractionation, eruption and replenishment are equal (X = E = R), mass of magma is reduced by X for each cycle, magma chamber disappears after M0/X cycles. (c) This scenario is a combination of (a) and (b), where the sum of fractionation and eruption is equal to replenishment such that the mass of magma remains constant (in this example X = Y, but this is not compelling). We prefer model (a) to have been the dominant mechanism during the evolution of the ATCO, because the ATCO is strongly dominated by plutonic rocks and because of highly enriched volcanic rocks, which require high amounts of enrichment by cumulate formation.

model the resulting arc crust is dominated by plutonic rocks. In model (b) fractionation, eruption, and replenishment rates are equal ($\partial X/\partial t = \partial E/\partial t = \partial R/\partial t$), and the magma mass is reduced by $\partial X/\partial t$ for a given time interval. As a consequence, the magma chamber disappears after a time $t = M_0/(\partial X/\partial t)$, where M_0 is the initial magma mass. Crustal growth in this case is both by the formation of mafic cumulate rocks and by volcanic eruptions. This scenario allows volatile-rich melts and higher rates of replenishment. Model (c) is a combination of (a) and (b), where the sum of fractionation rate and eruption rate equals the replenishment rate, such that the mass of magma remains constant over time ($\partial X/\partial t + \partial E/\partial t = \partial R/\partial t$). Varying the fractionation and eruption rates will yield either a crust dominated by volcanic rocks ($\partial E/\partial t > \partial X/\partial t$), or a crust dominated by plutonic rocks ($\partial X/\partial t > \partial E/\partial t$). In any case, this model requires higher melting rates, e.g. higher geothermal gradients and crust growths by the upwards migrating melt lens and by volcanic eruptions. For the

evolution of the plutonic rocks of the ATCO we prefer model (a), that is model (c) where $\partial E/\partial t \rightarrow 0$, as the dominant mechanism. This is because of the widespread occurrence of ultramafic cumulates and plutonic rocks in the ATCO and because of highly enriched volcanic rocks (Pfänder et al., submitted), which require high amounts of cumulate formation from primary depleted melts.

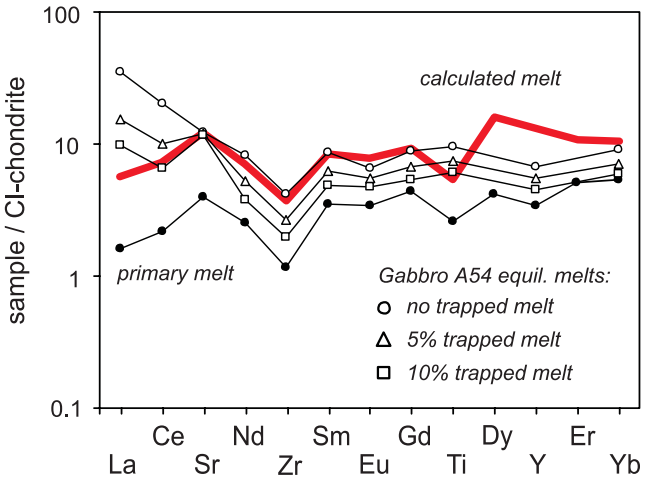

Fig. 18 Results of model calculations assuming an open system magma chamber evolution. The gabbro A54 equilibrium melt is best approximated by solely cpx fractionation from a primary melt. Details see text.

To estimate the amount of cumulates necessary to produce the parental melt of the gabbros from a primary magma, we have calculated open-system magma evolution by adopting model (a) in Fig. 17, and by combining Rayleigh fractionation, bulk mixing and mass balance considerations. The detailled procedure and the equations used are given in Appendix B. The pyroxenite equilibrium melt was used as the primary magma which originated from the mantle wedge above the subduction zone. The most primitive gabbro (A54) was chosen as representative for the parental melt of the gabbros. By using the modal composition (Tab. 1) and whole-rock trace element concentrations (Tab. 4), we calculated the composition of the equilibrium melt of this gabbro. The aim was to reproduce this composition by open-system evolution of the primary magma, and the results are shown in Fig. 18. The best fit was achieved by assuming solely clinopyroxene fractionation and by assuming 25 fractionation and replenishment cycles, with 10 % fractionation and 10 % replenishment per cycle. This fits all trace elements from Sr to Gd, whereas concentrations of La and Ce in the resulting melt are too low compared to the equilibrium melt of the gabbro, and the HREE are slightly too high (considering only Er and Yb, however, the fit is quite good). The negative Ti anomaly in the calculated melt is absent in the gabbro equilibrium melt, but this is most likely because ilmenite is present in gabbro A54, which was not considered during equilibrium melt calculations. The total amount of pyroxenite cumulate formed through this scenario would be 2.5 times the mass of the initial magma. Using pure olivine as fractionating phase would require less fractionation and replenishment cycles due to a higher incompatibility of the trace elements in olivine (again 10 % fractionation and 10 % replenishment per cycle), but the fit is generally worse (either HREE are fitted by assuming 10 cycles, or Sr, Nd and Zr are fitted by assuming 20 cycles). La and Ce are also strongly underestimated. For a combination of cpx and olivine, the fit is comparable to the pure cpx fit up to olivine contents of about 20%, therefore

wehrlite formation can also be explained by this model. However, we emphazise that the HREE excess problem is higher for higher amounts of olivine in the cumulus assemblage. Plagioclase in the cumulus assemblage is not consistent with the high Sr concentration in the gabbro equilibrium melt, ruling out plagioclase as a liquidus phase during the evolution of the parental melts of the gabbros.

Our results indicate that the occurrence of pyroxenites and even wehrlites closely associated with residual ultramafic mantle rocks is consistent with the assumption of a large magma reservoir at the base of the island arc crust. Pyroxenite occurrences suggest cpx to have been the major liquidus phase, which requires elevated pressures of roughly 1 GPa or more. The minimum crustal thickness of the magmatic crust in the ATCO magmatic arc, therefore, was about 30 - 35 km during the stage of ultramafic and gabbroic cumulate formation.

4.6 CONCLUSIONS

(1) Highly refractory mineral compositions in residual mantle rocks of the ATCO indicate the existence of a strongly depleted mantle source which underwent about 25 % total melt extraction, based on spinel compositions. Low trace element abundances, negative Nb anomalies and positive ϵ_{Nd} values in gabbroic rocks further suggest that this mantle source was a previously depleted mantle wedge above an intra-oceanic subduction zone.

(2) Primary magmas calculated from clinopyroxene compositions are very similar to boninitic melt inclusions from the supra-subduction zone type Troodos ophiolite. This suggests that the primary magmas of the plutonic section of the ATCO were also boninites.

(3) The occurrence of ultramafic cumulates associated with highly refractory mantle rocks is best explained by assuming high-pressure fractionation of boninitic parental melts under hydrous conditions.

(4) The variety of gabbros present, as well as mineral and whole-rock compositions indicate that crystallization of gabbroic rocks occurred within a relatively small magma chamber under moderate to low pressures, without appreciable replenishment. The cooling rate was sufficiently slow to produce abundant exsolutions in clinopyroxene and relatively homogeneous, unzoned plagioclase. Amphibole compositions suggest that final crystallization occurred in mid-crustal levels between around 7 and 12 km depth.

(5) Abundance ratios of highly incompatible trace elements are consistent with the assumption of substantial wall-rock assimilation during gabbro crystallization. Isotopic data further indicate that the parental melt of the gabbros intruded into pre-existing island arc crust with nearly the same ϵ_{Nd} value.

(6) Our geochemical and petrological data are best explained by assuming a two-stage process operating during the evolution of the lower and middle crust in the ATCO. Initial fractionation of primary, boninitic magmas occurred under pressures > 1 GPa in an open-system magma chamber at the crust mantle boundary, leading to ultramafic cumulates. More evolved melts were periodically expelled from this magma chamber to produce mafic intrusions at mid-crustal levels. The ATCO gabbroic rocks represent such an intrusion, which crystallized in a nearly closed system.

4.7 References

Allan, J.F., Sack, R.O. & Batiza, R. (1988). Cr-rich spinels as petrogenetic indicators: MORB-type lavas from the Lamont seamount chain, Eastern Pacific. *American Mineralogist* **73**, 741-753.

Anderson, J.L. & Smith, D.R. (1995). The effects of temperature and f_{O2} on the Al-in-hornblende barometer. *American Mineralogist* **80**, 549-559.

Barnes, C.G., Johnson, K., Barnes, M.A., Prestvik, T., Kistler, R.W. & Sundvoll, B. (1995). The Grayback Pluton: Magmatism in a Jurassic Back-Arc Environment, Klamath Mountains, Oregon. *Journal of Petrology* **36**, 397-416.

Batanova, V.G., Sobolev, A.V. & Schmincke, H.-U. (1996). Parental melts of the intrusive cumulates of the Troodos massif, Cyprus: a study of clinopyroxenes and melt inclusions in plagioclase. *Petrology* **4**, 273-282.

Batanova, V.G., Suhr, G. & Sobolev, A.V. (1998). Origin of geochemical heterogeneity in the mantle peridotites from the Bay of Islands ophiolite, New Foundland, Canada: Ion microprobe study of clinopyroxenes. *Geochimica et Cosmochimica Acta* **62**, 853-866.

Bédard, J.H. (1994). A procedure for calculating the equilibrium distribution of trace elements among the minerals of cumulate rocks, and the concentration of trace elements in the coexisting liquids. *Chemical Geology* **118**, 143-153.

Bernstein, S., Kelemen, P.B. & Brooks, C.K. (1996). Evolution of the Kap Edward Holm Complex: a Mafic Intrusion at a Rifted Continental Margin. *Journal of Petrology* **37**, 497-519.

Bernstein, S., Rosing, M.T., Brooks, C.K. & Bird, D.K. (1992). An ocean-ridge type magma chamber at a passive volcanic, continental margin: the Kap Edward Holm layered gabbro complex, East Greenland. *Geological Magazine* **129**, 437-456.

Bloomer, S.H. (1983). Distribution and origin of igneous rocks from the landward slopes of the Mariana Trench: implications for ist structure and evolution. *Journal of Geophysical Research* **88**, 7411-7428.

Bloomer, S.H., Natland, J.H. & Fisher, R.L. (1989). Mineral relationships in gabbroic rocks from fracture zones of Indian Ocean ridges: evidence for extensive fractionation, parental diversity and boundary-layer recrystallization. *Geological Society of London Special Publications* **42**, 107-124.

Bloomer, S.H., Taylor, B., MacLeod, C.J., Stern, R.J., Fryer, P., Hawkins, J.W. & Johnson, L. (1995). Early arc volcanism and the ophiolite problem: a perspective from ocean drilling in the western Pacific. *Geophysical Monograph* **88**, 1-30.

Blundy, J.D. & Holland, J.B (1990). Calcic amphibole equilibria and a new amphibole-plagioclase geothermometer. *Contributions to Mineralogy and Petrology* **104**, 208-224.

Boudier, F., Nicolas, A. (1995). Nature of the Moho transition zone in the Oman Ophiolite. *Journal*

of Petrology **36**, 777-796.

Boudier, F., Nicolas, A., Ildefonse, B. & Jousselin, D. (1997). EPR microplates, a model for the Oman Ophiolite. *Terra Nova* **9**, 79-82.

Briqueu, L., Mével, C., Boudier, F. (1991). Sr, Nd and Pb isotopic constraints in the genesis of a calc-alkaline plutonic suite in Oman ophiolite related to the obduction process. *In: Ophiolite Genesis and Evolution of the Oceanic Lithosphere, T.J. Peters et al. (eds), Ministry of Petroleum and Minerals, Sultanate of Oman* , 517-542.

Cameron, W.E., Nisbet, E.G. & Dietrich, V.J. (1980). Petrographic dissimilarities between ophiolitic and ocean floor basalts. *In: Ophiolites: Proceedings of the International Ophiolite Symposium, Panayiotou, A. (ed), Geol. Surv. Dept., Nicosia, Cyprus* , 182-192.

Cawthorn, R.G. & Davies, G. (1983). Experimental data at 3 kbars pressure on parental magma to the Bushveld complex. *Contributions to Mineralogy and Petrology* **83**, 128-135.

Conrad, W.K. & Kay, R.W. (1984). Ultramafic and Mafic Inclusions from Adak Island: Crystallization History, and Implications for the Nature of Primary Magmas and Crustal Evolution in the Aleutian Arc. *Journal of Petrology* **25**, 88-125.

Davies, J.H. & Bickle, M.J. (1991). A physical model for the volume and composition of melt produced by hydrous fluxing above subduction zones. *Philosophical Transactions of the Royal Society of London,* **335**, 355-364.

DePaolo, D.J. (1981). Trace element and isotopic effects of combined wallrock assimilation and fractional crystallization. *Earth and Planetary Science Letters* **53**, 189-202.

Dick, H.J.B. (1989). Abyssal peridotites, very slow spreading ridges and ocean ridge magmatism. *Geological Society of London Special Publications* **42**, 71-105.

Dick, H.J.B. & Bullen, T. (1984). Chromian spinel as a petrogenetic indicator in abyssal and alpine-type peridotites and spatially associated lavas. *Contributions to Mineralogy and Petrology* **86**, 54-76.

Dobosi, G., Jenner, G.A. & Embey-Isztin, A. (1998). Clinopyroxene/orthopyroxene trace-element partition coefficients in spinel peridotite xenoliths. *Mineralogical Magazine* **62A**, 393-394.

Doe, B.R. & Zartman, R.E. (1979). Plumbotectonics, The Phanerozoic . *In: Geochemistry of hydrothermal ore deposits. H.L. Barnes (ed.), Wiley Interscience* , 22-70.

Eales, H.V. & Cawthorn, R.G. (1996). The Bushveld Complex. *In: Layered Intrusions, Cawthorn, R.G. (ed), Elsevier, Amsterdam* , 181-230.

Elthon, D. (1987). Petrology of Gabbroic Rocks from the Mid-Cayman Rise Spreading Center. *Journal of Geophysical Research* **92**, 658-682.

Elthon, D., Stewart, M. & Ross, K.D. (1992). Compositional trends of minerals in oceanic cumulates. *Journal of Geophysical Research* **97**, 15189-15199.

Evans, B.W. (1977). Metamorphism of alpine peridotite and serpentinite. *Annual Review of Earth and Planetary Sciences* **5**, 397-447.

Falloon, T.J. & Crawford, A.J. (1991). The petrogenesis of high-calcium boninite lavas dredged from the northern Tonga ridge. *Earth and Planetary Science Letters* **102**, 375-394.

Frey, F.A., Green, D.H. & Roy, S.D. (1978). Integrated models of basalt petrogenesis: a study of quartz tholeiites to olivine melilitites from South Eastern Australia utilizing geochemical and experimental petrological data. *Journal of Petrology* **19**, 463-513.

Gaetani, G.A. & Grove, T.L. (1998). The influence of water on melting of mantle peridotite. *Contributions to Mineralogy and Petrology* **131**, 323-346.

Galer, S.J.G. (1999). Optimal double and triple spiking for high precision lead isotopic measurement. *Chemical Geology* **157**, 255-274.

Galer, S.J.G. & O'Nions, R.K. (1985). Residence time of thorium, uranium and lead in the mantle with implications for mantle convection. *Nature* **316**, 778-782.

Gamble, J., Woodhead, J., Wright, I. & Smith, I. (1996). Basalt and sediment geochemistry and magma petrogenesis in a transect from oceanic island arc to rifted continental margin arc: the Kermadec-Hikurangi Margin, SW Pacific. *Journal of Petrology* **37**, 1523-1546.

Garrido, C.J. & Bodinier, J.-L. (1998). Distribution of trace elements in minerals from anhydrous spinel peridotites and websterites from the Ronda peridotite: implications for the nature of LILE, REE and HFSE reservoirs in the subcontinental lithospheric mantle. *Mineralogical Magazine* **62A**, 498-499.

Gill, J.B. (1981). Orogenic andesites and plate tectonics. *Springer Verlag, Berlin - Heidelberg*

Goldstein, S., O'Nions, R.K. & Hamilton, P.J. (1984). A Sm-Nd isotopic study of atmospheric dusts and particulates from major river sediments. *Earth and Planetary Science Letters* **70**, 221-236.

Göpel, C., Allègre, C.J. & Xu, R-H. (1984). Lead isotopic study of the Xigaze ophiolite (Tibet): the problem of the relationship between magmatites (gabbros, dolerites, lavas) and tectonites (harzburgites). *Earth and Planetary Science Letters* **69**, 301-310.

Green, D.H. & Ringwood, A.E. (1968). Genesis of the calc-alkaline igneous rock suite. *Contributions to Mineralogy and Petrology* **18**, 105-162.

Grove, T.L., Gerlach, D.C., Sando, T.W. & Baker, M.B. (1982). Origin of calc-alkaline series lavas at Medicine Lake volcano by fractionation, assimilation and mixing. *Contributions to Mineralogy and Petrology* **80**, 160-182.

Gruau, G, Bernard-Griffiths, J., Lecuyer, C., Henin, O., Mace, J. & Cannat, M. (1995). Extreme Nd isotopic variation in the Trinity Ophiolite Complex and the role of melt/rock reactions in the oceanic lithosphere. *Contributions to Mineralogy and Petrology* **121**, 337-350.

Gust, D.A. & Perfit, M.R. (1987). Phase relations of a high-Mg basalt from the Aleutian Island arc:

implications for primary island arc basalts and high-Al basalts. *Contributions to Mineralogy and Petrology* **97**, 7-18.

Hammarstrom, J.M. & Zen, E.A. (1986). Aluminium in hornblende: An empirical igneous geobarometer. *American Mineralogist* **71**, 1297-1313.

Hart, S.R., Blusztajn, J., Dick, H.J.B., Meyer, P.S. & Muehlenbachs K. (1999). The fingerprint of seawater circulation in a 500-meter section of ocean crust gabbros. *Geochimica et Cosmochimica Acta* **63**, 4059-4080.

Hart., S.R. & Zindler, A. (1986). In search of a bulk-earth composition. *Chemical Geology* **57**, 247-267.

Hawkins, J.W. & Melchior, J.T (1985). Petrology of Mariana Trough and Lau Basin basalts. *Journal of Geophysical Research* **90**, 11431-11468.

Heath , E., Macdonald, R., Belkin, H., Hawkesworth, C. & Sigurdsson, H. (1998). Magmagenesis at Soufriere Volcano, St. Vincent, Lesser Antilles Arc. *Journal of Petrology* **39**, 1721-1764.

Hebert, R. & Laurent, R. (1990). Mineral chemistry of the plutonic section of the Troodos Ophiolite: New constraints for genesis of arc-related ophiolites. *In: Ophiolites: Oceanic Crustal Analogues: Proceedings of the Symposium "Troodos 1987", Malpas, J., Moores, E.M., Panayiotou, A., Xenophontos, C. (eds), Geol. Surv. Dept., Nicosia, Cyprus* , 149-163.

Hellebrand, E., Snow, J.E. & Hofmann, A.W. (subm.). Garnet-field melting and late-stage refertilization in 'residual' abyssal peridotites from the Central Indian Ridge. *Journal of Petrology*, submitted

Hellebrand, E., Snow, J.E., Dick, H. & Hofmann, A.W. (2001). Coupled major and trace elements as indicators of the extent of melting in mid-ocean-ridge peridotites. *Nature* **410**, 677-681.

Helz, R.T. (1973). Phase relations of basalts in their melting range at P_{H2O} = 5 kb as a function of oxygene fugacity. Part I. Mafic phases. *Journal of Petrology* **14**, 249-302.

Hess, P.C. (1992). Phase equilibria constraints on the origin of ocean floor basalts. *Geophysical Monograph* **71**, 67-102.

Hickey, R.L. & Frey, F.A. (1982). Geochemical characteristics of boninite series volcanics - implications for their source. *Geochimica et Cosmochimica Acta* **46**, 2099-2115.

Hirose, K. & Kushiro, I. (1993). Partial melting of dry peridotites at high pressures: Determination of compositions of melts segregated from peridotite using aggregates of diamond. *Earth and Planetary Science Letters* **114**, 477-489.

Hofmann, A.W. (1997). Mantle geochemistry: the message from oceanic volcanism. *Nature* **385**, 219-229.

Hofmann, A.W. (1988). Chemical differentiation of the Earth: the relationship between mantle, continental crust, and oceanic crust. *Earth and Planetary Science Letters* **90**, 297-314.

Hofmann, A.W. & Jochum, K.P. (1996). Source characteristics derived from very incompatible trace elements in Mauna Loa and Mauna Kea basalts, Hawaii Scientific Drilling Project. *Journal of Geophysical Research* **101**, 11831-11839.

Hofmann, A.W. & White, W.M. (1982). Mantle plumes from ancient oceanic crust. *Earth and Planetary Science Letters* **57**, 421-436.

Hollister, L.S., Grissom, G.C., Peters, E.K., Stowell, H.H. & Sisson, V.B. (1987). Confirmation of the empirical correlation of Al in hornblende with pressure of solidification of calc-alkaline plutons. *American Mineralogist* **72**, 231-239.

Irvine, T.N. (1977). Origin of chromitite layers in the Muskox intrusion and other stratiform intrusions: a new interpretation. *Geology* **5**, 273-277.

Irvine, T.N. (1967). Chromian Spinel as a Petrogenetic Indicator. *Canadian Journal of Earth Sciences* **4**, 71-103.

Jagoutz, E., Palme, H., Baddenhausen, H, Blum, K., Cendales, M., Dreibus, G., Spettel, B., Lorenz, V. & Wänke, H. (1979). The abundances of major, minor and trace elements in the earth's mantle as derived from primitive ultramafic nodules. *Proc. Lunar Planet. Sci. Conf.* **10**, 2031-2050.

Jochum, K.P., Dingwell, D.B., Rocholl, A., Stoll, B. & Hofmann, A.W. - and 20 others (2000). The preparation and preliminary characterisation of eight geological MPI-DING reference glasses for in-situ microanalyses. *Geostandards Newsletter* **24**, 87-133.

Jochum, K.P., Laue, H.J., Seufert, H.M., Dienemann, C., Stoll, B., Pfänder, J., Flanz, M., Achtermann, H. & Hofmann, A.W. (1997). Multi-Ion Counting-Spark Source Mass Spectrometry (MIC-SSMS): A new multielement technique in geo- and cosmochemistry. *Fresenius Journal of Analytical Chemistry* **359**, 385-389.

Jochum, K.P., Seufert, H.M., Midinet-Best, S., Rettmann, E., Schönberger, K. & Zimmer, M. (1988). Multi-element analysis by isotope dilution-spark source mass spectrometry (ID-SSMS). *Fresenius Journal of Analytical Chemistry* **331**, 104-110.

Johnson, K.T.M., Dick, H.J.B. & Shimizu, N. (1990). Melting in the oceanic upper mantle: An ion microprobe study of diopsides in abyssal peridotites. *Journal of Geophysical Research* **95**, 2661-2678.

Johnson, M.C. & Plank, T. (1999). Dehydration and Melting Experiments Constrain the Fate of Subducted Sediments. *G cubed* **1**.

Jordan, T.H. (1978). Composition and development of the continental tectosphere. *Nature* **274**, 544-548.

Jousselin, D. & Nicolas, A. (2000). The Moho transition zone in the Oman ophiolite-relation with wehrlites in the crust and dunites in the mantle. *Mar. Geophys. Res.* **21**, 229-241.

Kamenetsky V.S., Crawford, A.J., Eggins, S. & Mühe, R. (1997). Phenocryst and melt inclusion chemistry of near-axis seamounts, Valu Fa Ridge, Lau Basin: insight into mantle wedge melting and the addition of subduction components. *Earth and Planetary Science Letters* **151**, 205-223.

Kelemen, P.B. (1990). Reaction between Ultramafic Rock and Fractionating Basaltic Magma I. Phase Realtions, the Origin of Calc-alkaline Magma Series, and the Formation of Discordant Dunite. *Journal of Petrology* **31**, 51-98.

Kelemen, P.B., Hirth, G., Shimizu, N., Spiegelman, M. & Dick, H.J.B. (1997). A review of melt migration processes in the adiabatic upwelling mantle beneath oceanic spreading ridges. *Philosophical Transactions of the Royal Society of London* **355**, 283-318.

Kelemen, P.B., Shimizu, N., Salters, V.J.M. (1995). Extraction of mid-ocean-ridge basalt from the upwelling mantle by focused flow of melt in dunite channels. *Nature* **375**, 747-753.

Kersting, A.B. & Arculus, R.J. (1994). Klyuchevskoy volcano, Kamchatka, Russia - the role of high-flux recharged, tapped, and fractionated magma chamber(s) in the genesis of high-Al2O3 from high-MgO basalt. *Journal of Petrology* **35**, 1-41.

Korenaga, J. & Kelemen, P.B. (1997). Origin of gabbro sills in the Moho transition zone of the Oman ophiolite: Implications for magma transport in the oceanic lower crust. *Journal of Geophysical Research* **102**, 27729-27749.

Kushiro, I. (1990). Partial melting of mantle wedge and evolution of island arc crust. *Journal of Geophysical Research* **95**, 15929-15939.

Kuzmichev, A.B., Bibikova, E.V. & Zhuralev, D.Z. (2001). Neoproterozoic (~800 Ma) orogeny in the Tuva-Mongolia massif (Siberia): island arc-continent collision an the northeaqst Rodiniaq margin. *Precambrian Research* **110**, 109-126.

Lapierre, H., Ortiz, L.E., Abouchami, W., Monod, O., Coulon, C. & Zimmermann J.L. (1992). A crustal section of an intraoceanic island-arc - the late Jurassic early Cretaceous Guanajuato magmatic sequence, Central Mexico. *Earth and Planetary Science Letters* **108**, 61-77.

Leake, B.E. (1978). Nomenclature of amphiboles. *Mineralogical Magazine* **42**, 533-563.

Longhi, J., Walker, D. & Hays, J.F. (1978). The distribution of Fe and Mg between olivine and lunar basaltic liquids. *Geochimica et Cosmochimica Acta* **42**, 1545-1558.

MacLeod, C.J. & Yaouancq, G. (2000). A fossil melt lens in the Oman ophiolite: Implications for magma chamber processes at fast spreading ridges. *Earth and Planetary Science Letters* **176**, 357-373.

McBirney, A.R. (1996). The Skaergaard Intrusion. *In: Layered Intrusions, Cawthorn, R.G. (ed), Elsevier, Amsterdam* , 147-180.

McCulloch, M.T. & Gamble, J.A. (1991). Geochemical and geodynamical constraints on subduction zone magmatism. *Earth and Planetary Science Letters* **102**, 358-374.

McDonough, W.F. (1990). Constraints on the composition of the lithospheric mantle. *Earth and Planetary Science Letters* **101**, 1-18.

Metzner, C. & Grimmeisen, W. (1990). MONA: a user-friendly computer-program for calculating the modal mineralogy of rocks from chemical analyses. *European Journal of Mineralogy* **2**, 735-738.

Münker, C. (2000). The Isotope and Trace Element Budget of the Cambrian Devil River Arc System, New Zealand: Identification of Four Source Components. *Journal of Petrology* **41**, 759-788.

Nicolas, A. (1989). Structures of Ophiolites and Dynamics of Oceanic Lithosphere. *Petrology and Structural Geology, Kluwer Academic Publishers* **4**, 367 p.

Nicolas, A., Boudier, F. & Ildefonse, B. (1996). Variable crustal thickness in the Oman ophiolite: Implication for oceanic crust. *Journal of Geophysical Research* **101**, 17941-17950.

Niu, Y., Bideau, D., Hékinian, R. & Batiza, R. (2001). Mantle compositional control on the extent of mantle melting, crust production, gravity anomaly, ridge morphology, and ridge segmentation. *Earth and Planetary Science Letters* **186**, 383-399.

O'Hanley, D.S. (1996). Serpentinites: records of tectonic and petrological history. *Oxford Monographs on Geology and Geophysics, Oxford University Press, New York, Oxford* **34**, 277 p.

Otten, M.T. (1984). The origin of brown hornblende in the Artfjället gabbro and dolerites. *Contributions to Mineralogy and Petrology* **86**, 189-199.

Pallister, J.S. & Knight, R.J. (1981). Rare-Earth Element Geochemistry of the Samail Ophiolite near Ibra, Oman. *Journal of Geophysical Research* **86**, 2673-2697.

Pearce, J.A., van der Laan, S.R., Arculus, R.J., Murton, B.J., Ishii, T., Peate, D.W. & Parkinson, I.J. (1992). Boninite and harzburgite from LEG 125 (Bonin-Mariana forearc): A case study of magma genesis during the initial stages of subduction. *In: Fryer, P.; Pearce, J.A.; Stokking, L.B. et al.: Proc. of the Ocean Drilling Program, Scientific Results* **125**, 623-659.

Pfänder, J., Jochum, K.P., Todt, W. & Kröner, A. (1999a). Relationships between the mantle, lower crust and upper crust within the Agardagh Tes-Chem ophiolite, Central Asia: evidence from petrologic, trace element, and isotopic data. *Ofioliti* **24**, 151-152.

Pfänder, J.A., Jochum, K.P., Kozakov, I., Kröner, A. & Todt, W. (subm.). Coupled evolution of back-arc and island arc-like mafic crust in the late Neoproterozoic Agardagh Tes-Chem ophiolite, Central Asia: Evidence from trace element and Sr-Nd-Pb isotope data. *Contributions to Mineralogy and Petrology*, submitted.

Pfänder, J.A., Jochum, K.P., Kröner, A., Kozakov, I., Oidup, C. & Todt, W. (1998). Age and geochemical evolution of an early Cambrian ophiolite-island arc system in Tuva, South Central Asia. *In: Generation and Emplacement of Ophiolites Through Time. Geological Survey of*

Finland, Special Paper **26**, 42

Pfänder, J.A., Jochum, K.P., Sassen, A., Stoll, B., Maissenbacher, P. & Murmann, M. (1999b). Determination of Y, Zr and ultra-low Nb concentrations in geological material by multi-ion counting spark-source mass spektrometry (MIC-SSMS). *Fresenius Journal of Analytical Chemistry* **364**, 376-380.

Phipps Morgan, J, Harding, A., Orcutt, J., Kent, G. & Chen, Y.J. (1994). An observational and theoretical synthesis of magma chamber geometry and crustal genesis along a mid-ocean ridge spreading center. *In: Magmatic Systems, Ryan, M.P. (Ed)* , 139-178.

Piercey, S.J., Murphy, D.C., Mortensen, J.K. & Paradis, S. (2001). Boninitic magmatism in a continental margin setting, Yukon-Tanana terrane, southeastern Yukon, Canada. *Geology* **29**, 731-734.

Portnyagin, M.V., Magakyan, R. & Schmincke, H.-U. (1996). Geochemical variability of boninite magmas: Evidence from magmatic inclusions in highly magnesian olivine from lavas of southwestern Cyprus. *Petrology* **4**, 250-265.

Presnall, D.C. & Hoover, J.D. (1987). High pressure phase equilibrium constraints on the origin of mid-ocean ridge basalts. *In: Magmatic processes: Physicochemical Principles. Mysen, B.O. (ed.)*, 75-89.

Quick, J.E. (1981). Petrology and petrogenesis of the Trinity peridotite, an upper mantle diapir in the eastern Klamath mountains, northern California. *Journal of Geophysical Research* **86**, 1836-1837.

Rampone, E., Bottazzi, P. & Ottolini, L. (1991). Complementary Ti and Zr anomalies in ortho- pyroxene and clinopyroxene from mantle peridotites. *Nature* **354**, 518-520.

Rautenschlein, M., Jenner, G.A., Hertogen, J., Hofmann, A.W., Kerrich, R., Schmincke, H.-U. & White, W.M. (1985). Isotopic and trace element composition of volcanic glasses from the Akaki Canyon, Cyprus: implications for the origin of the Troodos ophiolite. *Earth and Planetary Science Letters* **75**, 369-383.

Roeder, P.L. & Emslie, R.F. (1970). Olivine-liquid equilibrium. *Contributions to Mineralogy and Petrology* **29**, 275-289.

Ross, K. & Elthon, D. (1997b). Cumulus and postcumulus crystallization in the oceanic crust: Major-and trace-element geochemistry of LEG 153 gabbroic rocks. *Proceedings of the Ocean Drilling Program* **153**, 333-350.

Ross, K. & Elthon, D. (1997a). Extreme incompatible trace-element depletion of diopside in residual mantle from south of the Kane fracture zone. *Proceedings of the Ocean Drilling Program* **153**, 277-284.

Ross, K. & Elthon, D. (1993). Cumulates from strongly depleted mid-ocean-ridge basalt. *Nature*

365, 826-829.

Sassen, A. (1999). Geochemistry, petrology and isotope geochemistry of magmatic intrusions in the Lewis Hills Massif, Bay of Islands Ophiolite: Implications for magma diversity at an island arc-spreading ridge intersection. *Unpublished doctoral thesis, Universität zu Köln*, 244p.

Schmidt, M.W. (1992). Amphibole composition in tonalite as a function of pressure: an experimental calibration of the Al-in-hornblende barometer. *Contributions to Mineralogy and Petrology* **110**, 304-310.

Sengör, A.M.C, Natal'in, B.A. & Burtman, V.S. (1993). Evolution of the Altaid tectonic collage and Palaeozoic crustal growth in Eurasia. *Nature* **364**, 299-307.

Sharma, M., Wasserburg, G.J., Papanastassiou, D.A., Quick, J.E., Sharkov, E.V. & Laz'ko, E.E. (1995). High $^{143}Nd/^{144}Nd$ in extremely depleted mantle rocks. *Earth and Planetary Science Letters* **135**, 101-114.

Shervais, J.W. (2001). Birth, death, and resurrection: The life cycle of suprasubduction zone ophiolites. *G cubed* **2**.

Sisson, T.W. & Grove, T.L. (1993). Experimental investigations of the role of H2O in calc-alkaline differentiation and subduction zone magmatism. *Contributions to Mineralogy and Petrology* **113**, 143-166.

Smewing, J.D. (1981). Mixing Characteristics and Compositional Differences in Mantle-Derived Melts Beneath Spreading Axes: Evidence From Cyclically Layered Rocks in the ophiolite of North Oman. *Journal of Geophysical Research* **86**, 2645-2659.

Stacey, J.S & Kramers, J.D. (1975). Approximation of terrestrial lead isotope evolution by a two-stage model. *Earth and Planetary Science Letters* **26**, 207-221.

Straub, S.M. & Martin-Del Pozzo (2001). The significance of phenocryst diversity in tephra from recent eruptions at Popocatepetl volcano (central Mexico). *Contributions to Mineralogy and Petrology* **140**, 487-510.

Suhr, G. & Robinson, P.T. (1994). Origin of mineral chemical stratification in the mantle section of the Table Mountain massif (Bay of Islands Ophiolite, Newfoundland, Canada). *Lithos* **31**, 81-102.

Sun, M. & Kerrich, R. (1995). Rare earth element and high field strength element characteristics of whole rocks and mineral separates of ultramafic nodules in Cenozoic volcanic vents of southeastern British Columbia, Canada. *Geochimica et Cosmochimica Acta* **59**, 4863-4879.

Tatsumi, Y. (1982). Origin of high-magnesian andesites in the Setouchi volcanic belt, southwest Japan, II. Melting phase relations at high pressures. *Earth and Planetary Science Letters* **60**, 305-317.

Tatsumi, Y., Sakuyama, M., Fukuyama, H. & Kushiro, I. (1983). Generation of arc basalt magmas

and thermal structure of the mantle wedge in subduction zones. *Journal of Geophysical Research* **88**, 5815-5825.

Taylor, R.N, Nesbitt, R.W., Vidal, P., Harmon, R., Auvray, B. & Croudace, I.W. (1994). Mineralogy, Chemistry, and Genesis of the Boninite Series Volcanics, Chichijima, Bonin Islands, Japan. *Journal of Petrology* **35**, 577-617.

Taylor, S.R. & McLennan, S.M. (1995). The geochemical evolution of the continental crust . *Rev. Geophys.* **33**, 241-265.

Thompson, G.M., Malpas, J. & Smith, I.E.M. (1997). The geochemistry of tholeiitic and alkalic plutonic suites within the Northland ophiolite, norhtern New Zealand; magmatism in a back arc basin. *Chemical Geology* **142**, 213-223.

Walker, D., Shibata, T. & DeLong, S.E. (1979). Abyssal Tholeiites from the Oceanographer Fracture Zone II. Phase Equilibria and Mixing. *Contributions to Mineralogy and Petrology* **70**, 111-125.

Woodhead, J.D., Eggins, S.M. & Johnson, R.W. (1998). Magma Genesis in the New Britain Island Arc: Further Insights into Melting and Mass Transfer Processes. *Journal of Petrology* **39**, 1641-1668.

Yanagi, T. & Maeda, S. (1998). Magma evolution observed in the Matsuura basalts in northwest Kyushu, Japan: An example of high-pressure open system fractional crystallization in a refilled magma chamber near the crust-mantle boundary. *Physics of the Earth and Planetary Interiors* **107**, 203-219.

Yoder, H.S.Jr. & Tilley, C.E. (1962). Origin of basalt magmas: An experimental study of natural and synthetic rock systems. *Journal of Petrology* **3**, 342-512.

Zimmer, M., Kröner, A., Jochum, K.P., Reischmann, T., Todt, W. (1995). The Gabal Gerf complex: A Precambrian N-MORB ophiolite in the Nubian Shield, NE Africa. *Chemical Geology* **123**, 29-51.

APPENDIX A: ANALYTICAL METHODS

Electron microprobe analyses were carried out on a Jeol JXA-8900 RL at Universität Mainz using 15kV acceleration voltage, 12 nA probe current and a beam size of 2 µm. Counting times were between 5 and 50 seconds. Data for each sample represent averages of at least three analyses per mineral and between three to five minerals per sample.

Clinopyroxene trace element compositions were measured on a modified Cameca IMS-3f secondary ion mass spectrometer (SIMS) at the Max-Planck-Institut für Chemie in Mainz. Ionization was performed using negative oxygen ions, an acceleration voltage of 12.5 kV and a primary beam current current of 10 nA. The spot size for these conditions was 15-20 µm. An energy offset of -80 eV was used to suppress multiple charged ions and molecules. Results were calculated from drift- and background-corrected element/^{30}Si-ratios using the known SiO_2 content of each clinopyroxene. Three to five spots on at least two grains were measured per sample, measuring time per spot was about 1 hour. The well-known reference glass sample GOR123 (Jochum et al., 2000) was used as external standard for calibration. The accuracy (95 % confidence level) is better than 20 % for REE and better than 12 % for other trace elements (Hellebrand et al., 2001).

Major elements and Ba, Y, Sc, V, Cr, Co, Ni, Cu, Zn, and Ga were determined on a Philips PW 1404 X-ray fluorescence spectrometer at Universität Mainz using fused and powder pellets. Reproducibility is better than 1 % for major elements and better than 4 % for trace elements. FeO was calculated from Fe_2O_3 assuming that all iron was Fe^{II}. All other trace elements (except Sr, Sm, and Nd) were determined by isotope dilution multi-ion counting spark-source mass spectrometry at the Max-Planck-Institut für Chemie (MIC-SSMS; Jochum et al. 1997). For the MIC-SSMS measurement of very low Zr and Nb concentrations in gabbroic rocks, a special procedure was necessary to correct for isobaric interferences due to high amounts of Al_2O_3 in most of the samples. This procedure includes a high mass resolution (~3000) and a mathematical interference correction, resulting in an analytical precision of 2-5 % for concentrations down to 0.02 µg/g and 10 % for lower concentrations (Pfänder et al. 1999b). For all other trace elements the precision of the MIC-SSMS technique is within 3-5 % of the recommended values for international reference materials for elements determined by isotope dilution and within 10 % for elements determined by the internal standard procedure (Jochum et al. 1988).

Nd-, Sr-, and Pb isotopic compositions were measured on two Finnigan MAT 261 multicollector thermal ion mass spectrometers in static mode. Nd and Sr isotopic analyses and Nd, Sm and Sr concentrations were analyzed on the same aliquot using mixed ^{150}Nd-^{149}Sm and ^{84}Sr-^{85}Rb spikes. After spiking, the sample powder was dissolved in HF-HNO_3 in closed Teflon® beakers for >48 hours at 200°C. REE were separated from other elements by using Bio-Rad AG 50W-X12 cation-exchange resin. Sm and Nd were subsequently separated on HDEHP-coated Teflon® powder

using diluted HCl eluents. Total procedural blanks were <500 pg for Sr and <30 pg for Nd. Measured Sr isotopic ratios were normalized to $^{86}Sr/^{88}Sr = 0.1194$, Nd isotopic ratios to $^{146}Nd/^{144}Nd = 0.7219$. Repeated measurements of the NBS 987 Sr standard resulted in $^{87}Sr/^{86}Sr = 0.710212 \pm 0.000036$ and $^{84}Sr/^{86}Sr = 0.056495 \pm 0.000053$ (errors 2σ, N = 10). Repeated measurements of the La Jolla Nd standard gave $^{143}Nd/^{144}Nd = 0.511839 \pm 0.000025$, $^{145}Nd/^{144}Nd = 0.348402 \pm 0.000017$ and $^{150}Nd/^{144}Nd = 0.236478 \pm 0.000082$ (2σ, N = 33). Pb was isolated from hand-picked rock chips up to 200 mg by weight. After leaching in hot 6M HCl for several hours and rinsing in ultrapure water, the chips were dissolved in closed Teflon® beakers using hot HF-HNO_3 for >48 hours. Plagioclase was isolated from crushed rock fractions after sieving by magnetic separation and hand picking. After washing in concentrated, hot HNO_3 for several hours and rinsing in ultrapure water, the plagioclase fractions were leached in a mixture of hot HNO_3/HF for a couple of minutes. The leaching procedure was repeated two or three times to remove radiogenic components. Remaining plagioclase was then washed in ultrapure water and dissolved in hot HF-HNO_3. Pb separation was carried out on Bio-Rad AG1-X8 anion-exchange resin using a diluted HBr-HNO_3 eluent. Total procedural blanks were between 8 - 40 pg. Pb isotopic compositions were measured by using the triple spike technique (Galer 1999). This technique requires the run of a spiked and unspiked sample aliquot to correct for instrumental mass fractionation, but improves the accuracy of the isotopic ratios by at least a factor of 10 compared to external correction for mass fractionation. Repeated measurements of the NBS 981 Pb standard gave $^{208}Pb/^{204}Pb = 36.7059 \pm 0.0046$, $^{207}Pb/^{204}Pb = 15.4923 \pm 0.0023$, $^{206}Pb/^{204}Pb = 16.9386 \pm 0.0021$, $^{207}Pb/^{206}Pb = 0.914621 \pm 0.00005$ (± 2σ, N = 20, normalized to $^{208}Pb/^{206}Pb$ of NBS 981 to correct for fractionation).

APPENDIX B: EQUATIONS AND MODEL PARAMETERS

Open system magma chamber evolution was calculated from a combination of Rayleigh fractionation, bulk mixing and mass balance considerations. The whole process was subdivided into discrete cycles, where for each cycle the following processes were assumed to occur in the following order:

(1) from an existing magma chamber, having an initial mass of $M_0 = 1$, a certain amount X of cumulate with a bulk partition coefficient D is fractionated using Rayleigh fractionation. The concentration of a specific element in the residual melt fraction is then:

$$^{n}C_l = C_0(1-X)^{(D-1)}$$

C_0 = initial concentration of a specific element, n = cycle number, here n = 1

(2) From this residual melt fraction, a certain amount E is erupted, further reducing the total amount of melt in the magma chamber to:

$$^{n}M_{fe} = M_0 - X - E \qquad n = 1$$

(3) Then, replenishment with a melt having C_0 occurs where R is the amount of replenishing melt, yielding a total amount of melt in the magma chamber after replenishing:

$$^{n}M_{fer} = {}^{n}M_{fe} + R \qquad n = 1$$

The concentration for the element of choice in this replenished melt is given by:

$$^{n}C_m = (R\,C_0 + {}^{n}M_{fe}\,{}^{n}C_l) / {}^{n}M_{fer} \qquad n = 1$$

(4) Then, the next cycle starts with Rayleigh fractionation, but considering the new amount of total melt (n = 2):

$$^{n}C_l = {}^{n-1}C_m(1-X/{}^{n-1}M_{fer})^{(D-1)}$$

and:

$$^{n}M_{fe} = {}^{n-1}M_{fer} - X - E \quad \text{and} \quad {}^{n}M_{fer} = {}^{n}M_{fe} + R$$

and finally:

$$^{n}C_m = (R\,C_0 + {}^{n}M_{fe}\,{}^{n}C_l) / {}^{n}M_{fer}$$

From the equations given in (4), all following melt fractions are calculated (n = 3, 4, ...). Note that X, E and R are fixed throughout the evolution of the magma chamber and are expressed relative to M_0.